REPORT DOCUMENTATION PAGE

Form Approved OMB No. 0704-0188

1. REPORT DATE *(DD-MM-YYYY)*	2. REPORT TYPE	3. DATES COVERED *(From – To)*
12-07-2004	Final Report	28-Dec-00 - 1-May-04

4. TITLE AND SUBTITLE

Advanced processes for high-strength titanium alloys

5a. CONTRACT NUMBER
STCU Registration No: P-057

5b. GRANT NUMBER

5c. PROGRAM ELEMENT NUMBER

6. AUTHOR(S)

Professor Orest Ivasyshyn

5d. PROJECT NUMBER

5d. TASK NUMBER

5e. WORK UNIT NUMBER

7. PERFORMING ORGANIZATION NAME(S) AND ADDRESS(ES)

Institute for Metal Physics
36 Vernadsky Street
Kyiv 03142
Ukraine

8. PERFORMING ORGANIZATION REPORT NUMBER

N/A

9. SPONSORING/MONITORING AGENCY NAME(S) AND ADDRESS(ES)

EOARD
PSC 802 BOX 14
FPO 09499-0014

10. SPONSOR/MONITOR'S ACRONYM(S)

11. SPONSOR/MONITOR'S REPORT NUMBER(S)
STCU 008008

12. DISTRIBUTION/AVAILABILITY STATEMENT

Approved for public release; distribution is unlimited.

20040923 000

13. SUPPLEMENTARY NOTES

14. ABSTRACT

In first part of this project, double Electron Beam Melting (EBM) was investigated for melting of high-strength alpha + beta and beta titanium alloys. The following advantages, as compared to Vacuum Arc Remelting (VAR), are expected:
- full dissolution of LDI due to higher temperature and longer times in melt condition;
- essential elimination of HDI by means of 'intermediate bath' application;
- employment of cheaper initial materials, such as sponge blocks;
- improved chemical homogeneity of ingots due to introducing alloying elements directly into a melting zone;
- improved microstructure due to better controlled solidification of liquid metal.

The second part of the project is aimed at the development of a novel approach in processing of beta alloys, which comprises cold or warm deformation and rapid heat treatment. An attractive advantage of beta-titanium alloys consists in a high plasticity in solid-solution metastable beta phase condition, which allows rolling of rods, sheets, foils, and other products at ambient temperature or in low (alpha + beta) region. Application of rapid heating as the final solid solutionizing treatment is supposed to allow formation of extremely fine beta-grain microstructure ensuring a sufficient ductility even in a high-strength condition. Detailed investigations of phase and microstructural evolution at continuous heating of solid solution and subsequently cold or warm rolled beta phase will be performed in order to establish the practical application of novel RHT technology.

15. SUBJECT TERMS

EOARD, Materials, Metallurgy & Metallography, Titanium, forming, beta, melting, VAR, EBM, electron beam

16. SECURITY CLASSIFICATION OF:			17. LIMITATION OF ABSTRACT	18, NUMBER OF PAGES	19a. NAME OF RESPONSIBLE PERSON
a. REPORT	b. ABSTRACT	c. THIS PAGE			CHARLES H. WARD, Lt Col, USAF
UNCLAS	UNCLAS	UNCLAS	UL	130	19b. TELEPHONE NUMBER *(Include area code)* +44 (0)20 7514 3154

Science and Technology Center in Ukraine

G.V. Kurdyumov Institute for Metal Physics National Academy of Sciences, Ukraine

Partner Project # P-057

Advanced processes for high-strength titanium alloys".

Final report

Project manager: Prof. Orest M. Ivasishin

Kyiv 2004

Under the project P-057 the following activities were performed:

1) To investigate macro- and microsegregation, macro- and microstructure, loses of alloying elements during melting, content of melting impurities in the EBM round ingots in comparison with available data for the same materials produced with VAR process;
2) To investigate influence of type of raw materials used in feed stock on uniformity of chemical composition, loses of alloying elements during melting, microstructure and texture of EBM ingots;
3) To study influence of ingot geometry (shape: round or rectangular, various cross-section), on uniformity of chemical composition, microstructure and texture of EBM ingots;
4) To study influence of thermal conditions on uniformity of chemical composition, microstructure and texture of EBM ingots, in particular the influence of additional heating achieved with EB scanning in solidification zone which results in convection flows within the melt;
5) To study influence of precise dosed supply of liquid metal into solidification zone on uniformity of chemical composition, microstructure and texture of EBM ingots;
6) To develop thermo-physical model of EBM process that will include power and regime of EB scanning of EB guns, mode of feed stock and rate of liquid metal dosed supply into solidification zone, temperature gradient and solidification rate in mould resulting in different type of ingots with optimized composition and microstructure;
7) To study microstructure and texture evolution during cold or warm deformation and subsequent continuous rapid heating of different titanium beta alloys from point of view of interaction between beta phase decomposition, recovery and recrystallization;
8) To investigate processes of cold or warm deformed as well as rapidly heat treated beta alloys strengthening on further aging from point of view of final microstructure and properties formation;
9) To study microstructure / properties relationships in fine-grained beta alloys processed with using deformation - rapid heating approach.

During project fulfillment the following main results were obtained:

A) In part concerning EBCH melting:

Electron Beam Cold Hearth Melting (EBCHM) technology for production of ingots and slabs of titanium alloys was developed. Characterization of single-melt Ti-6Al-4V confirmed that high quality could be achieved with EBCHM technology. Experience attained with Ti-6Al-4V was used for production of more complicated, multicomponent alloys VT22, and T17. Modeling was developed for prediction of EBCHM ingot composition and structure depending technological parameters employed.

1) It was shown that EBCHM technology provides even after single remelting close control of chemical composition, macro- and micro- chemical homogeneity in round ingots and rectangular slabs of titanium alloys, as well as guarantees the removal of hard α- type inclusions and high density inclusions. EBCHM technology allows to employ for initial melting charge of both titanium sponge and titanium scrap together with master alloys and/or pure alloying metals. The chemical composition and structure of EBCHM ingots of titanium alloys do not depend on type of raw materials in feedstock.
2) It was established that, in contrast to VAR melting of titanium ingots, during EBCHM macrostructure and crystallographic texture can be controlled even in production of rectangular slab due to solidification control by EB-heating of melt in the mold. The chemical and microstructural homogeneity coupled with the development of an equiaxed beta grain structure during solidification may be beneficial with regard to the reduction in the amount of primary beta working that

must be done prior alpha/beta processing as well as the homogeneity in properties of semi-finished and finished products relative to location in the initial ingot.

3) It was shown that comparatively simple thermomechanical processing of EBCHM ingots consecutively at temperatures of single-phase beta and then two-phase alpha+beta fields causes in formation of rather uniform microstructure and homogeneous mechanical properties of rolled products. Mechanical properties rolled products made from EBCHM ingots are comparable to or even better than those achieved in wrought products derived from VAR ingots.

4) Models for predicting and controlling the final chemical composition of EBCHM titanium alloys were developed and validated under prototype- and full-scale-production conditions. Calculations demonstrate that melt loses during EBCHM are determined by the competition between diffusion to the melt surface and Langmuir evaporation at the melt surface. Generally, loses are limited by solute diffusion to the melt surfaces; the depth of the solute-depleted layer is much less than the melt pool depth. More quantitative insight into the melt loss problem was obtained in the frame of finite-domain and semi-infinite diffusion models. Input data for the models comprised values of the diffusion coefficient, evaporation-rate constant, and the characteristics of the melting process itself (*e.g.*, melting temperature, residence time in the hearth, and melt-pool depth).

5) Thermo-physical modeling was developed to describe the thermal conditions of ingots/slab solidification during EBCHM. This modeling was applied to predict the effect of the process parameters (melting rate, power input to the melting hearth and mold) on final ingot/slab structure, and showed rather high practical

applicability. Results of modelling were confirmed experimentally and allowed to conclude following:

a) ingot macrostructure is dependant on electron beam heating power put into solidification zone in mold that opens an additional way to control cast material texture and macrostructure.

b) dosed supply of liquid metal into solidification zone has negligible, within investigated technological range, influence on macrostructure of cast material.

A) In part concerning titanium beta-alloys:

Technological approach which included solid solutioning, cold deformation, rapid recrystallization, and aging with controlled heating rate to peak aging temperature was developed, based on comparative study of deformation, precipitation and recrystallization behavior as well as aging response of beta-alloys of different alloying systems.

1) Evolution of microstructure, substructure and texture of solid solutioned and then cold deformed four beta- alloys (VT22, TC6, Ti-15-3 and TIMETAL-LCB), which differ by total content of alloying elements and specific composition, was studied employing wide range of physical metallurgy methods. It was shown that cold workability of solid-solutioned beta alloys having the same initial phase ($\beta+\omega$) composition and same grain size may be different because it is controlled by the initial degree of grain subdivision by subgrains/sells and the corresponding processes by which imposed deformation is accommodated. In alloys characterized by a high degree of subgrain/cell formation (e.g., Ti-15-3 and TIMETAL-LCB),

straining proceeds readily by means of deformation and rotation within and adjacent to subgrains and cells. By this means, nonuniform deformation from one grain to another is easily accommodated, low stresses are generated at the grain boundaries, and cold ductility is high. In alloys with a poorly developed substructure (e.g., VT22 and TC6), the accommodation of imposed deformation is limited by the generation of large intergranular stresses arising from multi-component textures and stress-induced phase transformations. The cold workability of such alloys is thus relatively low.

2) Precipitation behavior during continuous heating following solution treatment and cold (or hot) working of the beta-titanium alloys VT22, TIMETAL-LCB, and Ti-15-3 was established using x-ray diffraction, in-situ resistivity measurements, optical and transmission electron microscopy. It was shown for cold-deformed materials that precipitation kinetics during continuous heating are most rapid for cold-deformed VT22 because of its low amount of beta-stabilizing elements. A variety of precipitation reactions (e.g., $\beta \rightarrow \beta + \omega$; $\beta \rightarrow$ orthorhombic $\alpha'' \rightarrow \alpha$) as well as reversion of martensite occurs during heating. Precipitation of the omega and alpha phases in the more-highly-alloyed materials (TIMETAL-LCB and Ti-15-3) is slower than in VT22. The high diffusivity of iron enhances precipitation in TIMETAL-LCB relative to that in Ti-15-3.

3) Recrystallization behavior during continuous heating of three beta alloys VT22, TIMETAL-LCB, and Ti-15-3 was compared. It was shown that it is difficult to obtain a uniform, fine recrystallized microstructure in VT22 due to the limited cold reduction that can be imposed without failure prior to continuous annealing. Such a deficiency can be overcome by *hot* pre-deformation to large strains. In this case, the

wrought structure contains a high dislocation density and primary alpha particles. Subsequent heating at a high rate leads to the initiation of recrystallization prior to the solutioning of the alpha particles whose presence prevents the growth of the recrystallized beta grains. High cold reductions and high heating rates lead to refined grain sizes during continuous annealing of Ti-15-3 and TIMETAL-LCB. For a given set of processing parameters, the grain sizes in Ti-15-3 tend to be slightly coarser because of the lower rates of diffusion, which control the kinetics of the recrystallization process. Rapid solution treatment prior to cold reduction and continuous annealing leads to finer recrystallized beta grain sizes due to its beneficial effect on the as-solutioned-treated beta grain size.

4) It was shown that beta-titanium alloys exhibit faster aging response in the fine-grained condition as compared to coarse-grained one due to residual defects and /or stresses, which accelerate the diffusion of alloying elements.

5) It was found that microstructures and properties that are developed in beta-titanium alloys during aging are a strong function of the heating rate to peak temperature. Slow heating to peak temperature enables precipitation of athermal omega during heat-up, thus providing nucleation sites for subsequent formation of equiaxed alpha, orthorhombic α'', and finally fine plate-like alpha lathes that provide high strength. The formation of α'' during isothermal aging is attributed to the generation of matrix stresses that drive the $\alpha_{equiaxed} \rightarrow \alpha''$ reaction. The optimal balance of strength and ductility is obtained when such a precipitation sequence is developed in alloys, which have been previously rapidly solution treated to obtain a fine beta grain size (~10 μm). Also it was shown that alternative way of commercial heat treatments may include an intermediate step in the omega-precipitation temperature regime can

be designed to provide the same beneficial microstructure and hence properties as cycles involving very slow continuous heating to the peak aging temperature. Rapid heating to the peak aging temperature avoids the formation of omega phase and thus leads to the direct precipitation of coarse plate-like alpha. Such microstructures lead to inferior strength. However, reasonable ductility may be retained if a fine beta grain microstructure has been developed prior to the final aging sequence. The effect of heating rate on microstructure evolution during heat-up to peak temperature has a noticeable effect on subsequent aging behavior at the peak temperature and thus should be taken into account in the design of industrial heat-treatment practices.

6) Comparison of recrystallized and polygonized conditions showed that the better balance of strength and ductility was observed in the first case. Study of fine microstructure of material in Rapidly Polygonized condition showed a high density of residual deformation defects. The difference in precipitation microstructure after slow and fast heating to aging temperature was essentially smaller as compared to Rapidly Recrystallized condition because of heterogeneous mechanism of precipitation in which defects played most important role. As a result in both cases final microstructure and tensile properties were very close for both heating rates.

7) It was shown that tensile properties resulting from realization of proposed technological approach varied in a wide range depending on the parameters of separate operations. At optimized parameters the results were following for TIMETAL-LCB: YS=1600 MPa, UTS=1640 MPa, A_5=9.4%, RA=36.5%. For VT22, the finest obtained grain size was of about 50 μm because it was achieved not through cold, but hot deformation. It was concluded that high strength in excess of

1500 MPa balanced with reasonable ductility needs an essentially finer grain size and therefore is hardly to be possible in this alloy. Ti-15-3 due to very sluggish precipitation kinetics can not be strengthened to high values via single step reasonable duration aging. Better balance of tensile properties could be obtained using two-step aging or employing additional low reduction (of about 10-15%) cold deformation between stages of Rapid Recrystallization and aging.

8) Attention was paid to study of anisotropy in high-strengthened condition and its relation to the texture. Tensile properties were measured in longitudinal and transverse directions for some heat treatments of TIMETAL-LCB. It was found that Rapid Recrystallization (RR) allowed to form more isotropic (mechanically) condition of material as compared to conventionally ($\alpha+\beta$) treated conditions. The difference was at least partly related to the crystallographic texture. However, in recrystallized, fine-grained condition the texture was still rather strong. Heating to higher temperatures during RR caused in a more random texture but at the same time, in coarser beta-grain structure. So, dilemma to produce the more isotropic material or to allow grains to grow and thus, to deteriorate strength/ductility balance should be solved depending on a particular application of the heat-treated material.

Results were presented as three consecutive annual reports and technical papers [1-16].

Technical papers:

[1]. Ivasishin O. M., Semiatin S.L., Markovsky P.E., Shevchenko S.V. and Ul'shin S.V. Grain growth and texture evolution in Ti-6Al-4V during beta annealing under continuous heating conditions, Mat. Sci. & Eng. A, 337/1-2, (2002), pp.88-96.

[2]. O. M. Ivasishin, S. V. Shevchenko, N. L. Vasiliev, S. L. Semiatin, 3D Monte-Carlo Simulation of Texture-Controlled Grain Growth. Acta Materialia, 51, 2003, 1019.

[3]. Ivasishin O. M., Markovsky P.E. Matviychuk Yu.V. and Semiatin S.L. Precipitation and Recrystallization Behavior of Beta Titanium Alloys during Continuous Heat Treatment, Metall. Mater. Trans, A, 2003, Vol. 34A, pp. 147-158.

[4]. S.V. Shevchenko, O.M. Ivasishin, N.L. Vasiliev, S.L. Semiatin. 3D Monte-Carlo Simulation of Grain Growth in Polycrystalline Solids: Limits of the Potts Approach and Development of a Spatial-Scaling Procedure. "Materials Week 2002-Proceedings", Ed. Werkstoffwoche-Partnerschaft GbR, Publishier: Werkstoff-Informationsgesellschaft mbH, Frankfurt, 2003.

[5]. A.N. Kalinyuk, N.P. Trigub, V.N. Zamkov, O.M. Ivasishin, P.E. Markovsky, R.V. Teliovich , and S.L. Semiatin, Microstructure, Texture, and Mechanical Properties of Electron-Beam Melted TI-6AL-4V, Mat. Sci. & Eng., **A346**, 2003, #1-2, pp. 178-188.

[6]. O.M. Ivasishin, S.V. Shevchenko, P.E. Markovsky and S.L. Semiatin. Experimental Investigation and 3D Monte-Carlo Simulation of Texture- Controlled Grain Growth in Titanium Alloys. Proceedings of 10th world conference on Titanium, Hamburg, July 2003.

[7]. O.M. Ivasishin, P.E. Markovsky, et all., Precipitation and Recrystallization Behavior of Cold-Deformed Beta Titanium Alloys during Continuous Heat Treatment, Proceedings of 10th World Conference on Titanium 'Ti-2003', 13-18 July 2003, Hamburg, Germany.

[8]. O.M. Ivasishin, V.N. Zamkov, P.E. Markovsky, et all., Characterization of Electron-Beam Melted Ti-6Al-4V Alloy in Cast and Thermomechanically-Processed Conditions, Proceedings of 10th World Conference on Titanium 'Ti-2003', 13-18 July 2003, Hamburg, Germany.

[9]. O.M. Ivasishin, S.V. Shevchenko and S.L. Semiatin. Modeling of Abnormal Grain Growth in Textured Materials. Scripta Materialia, 50, 2004, pp. 1241-1245.

[10]. V.G. Ivanchenko, O.M. Ivasishin and S.L. Semiatin, Evaluation of Evaporation Losses during Electron-Beam Melting of Ti-Al-V alloys, Met. and Mat. Transactions B, 34B, #12, 2003, pp. 911-915.

[11]. S.L. Semiatin,V.G. Ivanchenko, S.V. Akhonin and O.M. Ivasishin, Diffusion Models for Evaporation Losses during Electron-Beam Melting of Alpha/ Beta- Titanium Alloys, Met. and Mat. Transactions B, 35B, #2, 2004, pp. 235-245.

[12]. S.V. Akhonin, N.K. Trigub, V.N. Zamkov, S.L. Semiatin Mathematical Modelling of Aluminum Evaporation during Electron-Beam Cold-Hearth Melting of Ti-6Al-4V Ingots, Met. and Mat. Transactions B, 34B, #4, 2003, pp.447-454.

[13]. O.M. Ivasishin, S.V. Shevchenko and S.L. Semiatin, 3D Monte Carlo (Potts) Modelling of Abnormal Grain Growth in Textured Materials, Metal Physics and Advanced technologies, 2004, v.26, #2, pp.269-286.

[14]. O.M. Ivasishin, P.E.Markovsky, S.L. Semiatin, and C. H. Ward, Aging Response of Coarse- and Fine-Grained Beta-Titanium Alloys, to be resubmitted to Mat. Sci. and Eng.

[15]. O.M. Ivasishin, P.E.Markovsky, Yu. V. Matviychuk, S.L. Semiatin, and C. H. Ward, Comparative analysis of high-strength conditions in titanium beta-alloys, (in Russian), CD Proceedings of International Conference "Titanium-2004 in CIS", probably to be published in 'Titanium' (Journal of Titanium Association of CIS).

[16]. H.V.Zhuk, P.A. Kobryn, and S.L. Semiatin, Influence of Heating and Solidification Conditions on the Structure and Surface Quality of Electron-Beam Melted Ti-6Al-4V Ingots; was sent to the Metallurgical and Materials Transactions B.

Science and Technology Center in Ukraine

G.V.Kurdyumov Institute for Metal Physics

E. O. Paton Institute for Electric Welding

Partner Project # P-057

"Advanced processes for high-strength titanium alloys"

Third annual report

(May 1, 2003 – April 30, 2004)

Project manager: Prof. Orest M. Ivasishin

Kyiv – 2004

Part 1

Activity #5: *To study influence of precise dosed supply of liquid metal into solidification zone on uniformity of chemical composition, microstructure and texture of EBM ingots.*

5.1. *Melting of Grade 5 ingots with precise dosed supply of liquid metal into solidification zone and their preliminary processing.*

5.2. *Study of precise dosed supply of liquid metal influence on uniformity of EBM ingots chemical composition.*

5.3. *Study of precise dosed supply of liquid metal influence on microstructure and texture of EBM ingots*

5.4. *Summarizing of obtained data and optimization of EBM parameters for Grade 5 and for more alloyed titanium alloys.*

Activity #6: *Development of thermo-physical model of EBM process that will include different process parameters.*

6.1. *Development of thermo-physical model of EBM process that will include different process parameters.*

6.2. *Study of liquid metal solidification mechanism under conditions of surface heating by scanning EB and dosed supply of liquid metal using proposed thermo-physical model of EBM.*

Investigation of influence of precise dosed supply of liquid metal into solidification zone on uniformity of chemical composition, microstructure and texture of EBM ingots.

Figures 1 – 8
Table 1

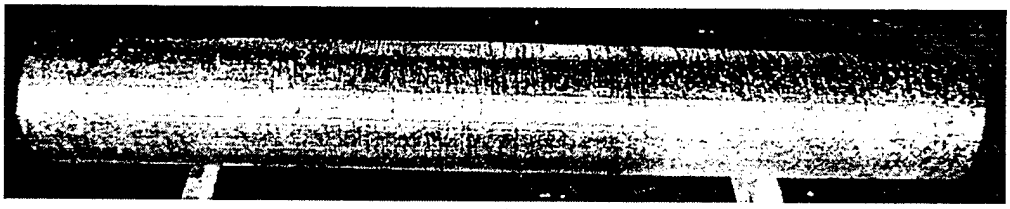

1

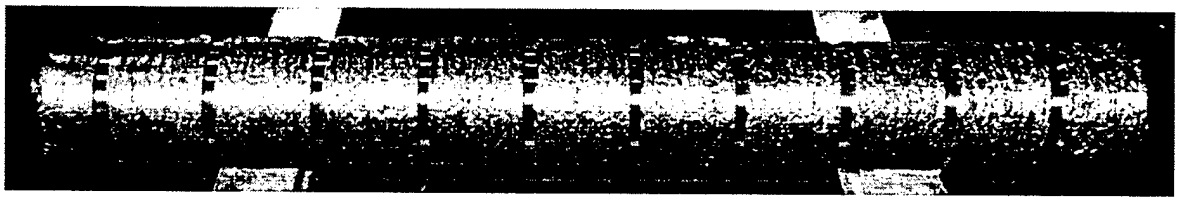

2

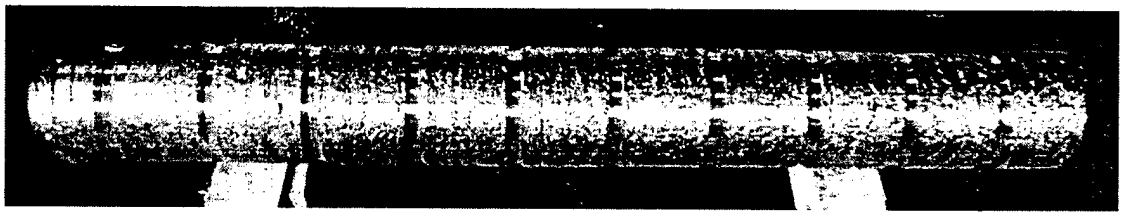

3

Figure 1. Ti-6Al-4V ∅200 mm ingots produced with different dosed supply.

Raw materials: titanium sponge Grade TG-130 88.0%, vanadium-aluminum master alloy VNAL (75%V-25%Al) 5.3%, metallic aluminum 6.7%

Horizontal feeding of raw material into melting zone.

Power of electron beam heating for charge melting 106 kW.

Power of EB-heating of melt in the mold in central and peripheral zones 9 kW and 15kW respectively.

Melting rate 43 kg/h.

Estimated temperature 2006 K

Table 1

Chemical composition of melted ingots

#	Melt dose kg	Interval between melt doses, s	Place of sampling	Chemical composition, %						
				Al	*V*	*Fe*	*C*	*O*	*H*	*N*
1	1.65	60	Top	6,10	3,99	0,14	0,011	0,11	0,002	0,022
			Middle	6,19	4,23	0,18	0,014	0,12	0,002	0,029
			Bottom	6,35	4,15	0,17	0,016	0,13	0,002	0,028
2	3.3	120	Top	6,19	4,20	0,13	0,019	0,11	0,002	0,024
			Middle	6,39	4,34	0,17	0,017	0,12	0,002	0,021
			Bottom	6,01	4,26	0,15	0,013	0,10	0,002	0,015
3	6.6	240	Top	6,23	4,36	0,14	0,012	0,14	0,002	0,017
			Middle	6,14	4,00	0,14	0,017	0,12	0,002	0,029
			Bottom	6,30	4,23	0,13	0,019	0,11	0,002	0,020

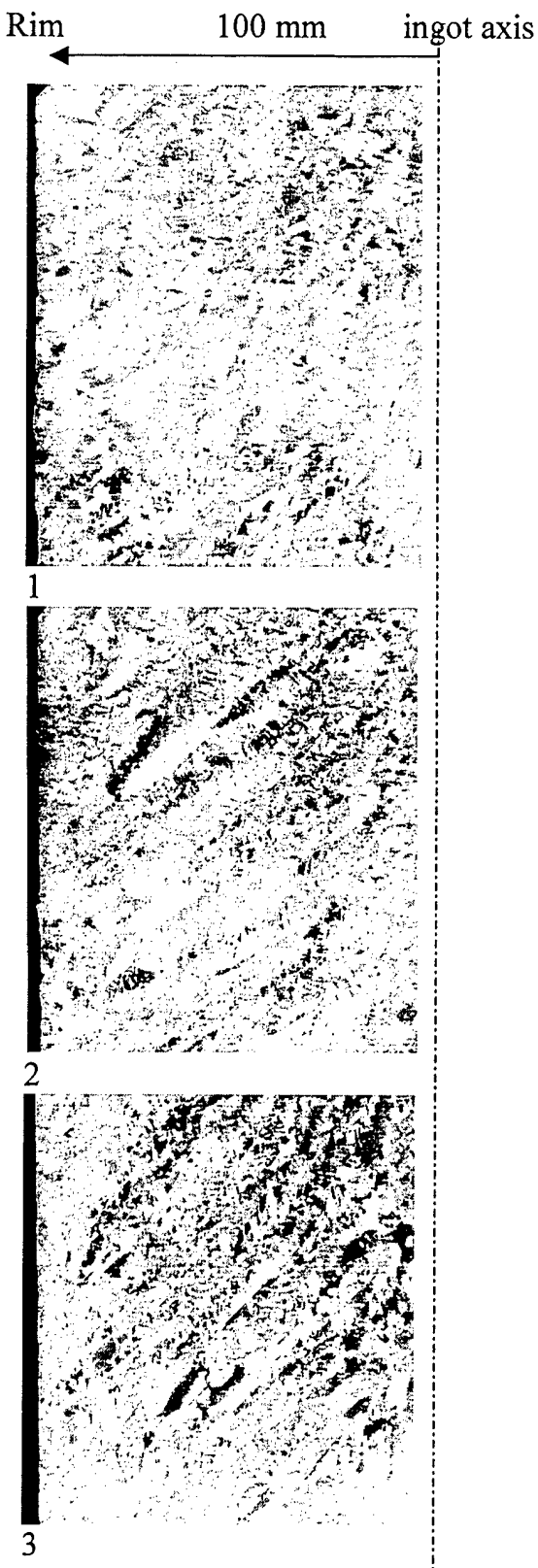

Figure 2. Ingots' macrostructure (appropriate numbers).

Macrostructure was most equiaxed in ingot #1. Some columnarity was observed in ingots ##2 and 3.

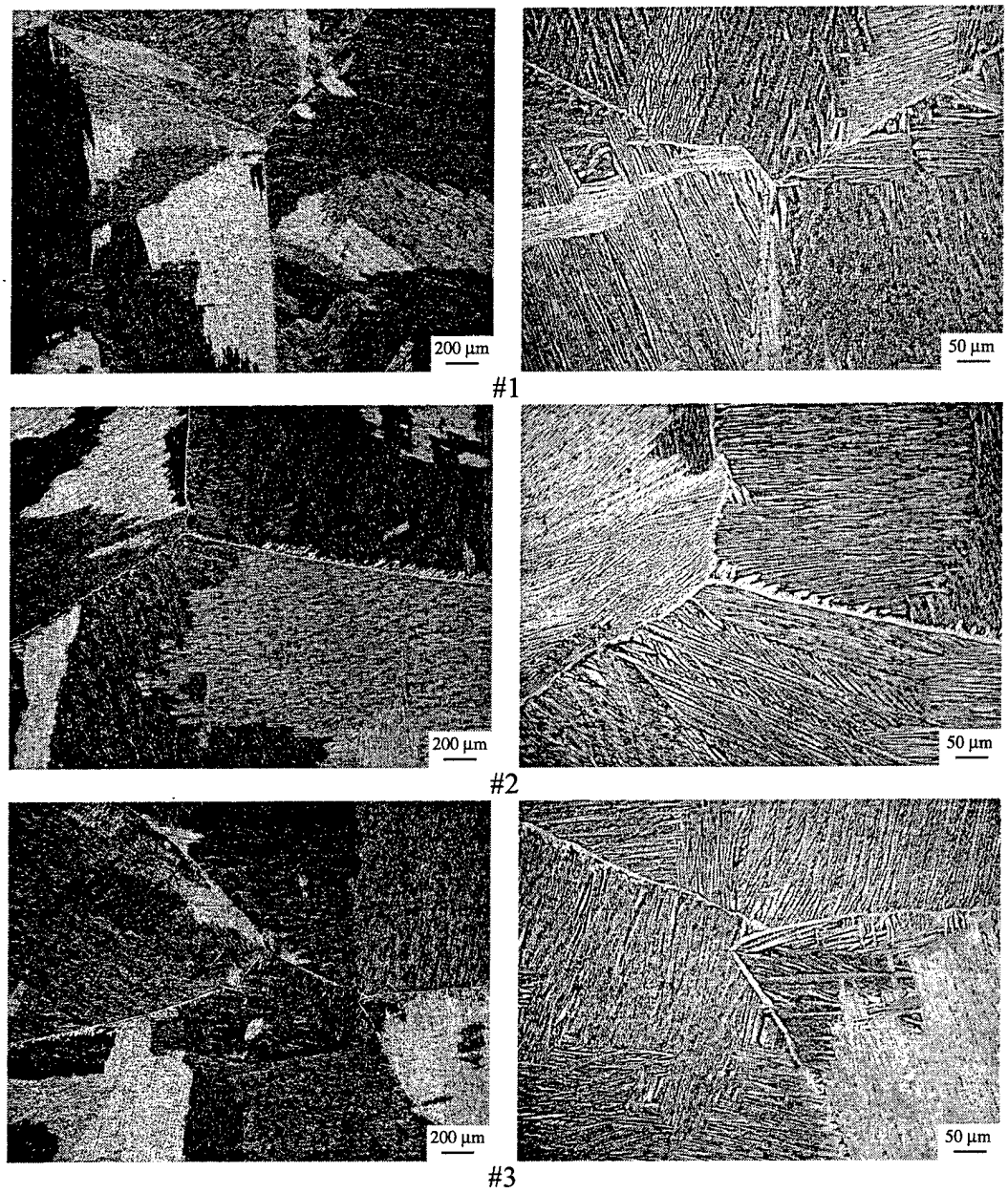

Figure 3. Typical microstructures of ingots.

In all studied ingots microstructure was similar and independent on melt dose.

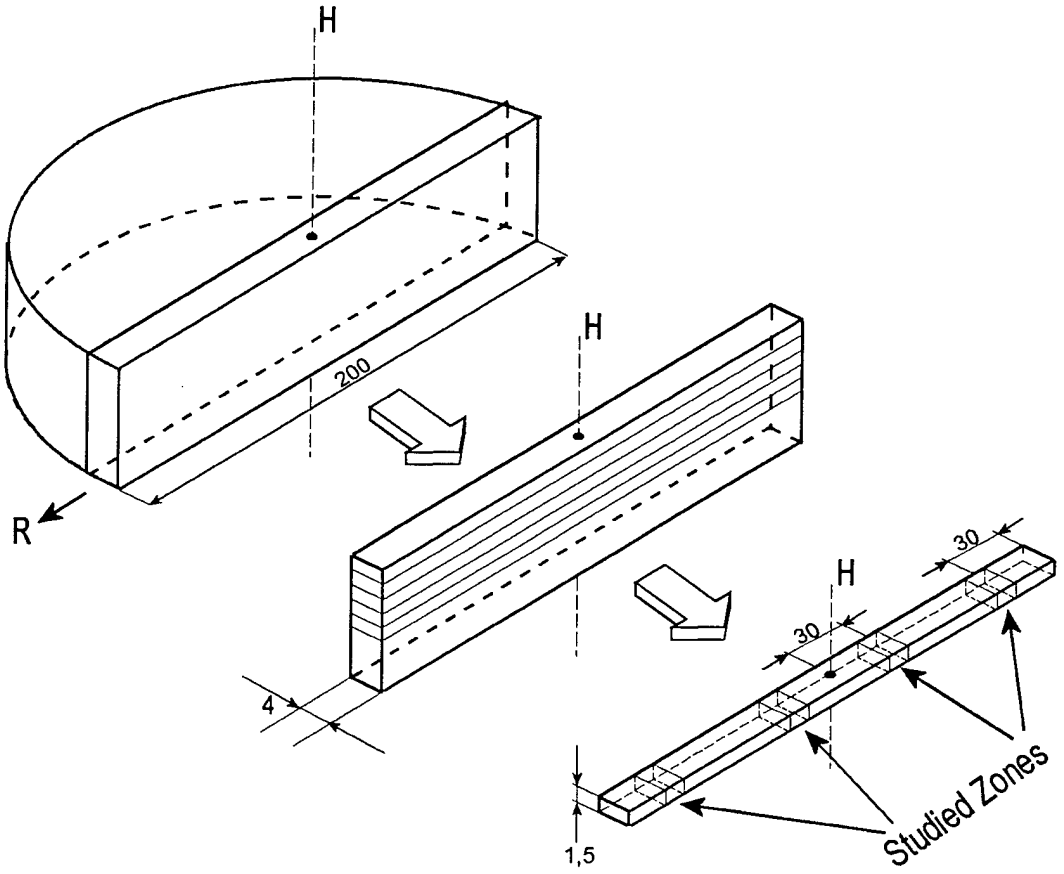

Figure 4. Scheme of specimen cutting.

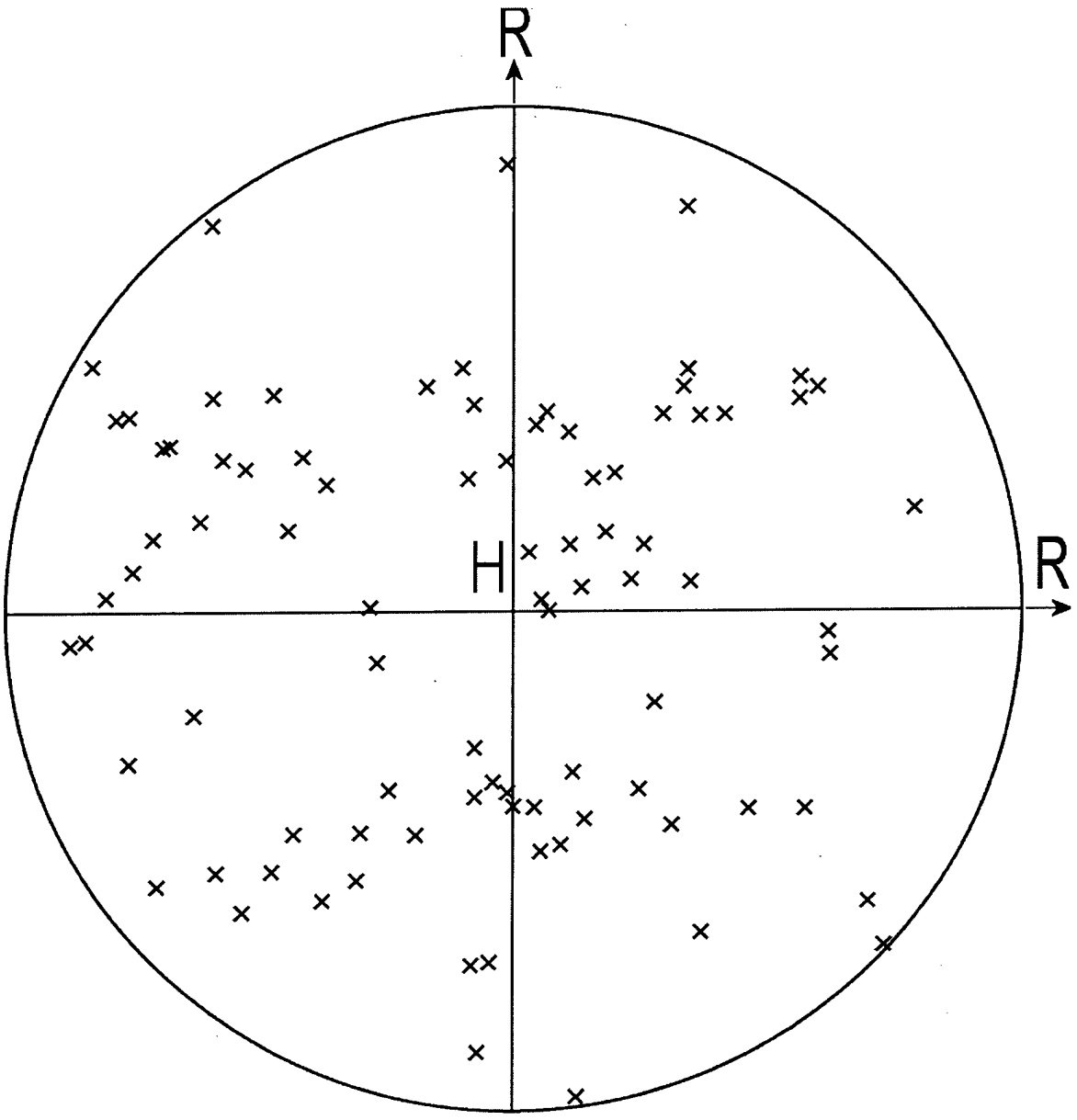

Figure 5. Stereographic projection of $\{200\}_\beta$ grain orientation distribution in ingot #1.

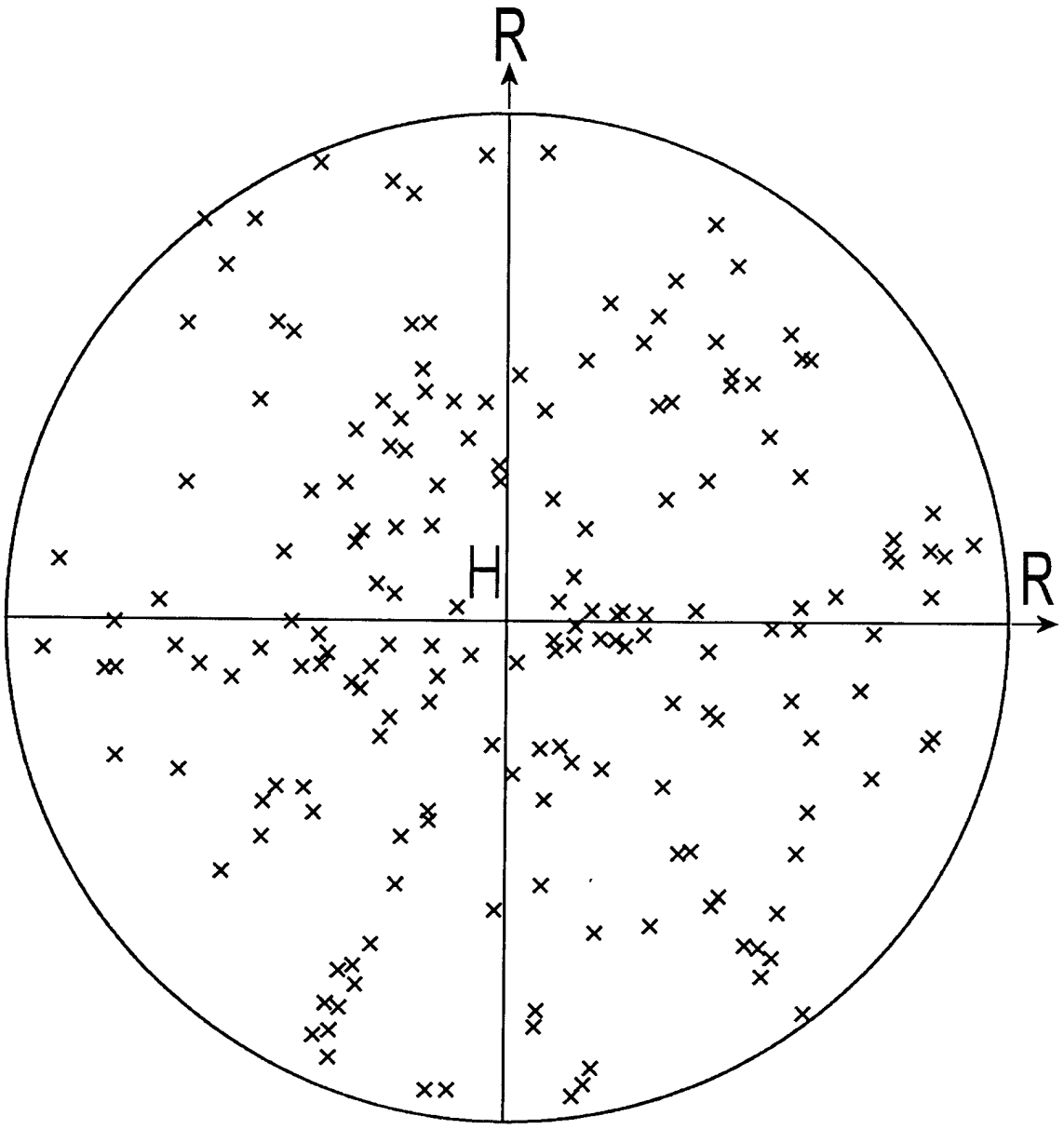

Figure 6. Stereographic projection of $\{011\}_\beta$ grain orientation distribution in ingot #1.

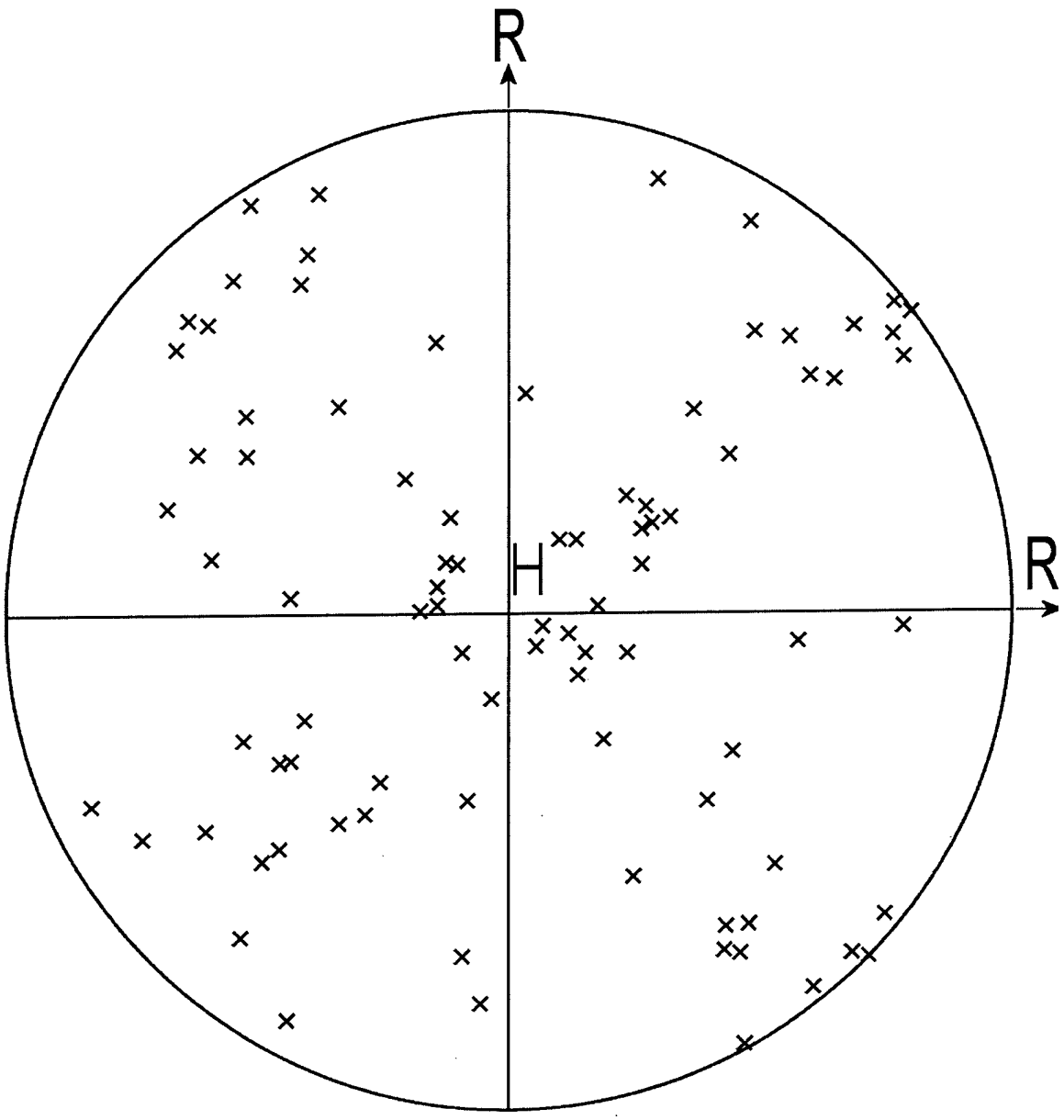

Figure 7. Stereographic projection of $\{200\}_\beta$ grain orientation distribution in ingot #3.

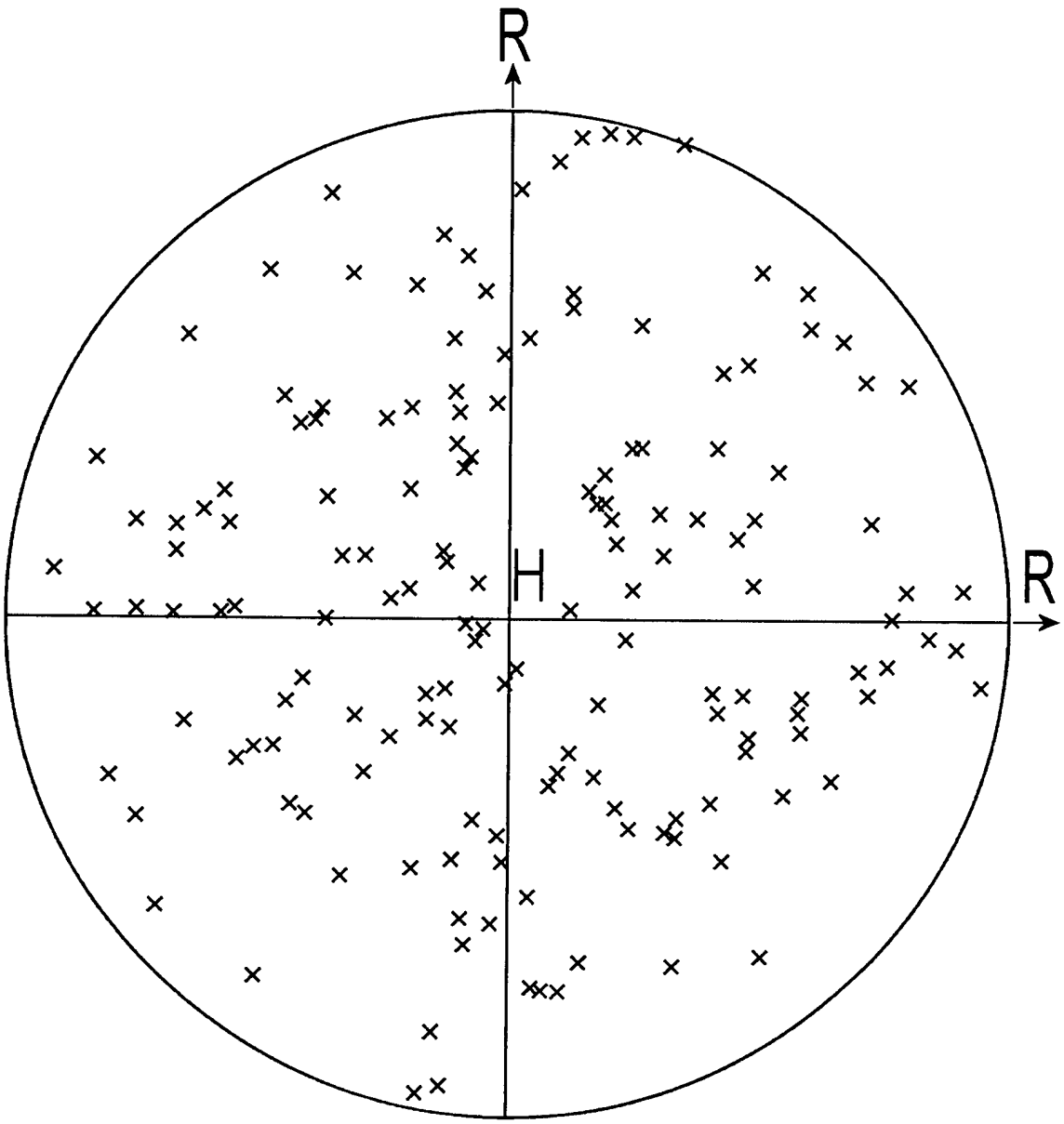

Figure 8. Stereographic projection of $\{011\}_\beta$ grain orientation distribution in ingot #3.

Texture analysis (orientation of beta-grains) was performed in the cylindrical Ø200 mm ingots ##1, 3. Random character of texture was observed in both ingots despite of some difference in macrostructure. As it was observed earlier slightly columnar type of macrostructure was not directly related to crystallization texture.

Modeling of dosed supply for round ingots

Figures 9 - 10

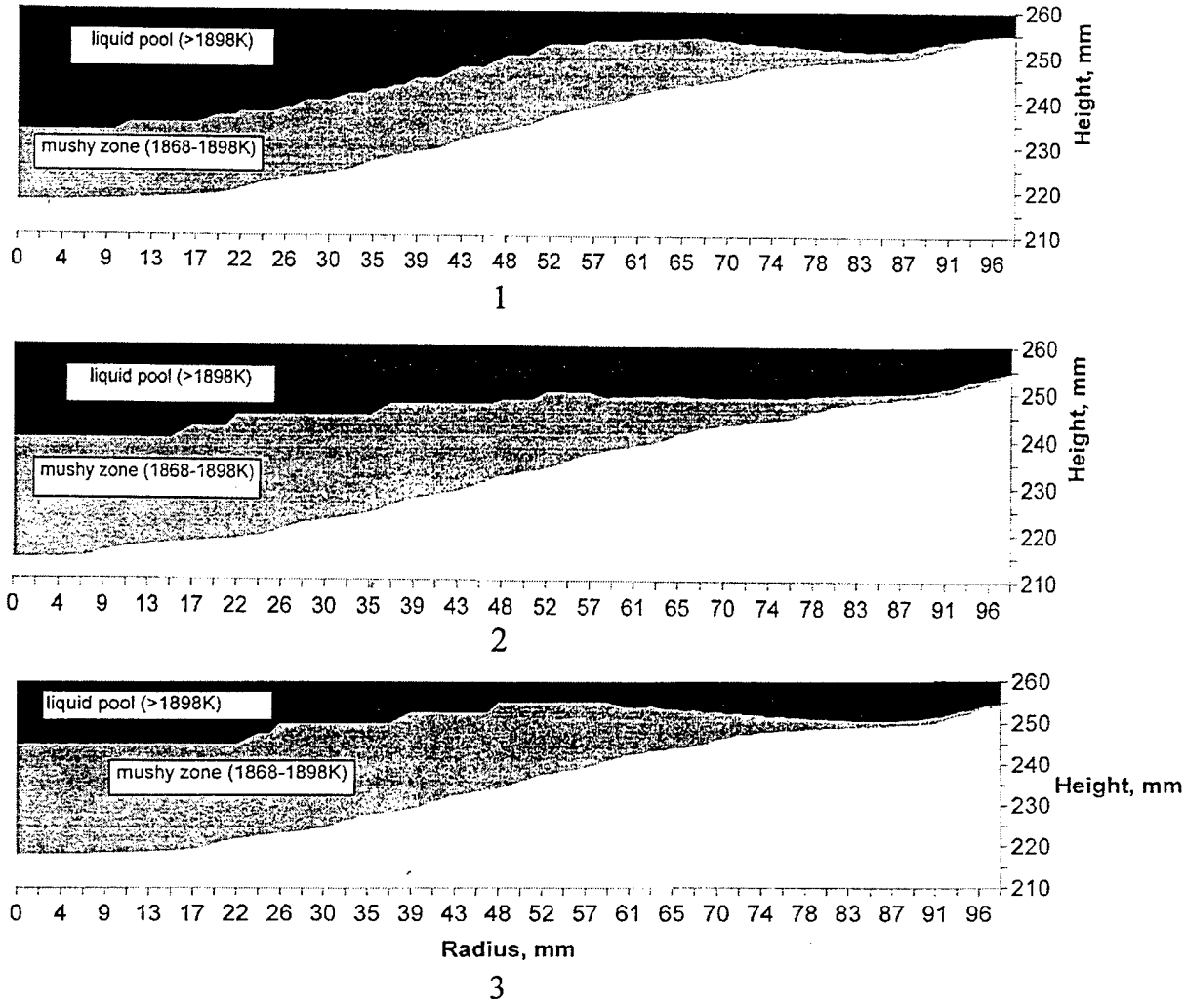

Figure 9. Temperature fields in ingot for different doses height and periods between supplies:
1 - 6 mm, 60 s;
2 – 12 mm, 120 s;
3 – 24 mm, 240 s.

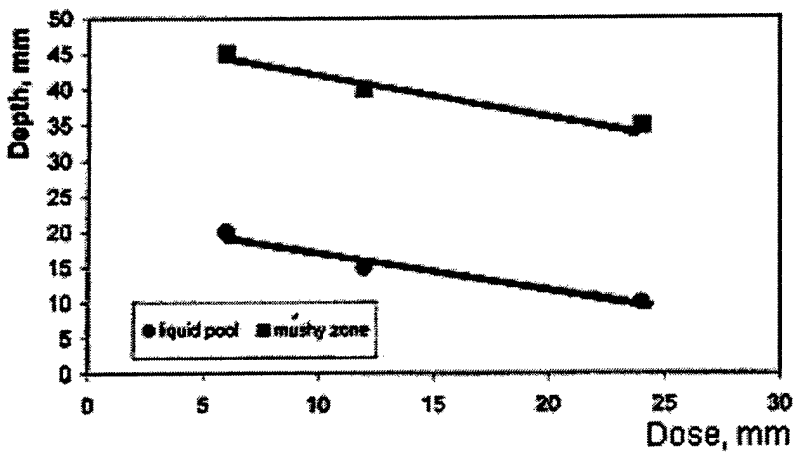

Figure 10. Dependence of liquid pool and mushy zone depth on dose.

In general, it may be concluded that for studied variation of dose it did not significantly affect the melt condition in mold what is in an agreement with the above experimental observations.

Additional experiments on rolling of slab #2

Figures 11 – 16
Table 2

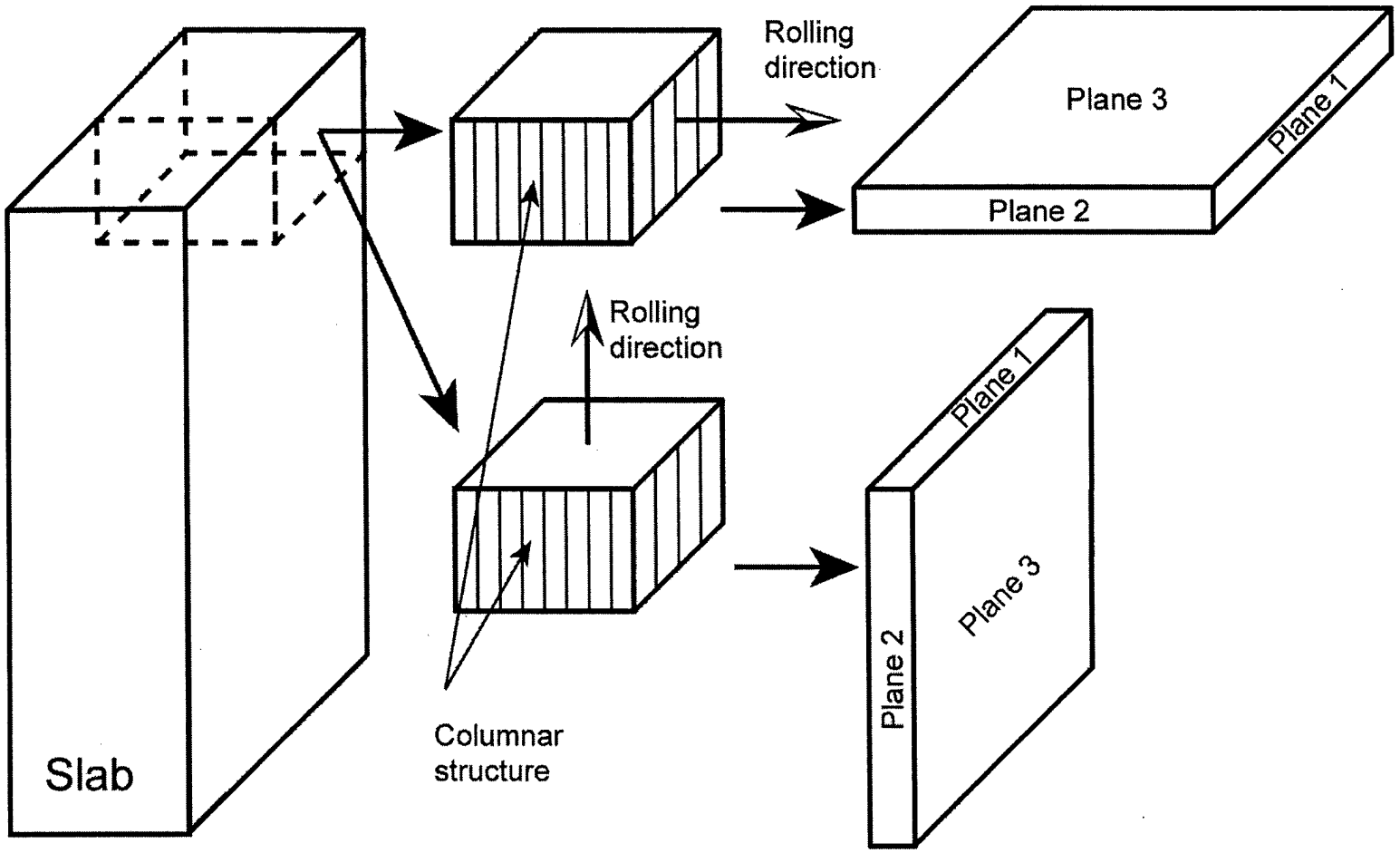

Figure 11. Scheme illustrating cutting and rolling of slab.

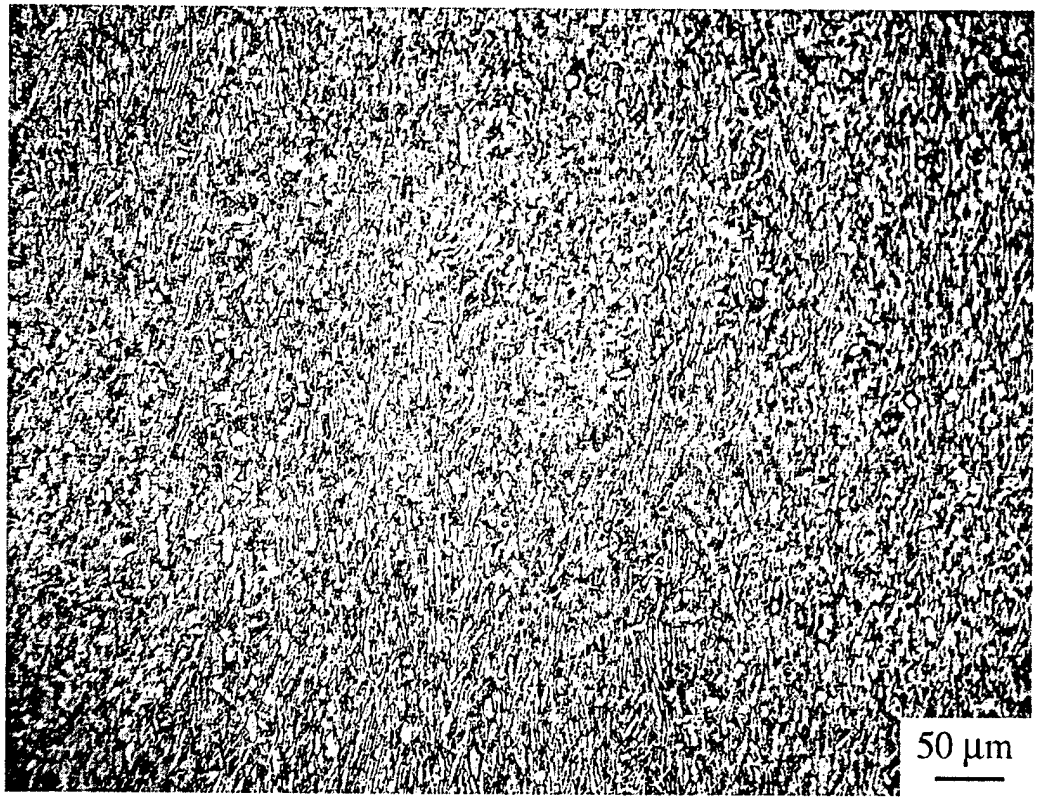

Plane 1

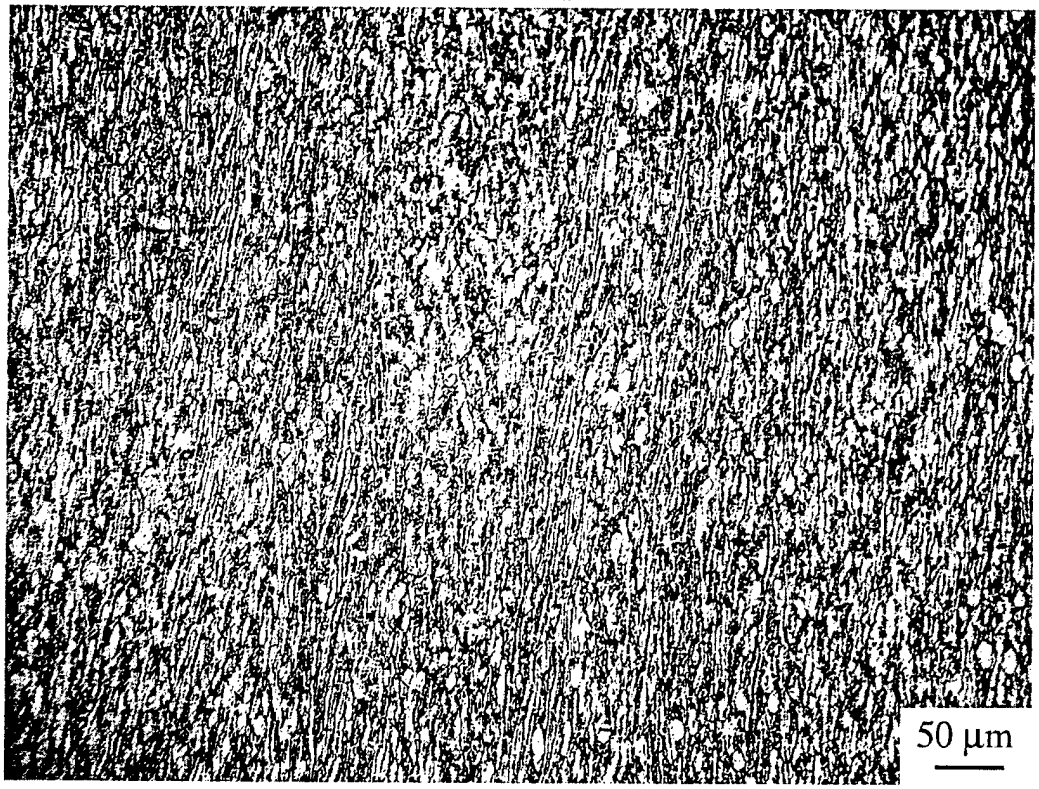

Plane 2

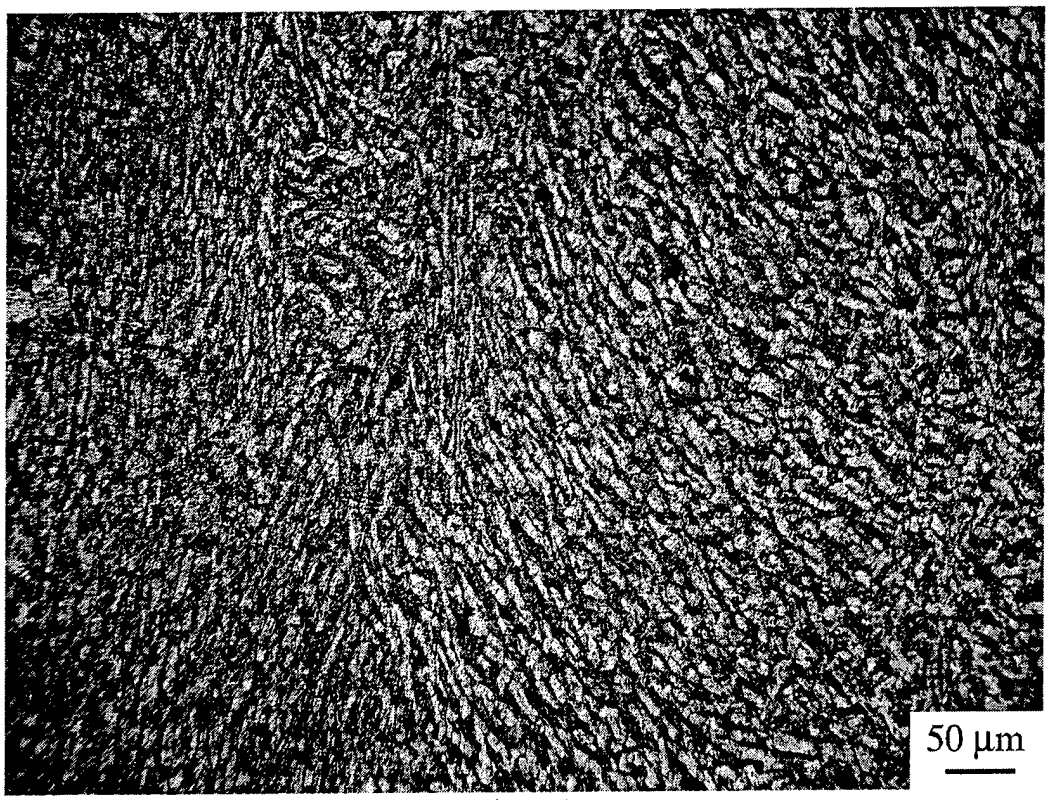

Plane 3

Figure 12. Microstructure of slab rolled along columnar crystals.

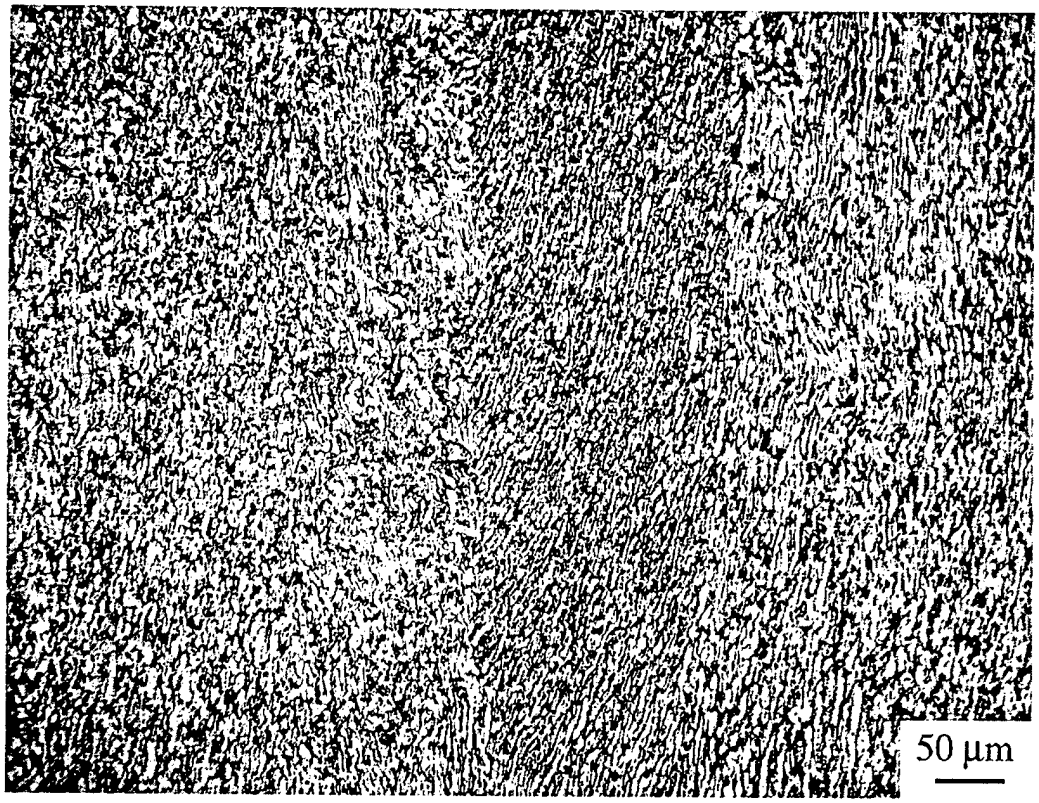

Plane 1

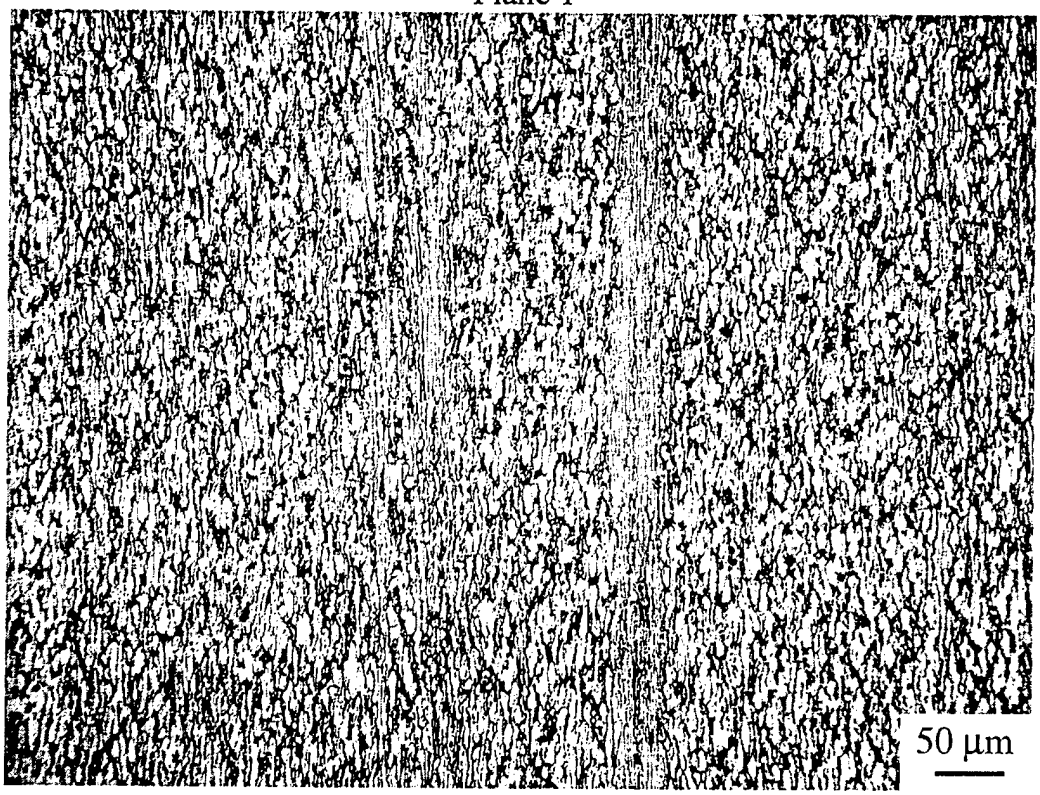

Plane 2

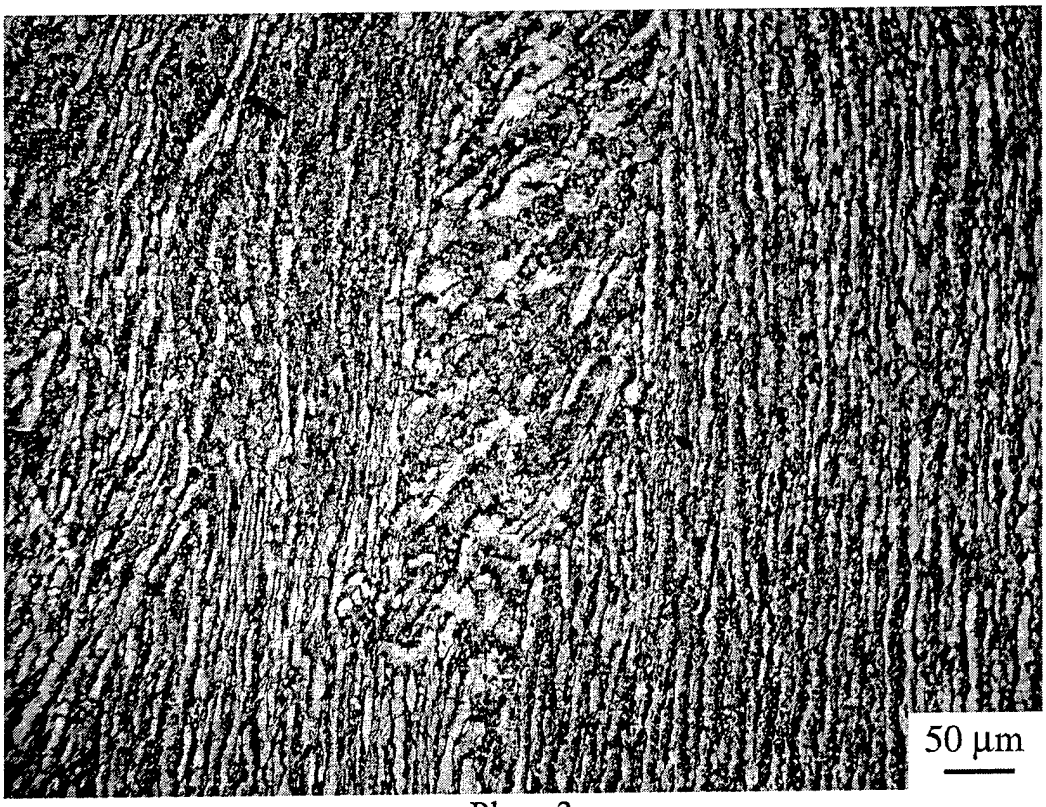

Plane 3

Figure 13. Microstructure of slab rolled across columnar crystals.

Textures of rolled slab

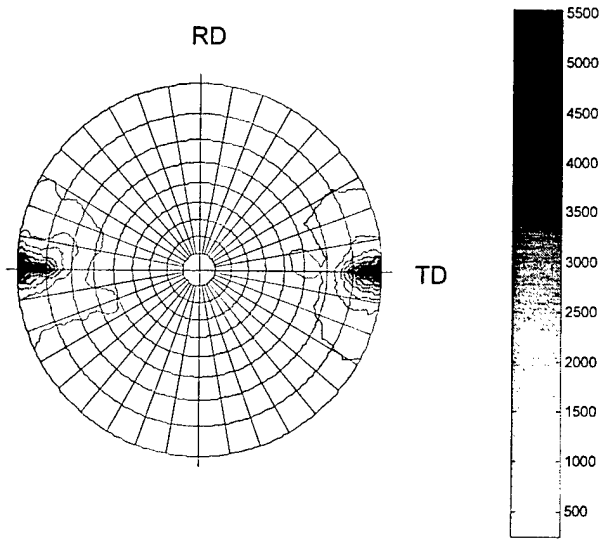

Figure 14. (0002)α pole figure of slab rolled along columnar crystals.

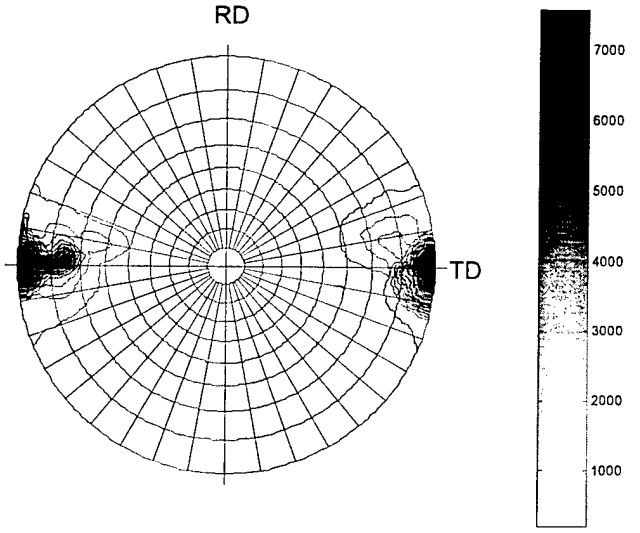

Figure 15. (0002)α pole figure of slab rolled across columnar crystals.

Change in a direction of rolling from along columnar crystals to across does not result in a change of a rolling texture. The transverse texture is formed in both cases. This texture is different from that achieved by rolling of round ingot. Thus, the presence of the crystallization texture influences final texture at the given rolling conditions. On the other hand, rolling along and across the columnar structure result in the same rolling texture because of symmetry of bcc crystal lattice (see Fig. 16).

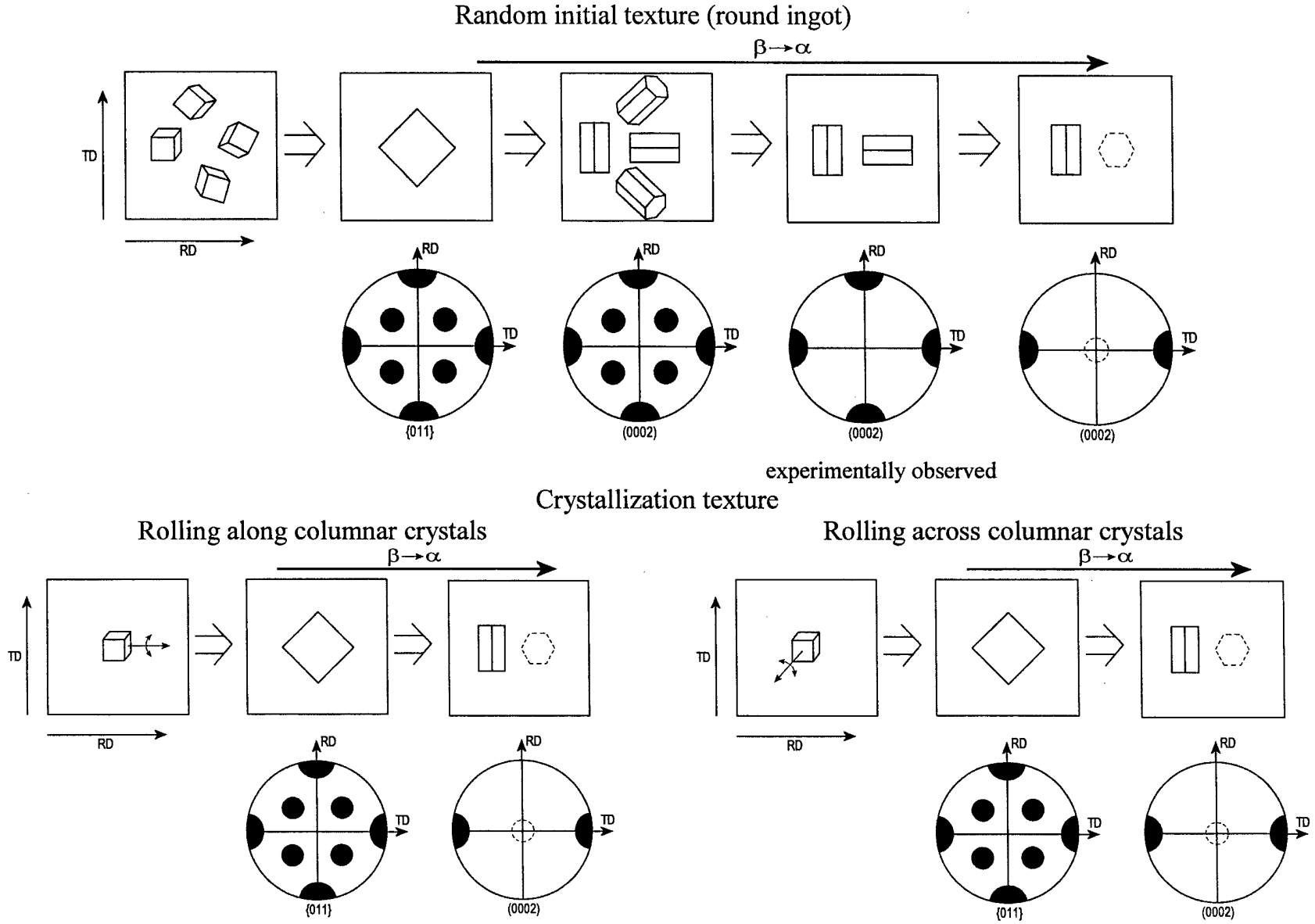

Figure 16. Schematic presentation of texture formation.

Table 2

Comparison of Mechanical Properties of Slab in Different Conditions

##	Metal Condition	Regime of Rolling	Rolling direction					Transverse direction				
			UTS, MPa	YS, MPa	A_5, %	RA, %	KCV, J/cm^2	UTS, MPa	YS, MPa	A_5, %	RA, %	KCV, J/cm^2
1	Cast	-*-	904	883	6	28	29	-	-	-	-	-
2	Rolled along crystals	50% β + 80 % α+β	1011	943	11	27	26	1123	1072	13	44	22
3	Rolled across crystals	50% β + 80 % α+β	953	878	10	27	31	1090	1040	12	49	27

Tensile properties in transverse and longitudinal directions are different what is in a good correlation with above texture data. On the other hand, difference between rolled along and rolled across is less then between transverse and longitudinal directions.

Temperature dependence of mechanical properties of Ti-6Al-4V material.

Comparative study of Ti-6Al-4V mechanical behavior in as-cast and hot rolled (plate 12mm) conditions

Figures 17 - 22

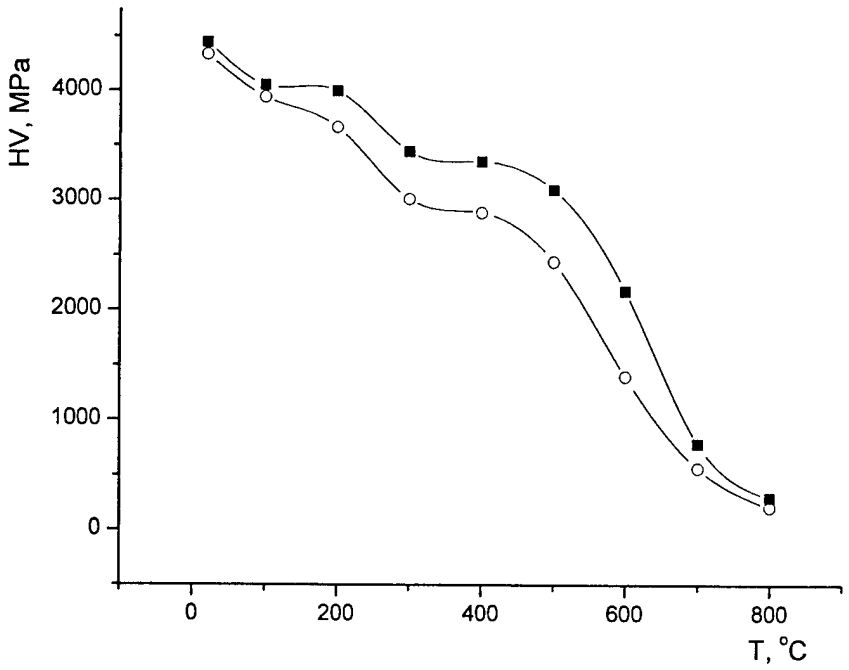

Figure 17. Hardness vs temperature for Ti-6Al-4V in hot rolled (solid symbols) and as-cast (open symbols) conditions.

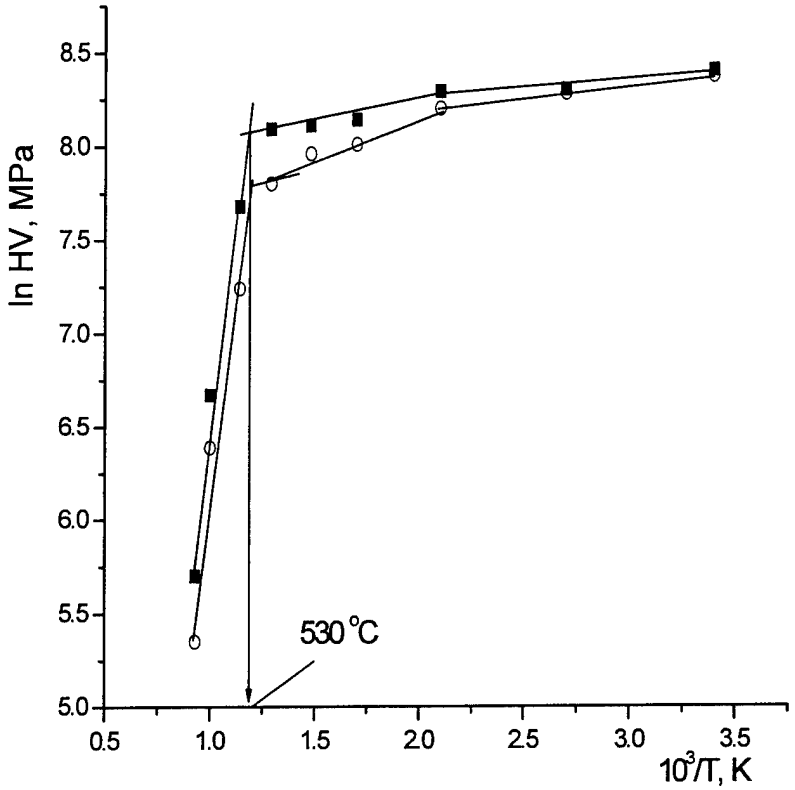

Figure 18. ln HV vs. 1/T for Ti-6Al-4V in hot rolled (solid symbols) and as-cast (open symbols) conditions.

At high temperatures activation energy became equal to the activation energy of self-diffusion (high-temperature deformation mechanism). Independently on alloy condition, this transition occurs at about 530°C.

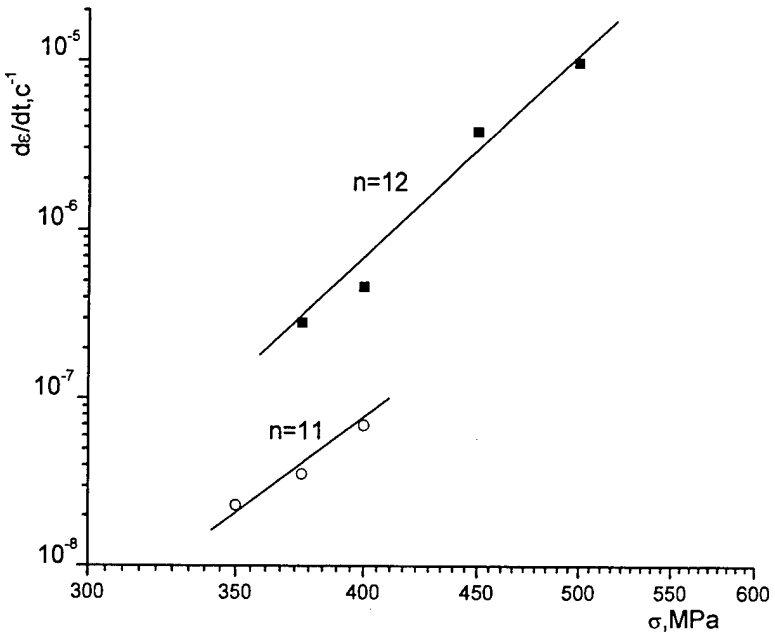

Figure 19. Minimum creep rate vs. stress for Ti-6Al-4V in hot rolled (solid symbols) and as-cast (open symbols) conditions at 450°C.

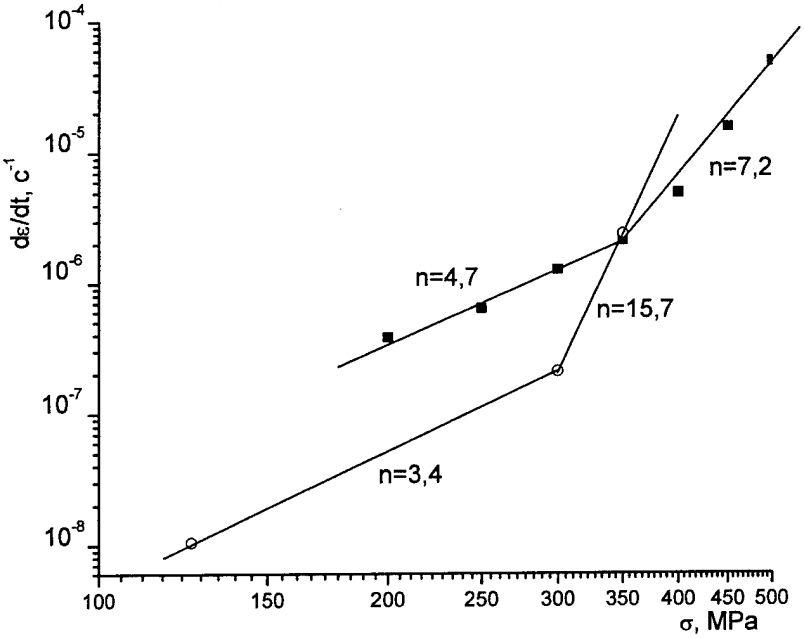

Figure 20. Minimum creep rate vs. stress for Ti-6Al-4V in hot rolled (solid symbols) and as-cast (open symbols) conditions at 500°C.

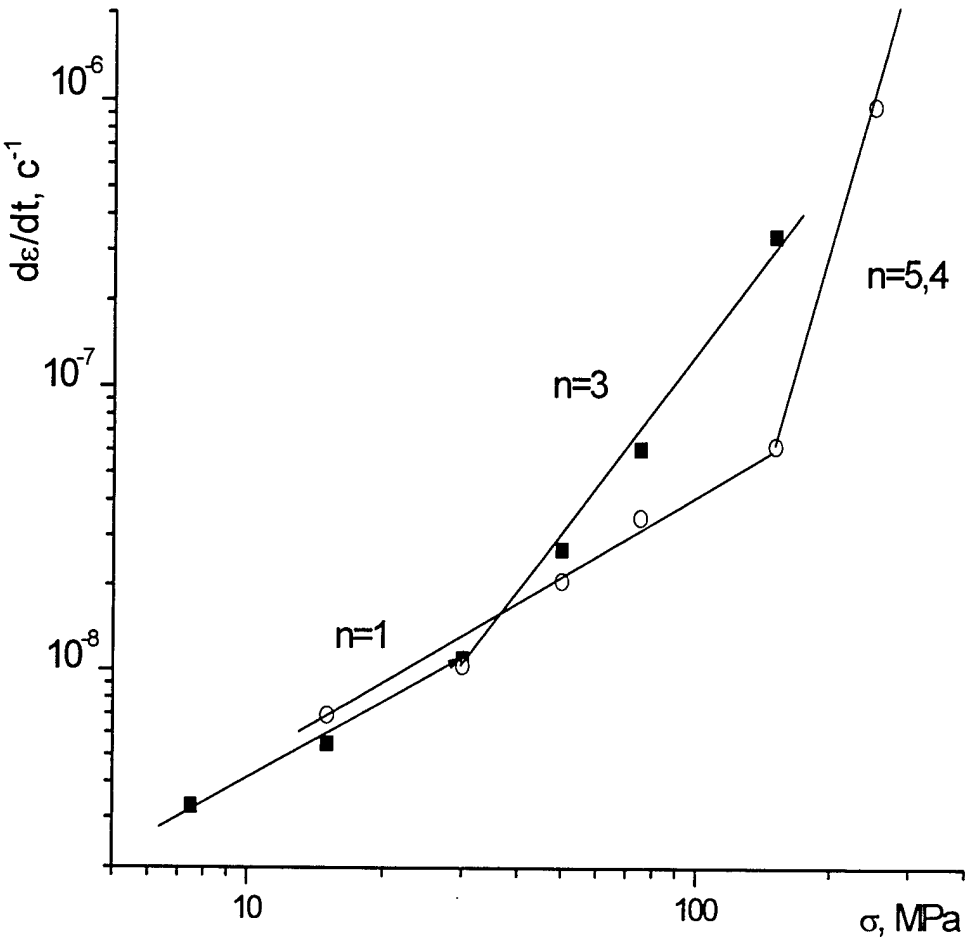

Figure 21. Minimum creep rate vs. stress for Ti-6Al-4V in hot rolled (solid symbols) and as-cast (open symbols) conditions at 600°C.

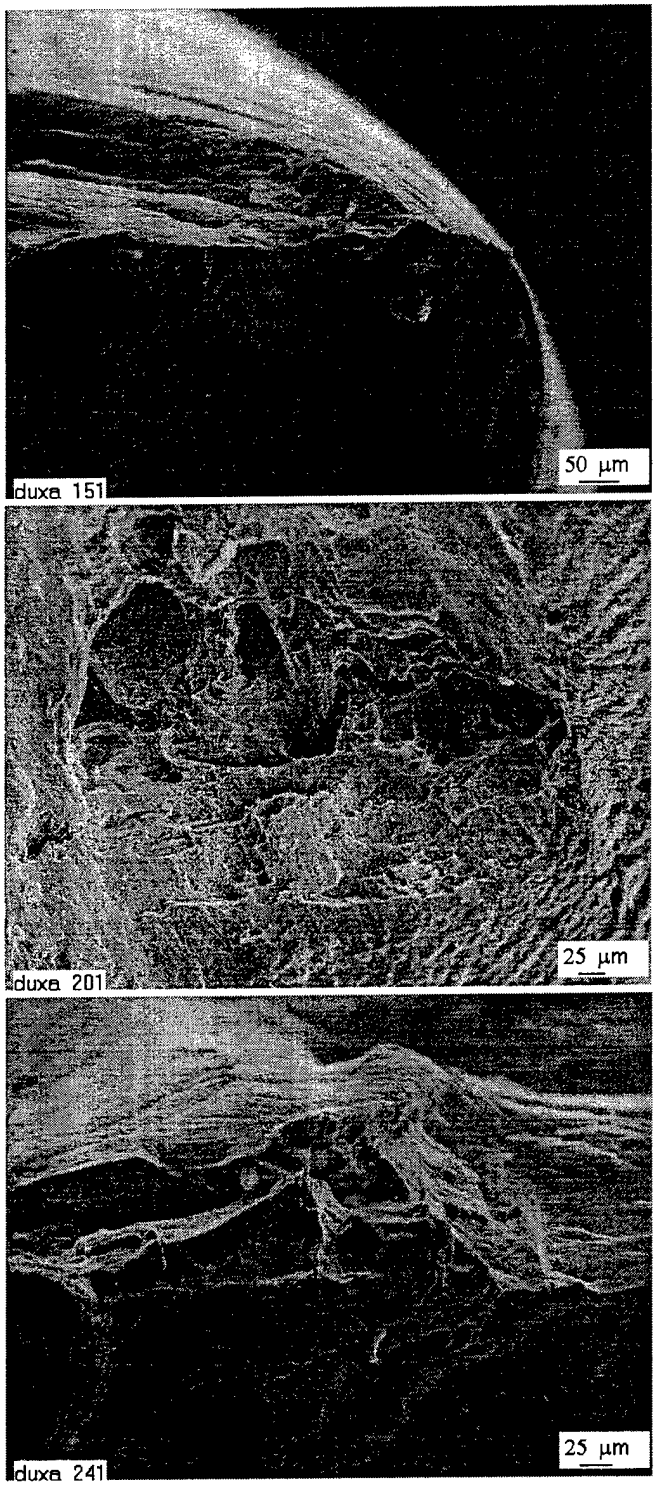

Figure 22. Fracture surface of as-cast Ti-6Al-4V tested at 500°C and 400 MPa.

Main conclusion was done that, in the temperature range of 450÷600°C creep mechanisms drastically changed. At 450°C power exponent n=11-12, deformation was controlled by cross-slip of screw dislocations. At 500°C and high stresses mechanism was the same, while at low stresses creep was controlled by edge dislocation climb (n=4.7 and 3.4 for deformed and as-cast conditions respectively). Finally, at 600°C and high stresses controlling mechanism was similar (n=3 and 5.4 for deformed and cast alloy respectively), while at low stresses it changed to diffusion creep of Nabarro-Herring type (n=1).

EBCH melting of multicomponent alloys (VT22 and Ti-17)

Figures 23 - 32
Tables 3 - 5

Modeling of alloying elements loses in Ti-Al-Cr system

Figures 23 – 29

The Prediction of Aluminum and Chromium Content in Ti-Al-Cr Ingots after Electron-Beam Cold-Hearth Melting

The main conceptions

1. The prognoses were limited only by evaluation of Ti, Al and Cr losses during electron-beam cold-hearth melting. The losses during melting of raw materials (consumable workpiece) and losses from mould were neglected.

2. The initial compositions of the melt in the cold-hearth are presented in Table 1 (see file Attach1.xls).

3. The rate of ideal evaporation of component *i* into vacuum (W_i) varies with temperature according to Langmuir's equation:

$$W_i\ [\text{кг/м}^2\text{с}] = P_i [M_i/(2\ \pi\ R\ T)]^{1/2} \qquad (1)$$

$$P_i = X_i\ \gamma_i\ P_i^0\ ,$$

X_i, γ_i і M_i – are the molar fraction, activity coefficient and molar mass of the evaporation species respectively; P_i – is the partial pressure of vapor of component *i* over the multicomponent melt ; R is the gas constant and P_i^o is the vapor pressure of pure component *i* above the melt.

The activity coefficients of the components γ_i were expressed through the partial Gibbs energies of Al and Cr at 2100, 2050 and 2000 K, which were calculated using thermodynamic properties of liquid of the binary Ti-Al and Ti-Cr system [COST 507]. They are presented in Table 2 (see file Attach1.xls).

4. The vapor pressures of pure Al, Cr and Ti were calculated using the Clausius-Clapeyron equation:

$$P_i^0 \text{ [Pa]} = 133 \cdot 10^{(-A/T+B)} \cdot T^C \ . \qquad (2)$$

The constants A, B and C as well as evaporation pressures calculated for 2000, 2050 and 2100 K are presented in Table 3 (see file Attach1.xls).

5.The impurity diffusion of Al in β-Ti is characterized by

$$D_{Al}^{(s)}(T) = 1.2\text{x}10^{-7} \exp[-150000/(RT)] \qquad (3)$$

[H. Araki, T.Yamane, Y.Minamino, Sh.Saji,Y.Hana, S.Boo Yung, "Anomalous Diffusion of Aluminum in β-Titanum", MMT, A, **25A** (4), 1994, p.874-876].

For Cr

$$D_{Cr}^{(s)}(T) = 8{,}42^{+6{,}39}_{-2{,}63} *10^{-6} \exp[-(208000\pm9000)/(RT)]*\exp[((36{,}6\pm6{,}4) *10^6)/RT_m^2] \ m^2s^{-1} \qquad (4)$$

[S.-Y. Lee, Y.Iijima, K.Hirano, "Diffusion of Chromium and Palladium in β-Titanium", Materials Trans. JIM, **32** (5), 1991, p.451-456]

The diffusivity of Al and Cr in liquid state were estimated assuming that the diffusion coefficient of a solid in its melting point is determined in accordance with equations (3) and (4), and the correspondent diffusivity of the liquid at the melting points is higher by a factor $K^{s-l} = 1.68 * 10^3$. In such way the diffusion coefficient of Al at 2100 K was numerically equal to one used in [2003Iva] but it's temperature dependence was another, namely such, as proposed by [1994Ara]. The Cr losses were calculated using two different values of diffusion coefficient. They were calculated by equation (4) using average and higher numerical coefficients. The

numerical values of diffusion coefficients are presented in Tables 4 (see file Attach1.xls) for two different parts of calculations.

5. The mass of charge in the cold-hearth was calculated using the volume of cold-hearth and density of the alloy. The melting time of this charge was calculated by dividing the mass of charge by value of melting rate. The melting times of 16.2 kg charge at different melting rates are presented in Table 5 (see file Attach1.xls).

6. The evaluation of Al and Cr losses was based on the physical conception presented by [2003Iva] and [2004Sem], that consists in the existing of the surface layer of the melt depleted by volatile components. The results of evaluation of the Cr, Al and Ti losses for different initial composition of charge, temperature of the melt and the melting rates are presented in Table 6 – 14 (see file Attach1.xls) for two different temperature dependences of the diffusion coefficient of Cr. The changes in surface composition during the first five seconds are presented too.

7. The final concentrations of components during E-B melting were calculated using these results. They are presented in the Tables (see file Attach1.xls & Attach2.xls) and in Figures 23-28.

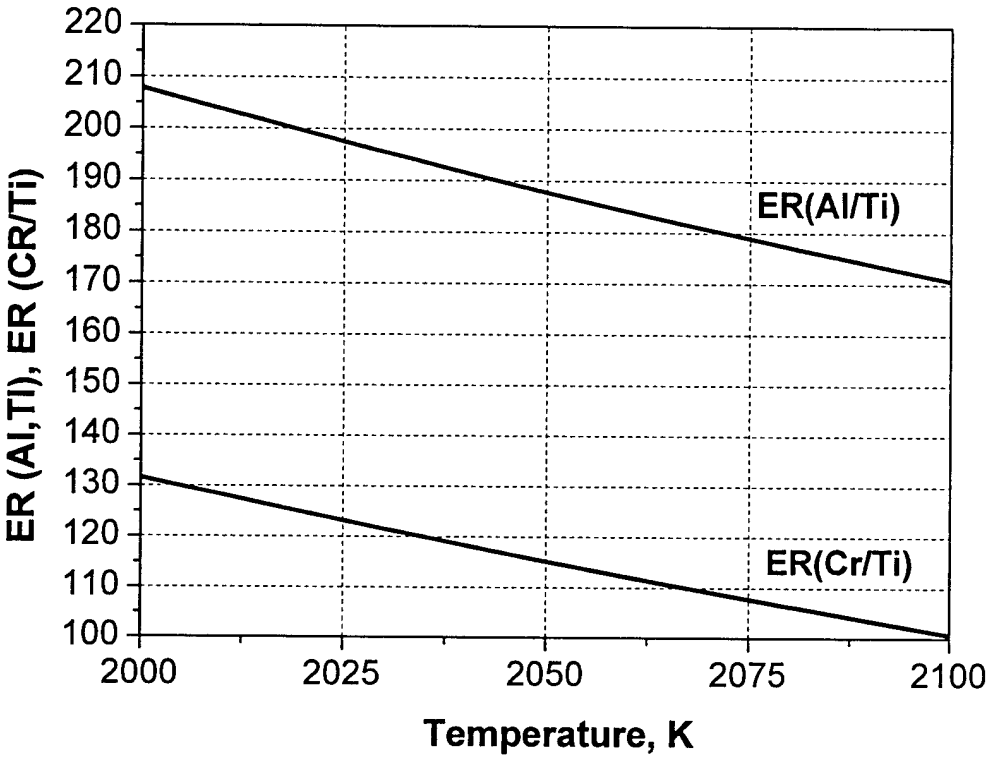

Figure 23. Evaporation Ratio of Al/Ti and Cr/Ti as a function of temperature.

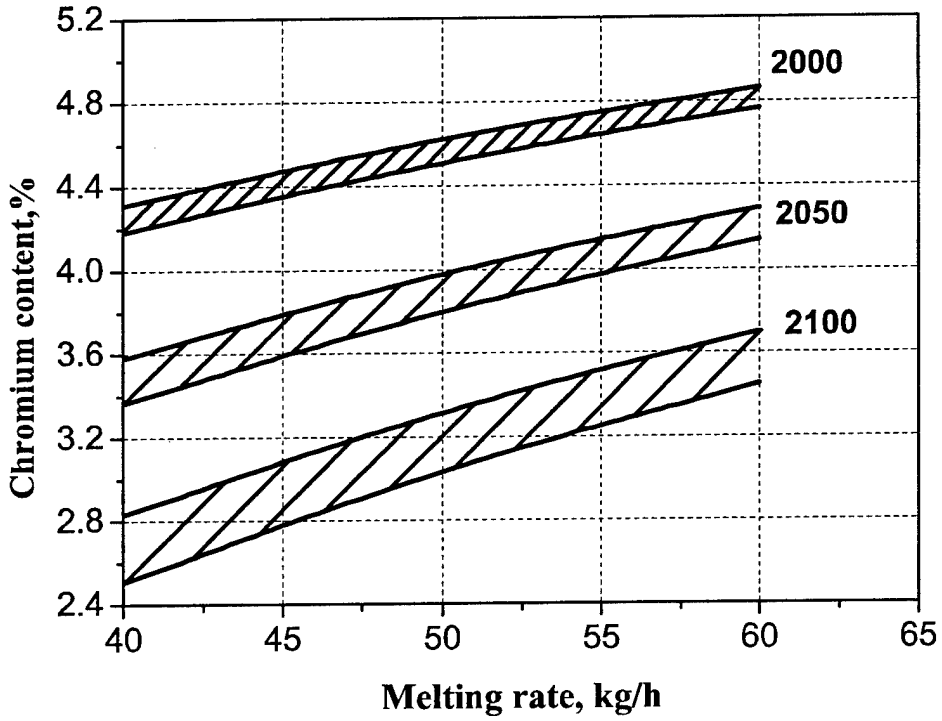

Figure 24. Model predictions of the chromium concentration in alloy Ti-Al-Cr ingot after melting in the 0.3x0.4 m^2 cold hearth as a function of melting rate at different temperatures of the melt for aluminum content of the initial charge $[Al]_0 = 6.3\%$, chromium content of the initial charge $[Cr]_0 = 6.5\%$.

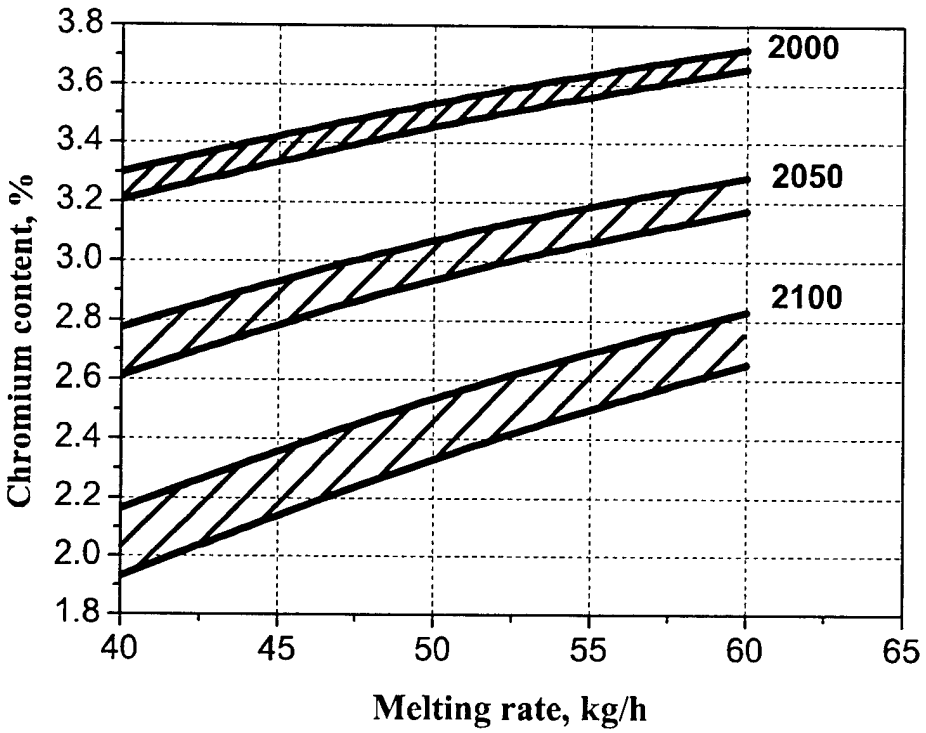

Figure 25. Model predictions of the chromium concentration in alloy Ti-Al-Cr ingot after melting in the 0.3x0.4 m^2 cold hearth as a function of melting rate at different temperatures of the melt for aluminum content of the initial charge $[Al]_0 = 6.3\%$, chromium content of the initial charge $[Cr]_0 = 5\%$.

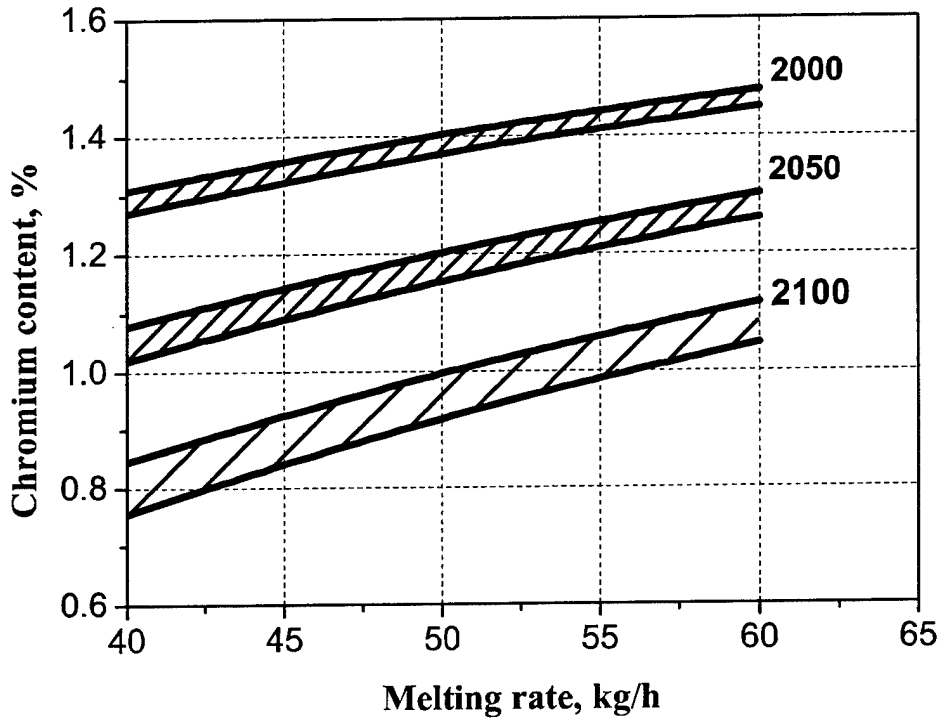

Figure 26. Model predictions of the chromium concentration in alloy Ti-Al-Cr ingot after melting in the 0.3x0.4 m^2 cold hearth as a function of melting rate at different temperatures of the melt for aluminum content of the initial charge $[Al]_0 = 6.3\%$, chromium content of the initial charge $[Cr]_0 = 2\%$.

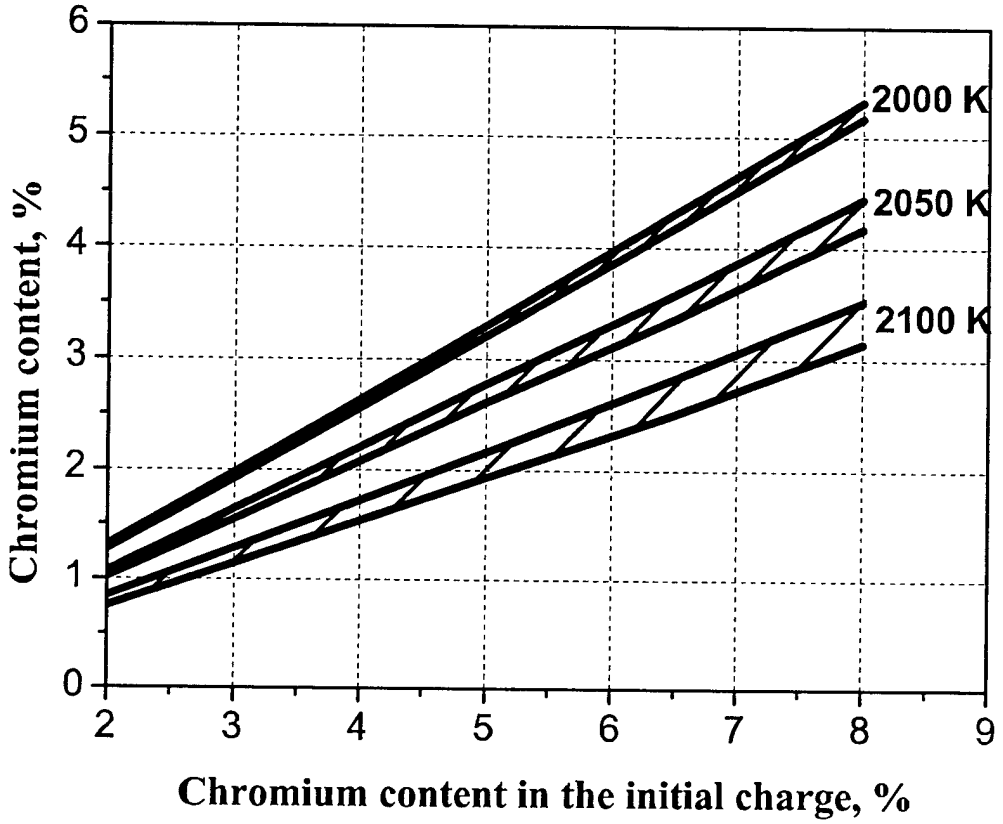

Figure 27. Model predictions of the chromium concentration in alloy Ti-Al-Cr ingot after melting in the 0.3x0.4 m^2 cold hearth as a function of the chromium content in the initial charge at melting rate 40 kg/h, aluminum content of the initial charge $[Al]_0 = 6.3$ % at different temperatures.

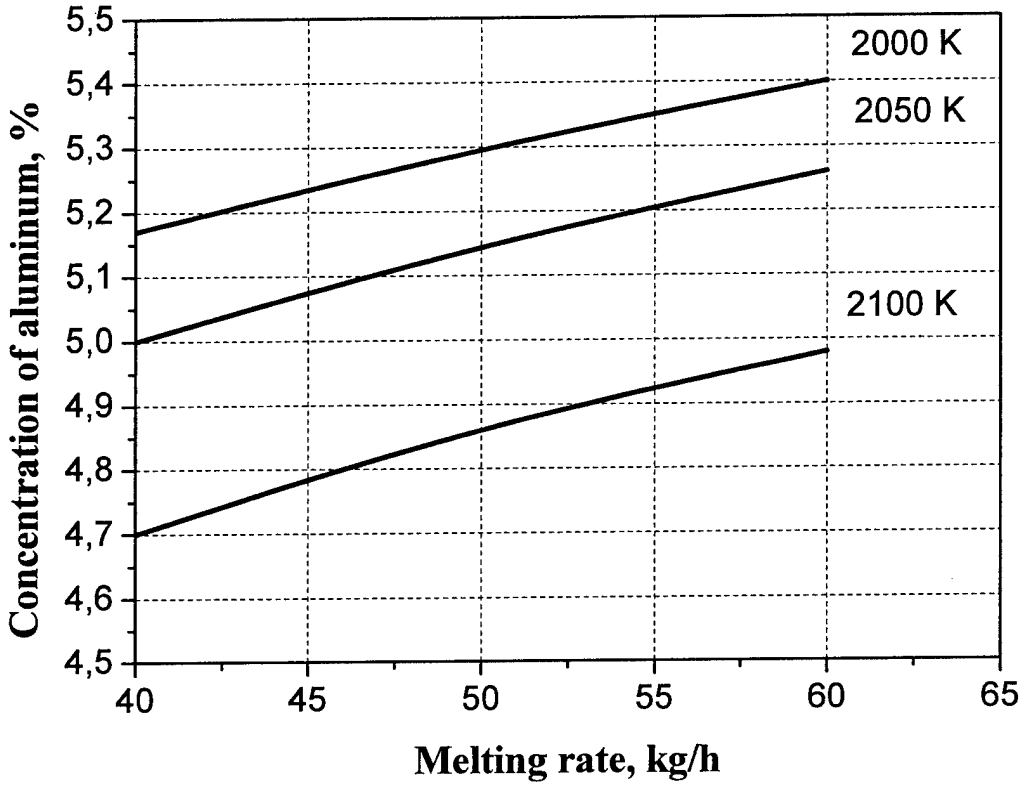

Figure 28. Model predictions of the aluminum concentration in alloy Ti-Al-Cr ingots after melting in the 0.3x0.4 m^2 cold hearth as a function of the melting rate at different temperatures and chromium content in the initial charge from 2 to 8 %. The aluminum content of initial charge is 6.3 %.

Main conclusion done from the above calculations was following: Cr losses are expected to be high and if "normal" temperature regime (~2100 K normally used for Ti-6Al-4V) were used for Ti17 the losses would exceed 50%. Therefore, melting regime with lower EB capacity was recommended to keep the temperature close to 2000 K. It was especially important since because of a danger of cracking during solidification the melting rate was chosen low, 40 kg/h, i.e. that with the highest predicted losses.

Experimental results: Ti-17

Tables 3 – 4

Specification:

4.5 – 5.5% (wt.) Al, 3.5 – 4.5% Mo, 3.5 – 4.5% Cr, 1.6 – 2.4% Sn, 1.6 – 2.4% Zr, Ti – balance

Raw materials: titanium sponge 79.2%, metallic molybdenum 4.0%, zirconium 2.0%, chromium 6.5%, tin 2.0% and aluminum 6.3%.

Horizontal feeding of raw material into melting zone.

Copper water-cooled cold hearth with dimensions 300×400 mm and copper water-cooled round mold with inner diameter of 150 mm.

Power of electron beam heating for charge melting 106 kW.

Power of EB-heating of melt in the mold 20 kW.

Melting rate 43 kg/h.

Estimated temperature 2006 K

Table 3

Chemical composition through melted Ti-17 ingot

Place of sampling	Element content, wt. %									
	Al	*Mo*	*Cr*	*Sn*	*Zr*	*Fe*	*C*	*O*	*H*	*N*
Top	5,10	3,68	3,50	1,87	2,38	0,10	0,023	0,12	0,002	0,010
Middle	4,95	4,41	3,60	1,63	2,16	0,10	0,015			
Bottom	5,30	4,26	3,75	2,40	1,61	0,14	0,024			

Table 4

Chemical composition through cross section of Ti-17 ingot

Place of sampling	Chemical composition, %									
	Al	*Mo*	*Cr*	*Sn*	*Zr*	*Fe*	*C*	*O*	*H*	*N*
Edge	5,31	4,09	3,78	2,42	1,83	0,15	0,027	0,12	0,002	0,010
2/3R	5,27	4,10	4,02	2,39	1,90	0,16	0,025			
1/3R	5,25	4,12	3,80	2,40	1,75	0,14	0,029			
Centre	5,23	4,11	3,87	2,41	1,83	0,16	0,025			
1/3R	5,24	4,12	3,85	2,48	1,68	0,17	0,029			
2/3R	5,20	4,13	3,86	2,40	1,94	0,15	0,031			
Edge	5,21	4,14	3,82	2,41	1,77	0,15	0,028	0,11	0,001	0,011

These data showed that chemical composition of melted Ti-17 ingot was well within the specification (Cr: 3.6-4.02 wt.%, Al: 5.15-5.31 wt.%), and that uniform distribution of alloying elements was observed through the ingot length and cross section.

Experimental results were compared with calculations. Content of Cr and Al are in a good agreement to those predicted for the 2050 K case and some higher than expected at 2000 K. The reason of the last discrepancy may be related either to the accuracy of temperature evaluation or to additional losses from the surface of consumable workpiece and water-cold mold.

Experimental results: VT22

Tables 5

Specification:

4.4 – 5.9% (wt.) Al, 4.0 – 5.5% Mo, 4.0 – 5.5% V, 0.5 – 1.5% Fe, 0.5 – 2.0 % Cr, Ti – balance

Table 5. Comparison of Predicted and Measured Aluminum and Chromium Content in titanium alloy VT22 ingots with diameter 150 mm after EBCHM

M_0 (kg/h)	W_e (kW)	W_c (kW)	Aluminum concentration, % (wt.)				Chromium concentration, % (wt.)			
			Initial	After EBCH	Predi-ction*	Devi-ation	Initial	After EBCH	Predi-ction*	Devi-ation
70.0	132	30	7.04	5.59	5.43	-0.16	1.98	0.61	0.57	-0.04
62.0	128	20	7.02	5.34	5.27	-0.07	2.02	0.56	0.58	0.02
66.0	128	16	7.03	5.34	5.40	0.06	2.08	0.72	0.68	-0.04
59.0	128	16	7.00	4.92	5.19	0.27	2.09	0.52	0.59	0.07

* by Paton Institute modeling (see Figures 29 - 32)

Experimental results on VT22 could not be compared with thermodynamic predictions because of uncertainty with temperature of melt.

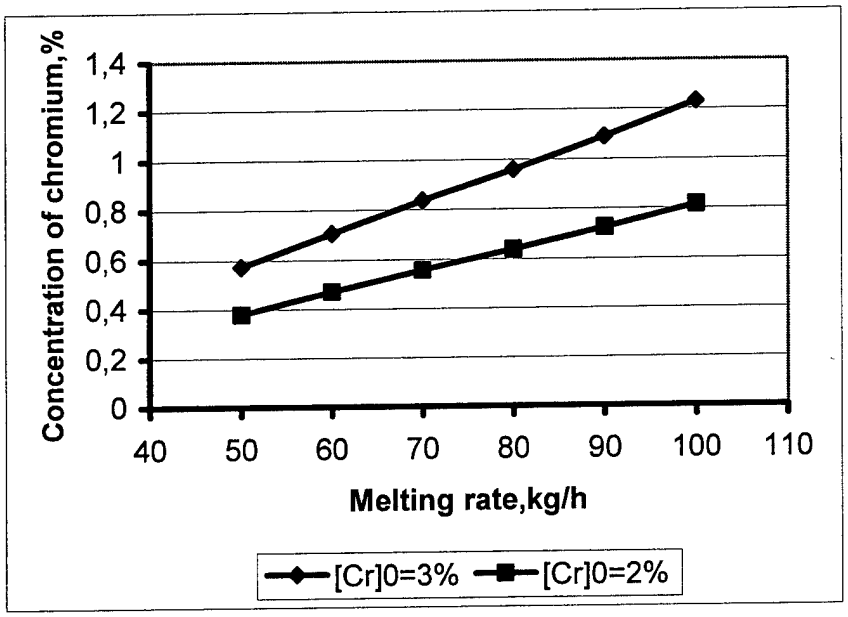

Figure 29. Expected chromium concentration in ∅150 mm *Ti-6Al-2Cr* ingot as a function of the melting rate m_0 at different initial chromium content. Initial aluminum content 7%, power input to the hearth W_e = 150 kW, power input to the mold W_c = 20 kW.

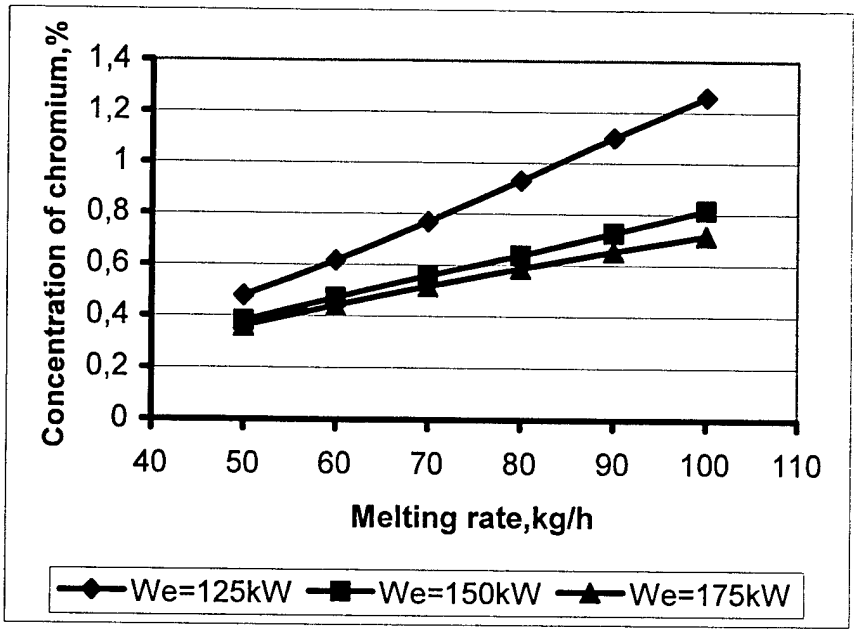

Figure 30. Expected chromium concentration in ∅150 mm *Ti-6Al-2Cr* ingot as a function of the melting rate m_0 at different power input to cold hearth W_e. Initial aluminum content 7%, initial chromium content 2%, power input to the mold W_c = 20 kW.

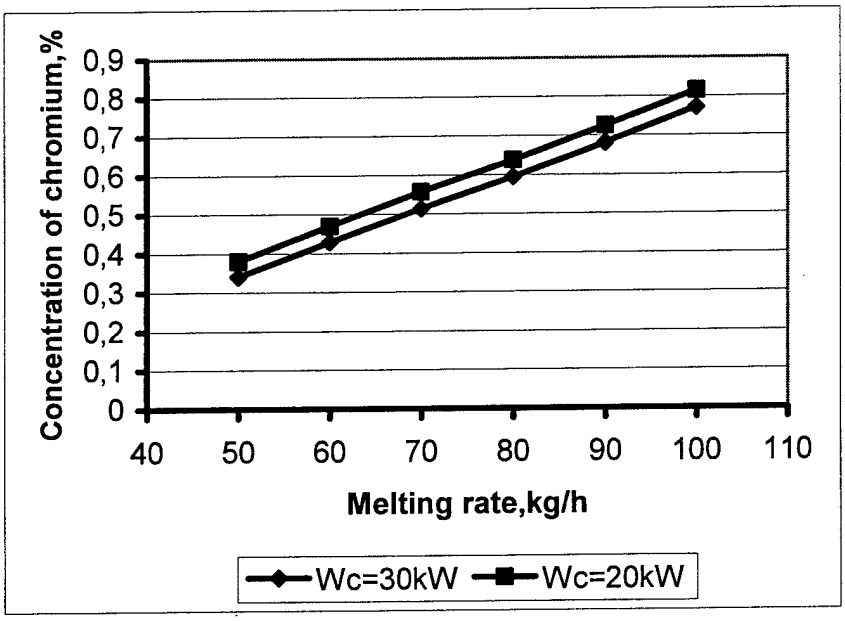

Figure 31. Expected chromium concentration in ∅150 mm *Ti-6Al-2Cr* ingot as a function of the melting rate m_0 at different power input to the mold W_c. Initial aluminum content 7%, initial chromium content 2%, power input to the cold hearth W_e = 150 kW.

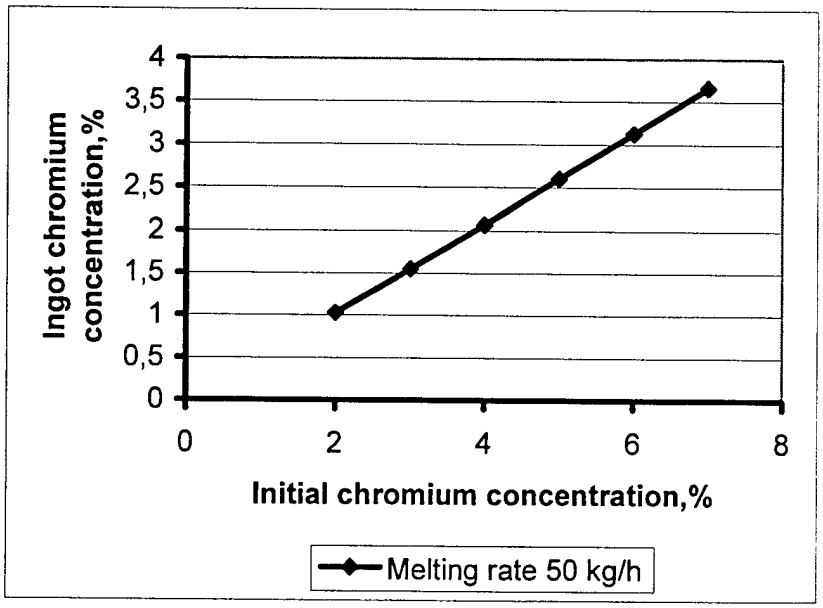

Figure 32. Expected chromium concentration in ∅150 mm *Ti-6Al-2Cr* ingot as a function of the initial chromium content. Melting rate 50 kg/h, initial aluminum content 7%, power input to the cold hearth W_e = 100 kW, power input to the mold W_c = 20 kW.

Thermo-physical model of slab solidification

Figures 33 - 38

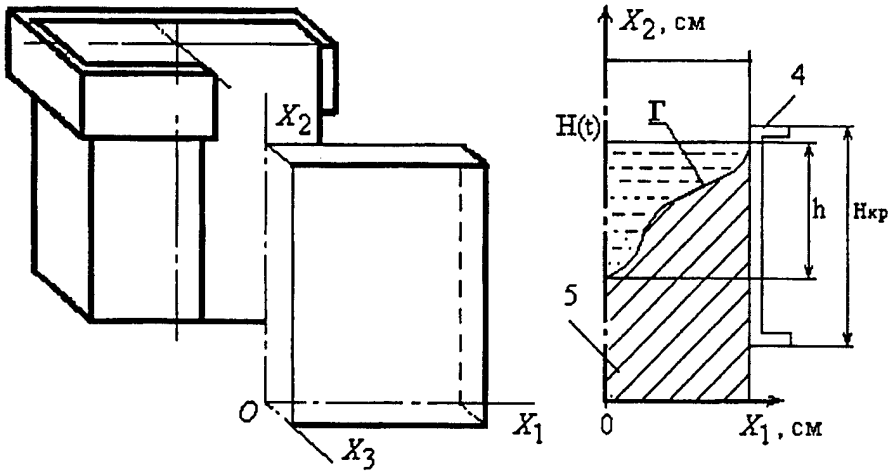

Figure 33. Schematic presentation of modeled zone.
H(t) – ingot height
Г – solidification front
$H_{кр}$ – mold height.

The mathematical model is based on the solution of the three-dimensional Fourier's heat transfer equation in the field of an ingot in rectangular system of coordinates, which origin is located in the center of the ingot basis, and axes are parallel to sides of an ingot.

$$\frac{\partial W}{\partial t} = \sum_{\alpha=1}^{p} \frac{\partial}{\partial x_\alpha} \left(\lambda_{effective}(\mathrm{T}) \frac{\partial T}{\partial x_\alpha} \right);$$

$$\Omega = \{ 0 < x_\alpha < X_\alpha,\ \alpha = \overline{1,p},\ p = 3 \},\ t \in [0, t^*].$$

Equation is valid for positive coordinates. Boundary conditions for the specified area were formulated as the following.

On planes of symmetry the thermal flow is absent, i.e. the derivative of temperature on the appropriate coordinates is equal to zero.

$$\left.\frac{\partial T}{\partial \mathrm{x}_1}\right|_{x_1=0} = \left.\frac{\partial T}{\partial \mathrm{x}_3}\right|_{x_3=0} = 0.$$

On a lateral and bottom surface of an ingot heat exchange with mold (and, accordingly - the pallet) is carried out under the law of contact Newton – Richman's heat exchange if the ingot densely adjoins to a wall of mold (a formal condition - the temperature at a surface of an ingot above some critical temperature "shrinkage beginning" $T=T_k$),

$$T \geq T_k$$

$$-\lambda(T)\frac{\partial T}{\partial x} = \vartheta(T - T_{mold})$$

where υ- factor of a heat transfer, and under the law of radiant Stefan-Bolzman's heat exchange (temperature below critical)

$$T < T_k$$

$$\lambda(T)\frac{\partial T}{\partial x} = -\varepsilon\sigma(T^4 - T_{env}{}^4).$$

At the top surface of an ingot

$$\lambda(T)\frac{\partial T}{\partial x_2}\Big|_{x_2=H(t)} = -\varepsilon\sigma(T^4 - T_{env}{}^4) + w(r,t),$$

where $w(r,t)$ is heating by two EB – central and peripheral W_1 and W_2

At transition of metal from liquid into solid condition allocation of the latent heat of crystallization occurs in regular manner in an interval of crystallization (solidus-liquidus).

Convective heat transfer in a liquid phase was taken into account as multiplication conductive heat transfer on some correction factor.

The modeling was done with the method of finite differences under the implicit scheme.

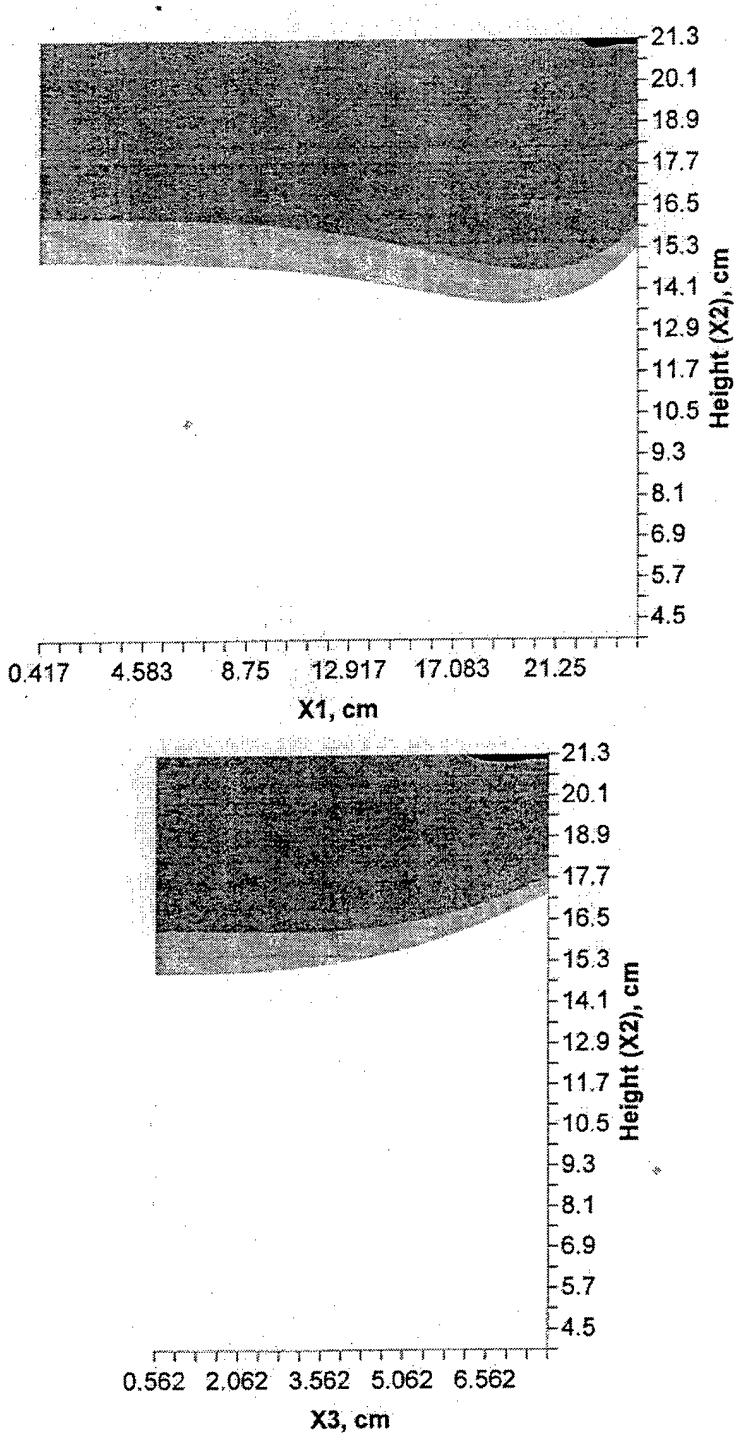

Figure 34. Two cross-section temperature fields (black – overheating 50K, gray – liquid pool, light gray – mushy zone).

Power distribution according to that used in trials was simulated.

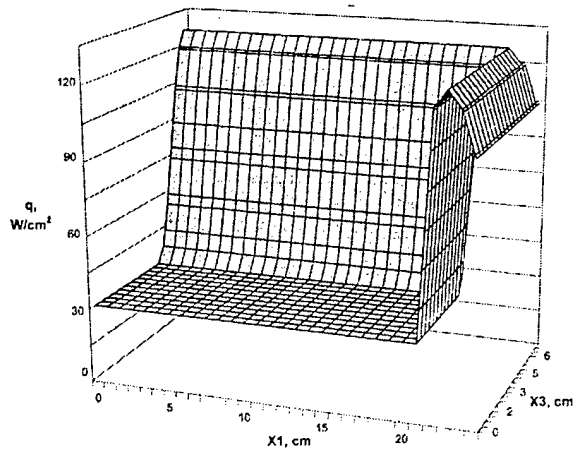

Regime # 1

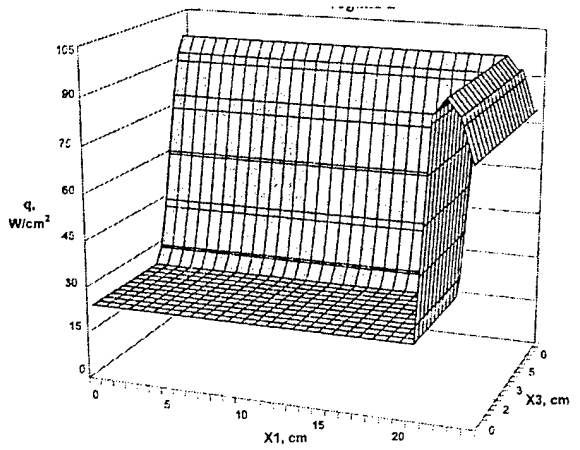

Regime #2

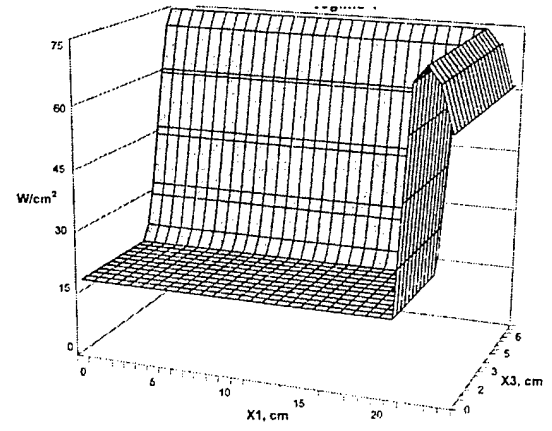

Regime # 3

Figure 35. 3D distribution of EB power through the mold (1/4 part). Regimes 1, 2 and 3 correspond respectively to total power of 30, 40 and 50 kW applied to the ingot surface.

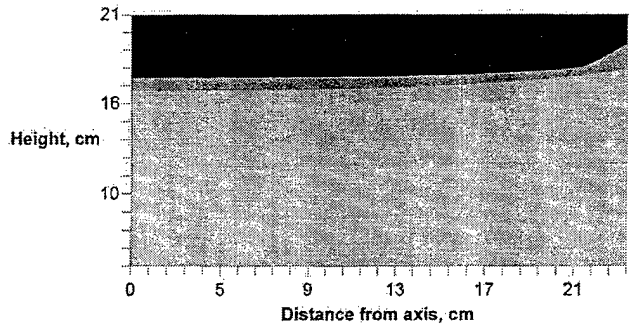

Regime # 1

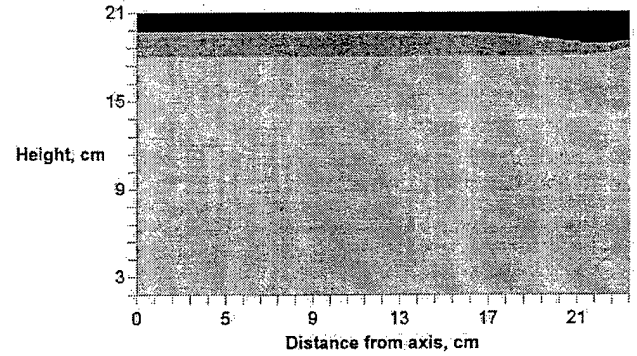

Regime # 2

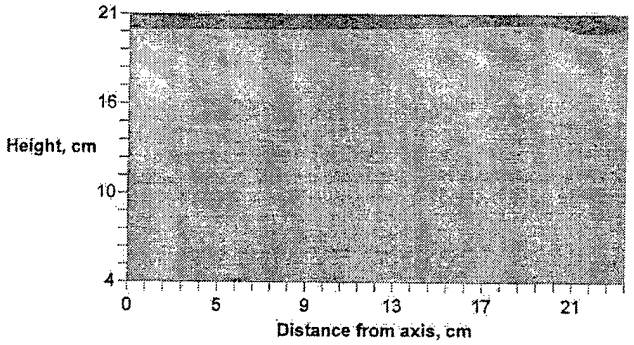

Regime # 3

Figure 36. Distribution of aggregative states through ½ part of the slab (longitudinal section). Black color- melt, dark gray – semi-liquid (mushy) zone, light gray - solid metal.

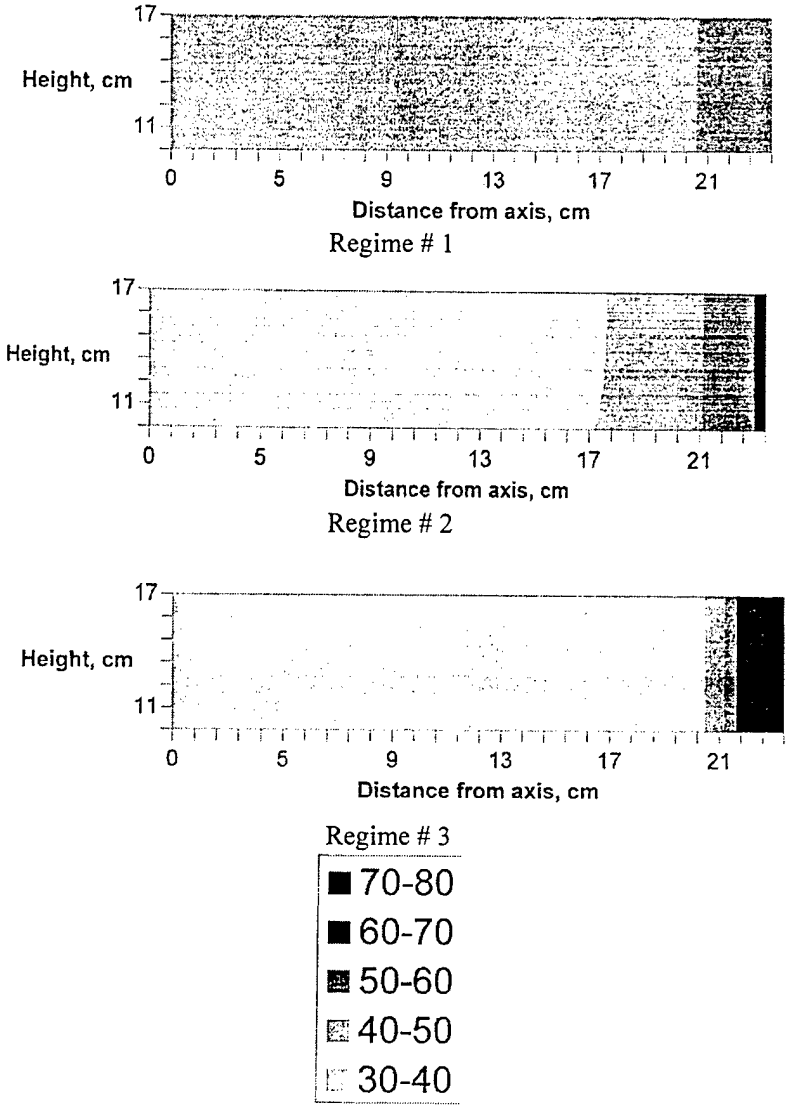

Figure 37. Temperature gradients (K/cm^2) for ½ part of slab.

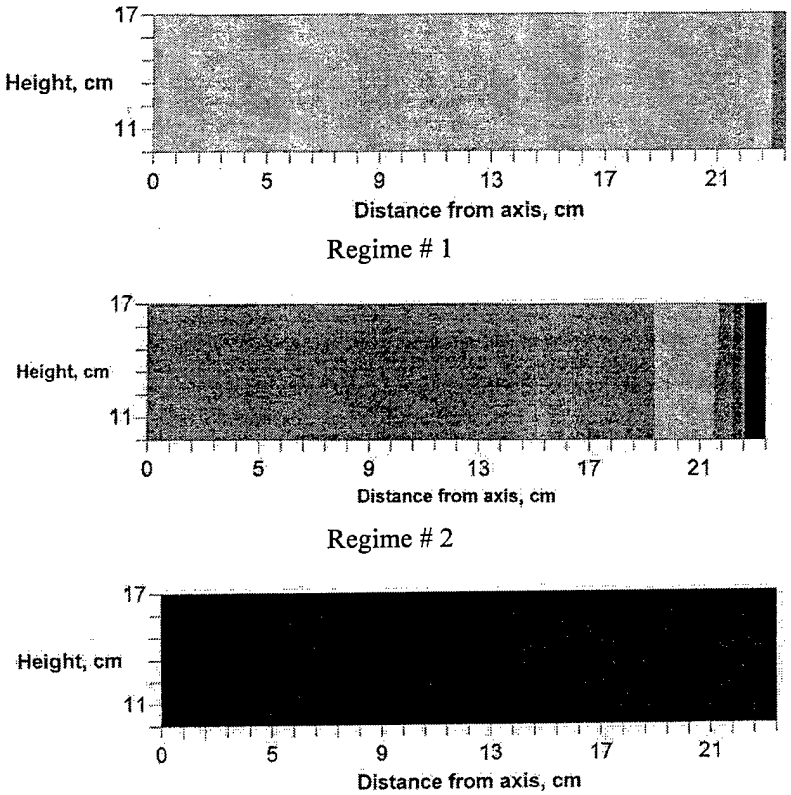

Figure 38. Cooling rates (Ks^{-1}) distribution through ½ part of slab.

Following conclusions were made from modeling:

1. Three-dimensional thermo-physical model allows to calculate temperature fields, gradients and cooling rates for EBCHM slab of Ti-6Al-4V.
2. It was shown that for a real EBCHM parameters, temperature gradient variation was monotonic while moving from the center to the rim normally to ingot vertical axis.
3. It was shown that at heating regime #2, cooling rate had some minimum at slab periphery. It was suggested that location of this minimum could correspond to zone of columnar microstructure. Comparison of experimental and calculated results does not contradict this suggestion.
4. 3D thermo-physical modeling can be used for ingot structure prediction.

Part 2

Activity # 9: *To study microstructure / properties relationships in fine-grained beta alloys processed with using deformation - rapid heating approach.*

9.1. Investigation of microstructure/ mechanical properties relationship for beta-titanium alloys processed by cold deformation, rapid heating and aging.

9.2. Investigation of microstructure/ mechanical properties relationship for beta-titanium alloys processed by warm deformation, rapid heating and aging.

Comparative study of three programme alloys:
TIMETAL-LCB, Ti-15-3 and VT22.

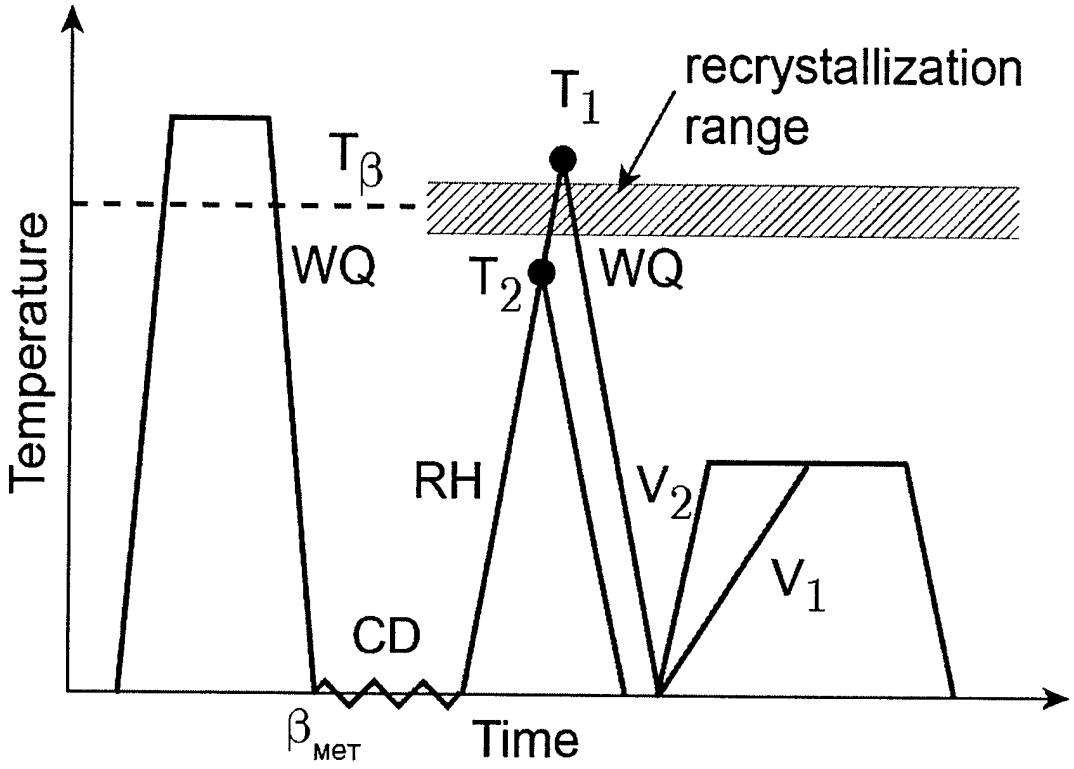

Figure 39. Scheme of treatments.

Definitions of terms:
RR – rapid recrystallization;
RP – rapid polygonization;
CD – cold deformation;
WQ – water quenching;
RH – rapid heating;
V_1, V_2 – heating rates to aging peak temperature;
T1 – temperature of recrystallization;
T2 – temperature of polygonization;
ST – solid solutioning treatment.

TIMETAL-LCB

Figures 40 - 63
Tables 6 - 8

Table 6
Mechanical Properties of TIMETAL-LCB

##	Treatment				Properties			
	Condition	Rapid Heating	Aging	Heating rate	YS, MPa	UTS, MPa	El., %	RA, %
1	*RR*	*20 Ks^{-1} 815 °C*	*520°C, 8h*	*0.16 Ks^{-1}*	*1600*	*1640*	*9.4*	*36.5*
2	*RR*	*20 Ks^{-1} 815°C*	*520°C, 8h*	*20 Ks^{-1}*	*1445*	*1510*	*7.0*	*28*
3	**RP**	**20 Ks^{-1} 780 °C**	**520°C, 8h**	**0.16 Ks^{-1}**	**1685**	**1685**	**5.4**	**27.5**
4	**RP**	**20 Ks^{-1} 780°C**	**520°C, 8h**	**20 Ks^{-1}**	**1580**	**1600**	**6.7**	**31**
5	*RR*	*20 Ks^{-1} 815 °C*	*538°C, 8h*	*0.16 Ks^{-1}*	*1470*	*1510*	*9,9*	*43*
6	*RR*	*20 Ks^{-1} 815°C*	*538°C, 8h*	*20 Ks^{-1}*	*1340*	*1405*	*10,5*	*42*
7	**RP**	**20 Ks^{-1} 780 °C**	**538°C, 8h**	**0.16 Ks^{-1}**	**1580**	**1580**	**2,6**	**25**
8	**RP**	**20 Ks^{-1} 780°C**	**538°C, 8h**	**20 Ks^{-1}**	**1590**	**1590**	**5,1**	**32**
9	*RR*	*20 Ks^{-1} 815 °C*	*560°C, 8h*	*0.16 Ks^{-1}*	*1435*	*1460*	*11.7*	*50.3*
10	*RR*	*20 Ks^{-1} 815°C*	*560°C, 8h*	*20 Ks^{-1}*	*1360*	*1400*	*12.3*	*60*
11	**RP**	**20 Ks^{-1} 780 °C**	**560°C, 8h**	**0.16 Ks^{-1}**	**1600**	**1600**	**4.6**	**35.5**
12	**RP**	**20 Ks^{-1} 780°C**	**560°C, 8h**	**20 Ks^{-1}**	**1605**	**1605**	**4.9**	**29**

Following conclusions can be drawn from above tensile data:

a) In general, recrystallized condition has shown better balance of tensile strength and ductility. The strength varied from 1640 MPa to 1400 MPa with change of aging temperature from 520 to 560°C.

b) Significant role of rate of heating to aging temperature in balancing mechanical properties was established. Slow heating (0.16 Ks^{-1}), at which precipitation in beta-phase proceeded through the formation of isothermal omega-phase, allowed higher both strength and ductility after aging at 520°C to be obtained in comparison with heating 20 Ks^{-1}. Advantage in strength remained valid for higher aging temperatures also, while difference in ductility decreased with increase of aging temperature.

c) Polygonized microstructure showed completely different aging response. Conditions achieved by fast heating to aging temperature showed weak dependence of strength and ductility on aging temperature. For slow heated conditions the ductility remained low even when strength went down due to high aging temperature.

Thus, the best combination of tensile properties for TIMETAL-LCB was obtained in fine grained recrystallized condition slowly heated to aging temperature 520°C, 8h.

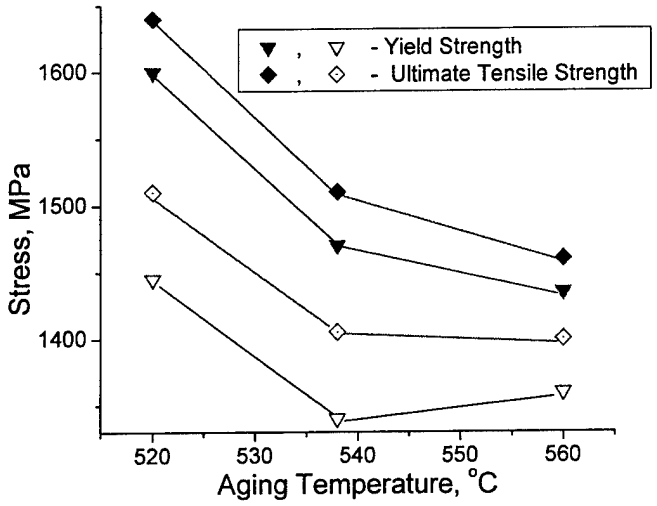

a

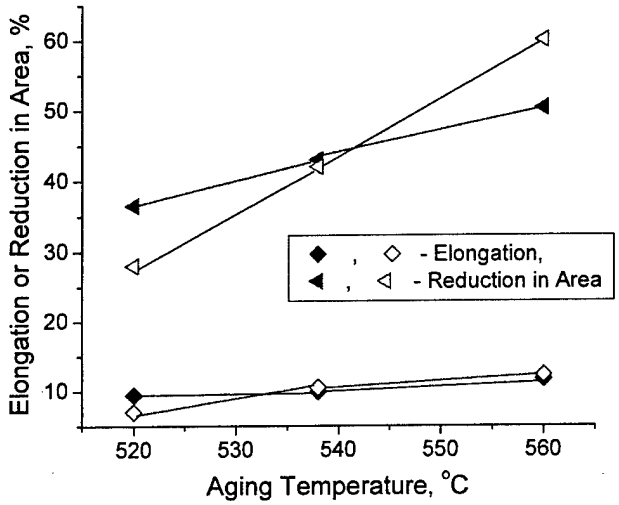

b

Figure 40. Influence of aging temperature on (a) tensile strength and (b) ductility of TIMETAL-LCB in RR condition aged 8h. Rate of heating to aging temperature: (open symbols) - 20 Ks^{-1}, (solid symbols) – 0.16 Ks^{-1}.

Precipitation mechanism: TEM

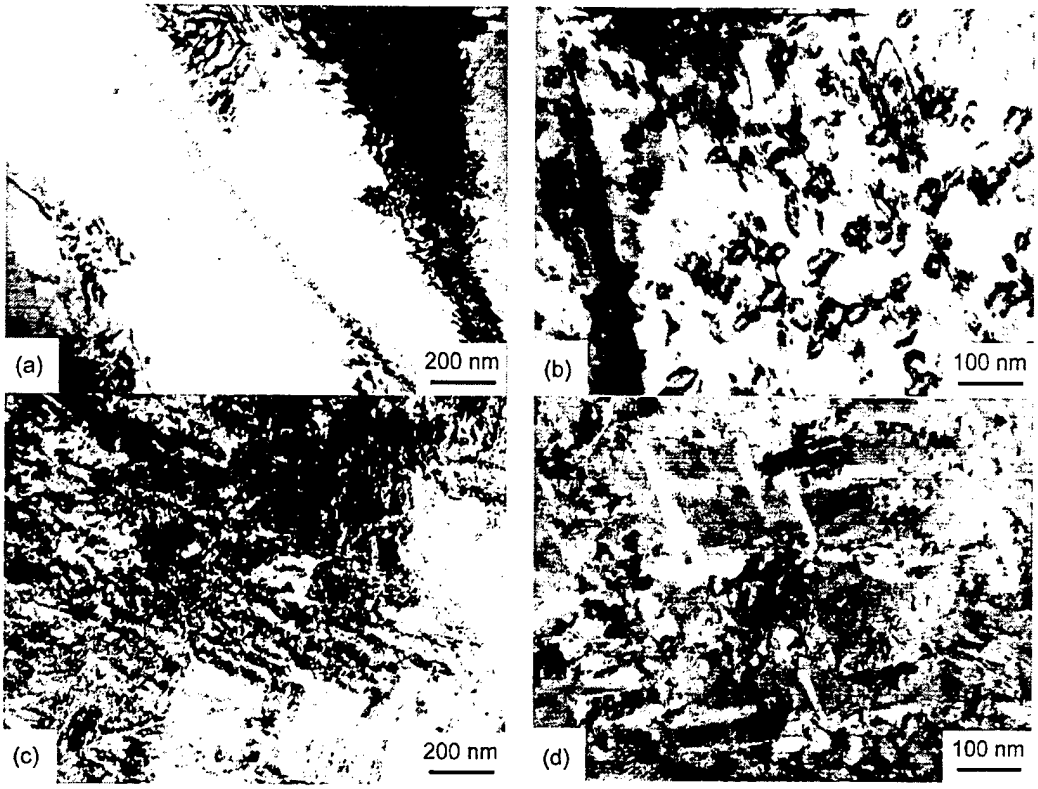

Figure 41. Microstructure of TIMETAL-LCB in: (a) quenched condition and after aging at 538°C during (b) 1 min, (c) 5 min and (d) 15 min.

Precipitation sequence: $\beta \rightarrow \beta+\omega \rightarrow \beta+\alpha_{glob} \rightarrow \beta+\alpha'' \rightarrow \beta+\alpha$

Table 7

Beta-stabilizer content in alpha-precipitates developed during aging at 538°C

Aging Exposure (h)	Content of Alloying Element (wt. pct.)	
	Mo	Fe
0.25	6.88	3.86
0.5	6.21	1.53
1	3.15	0.62
8	0.65	0.22

Iron redistributes between alpha and beta phases faster than molybdenum.

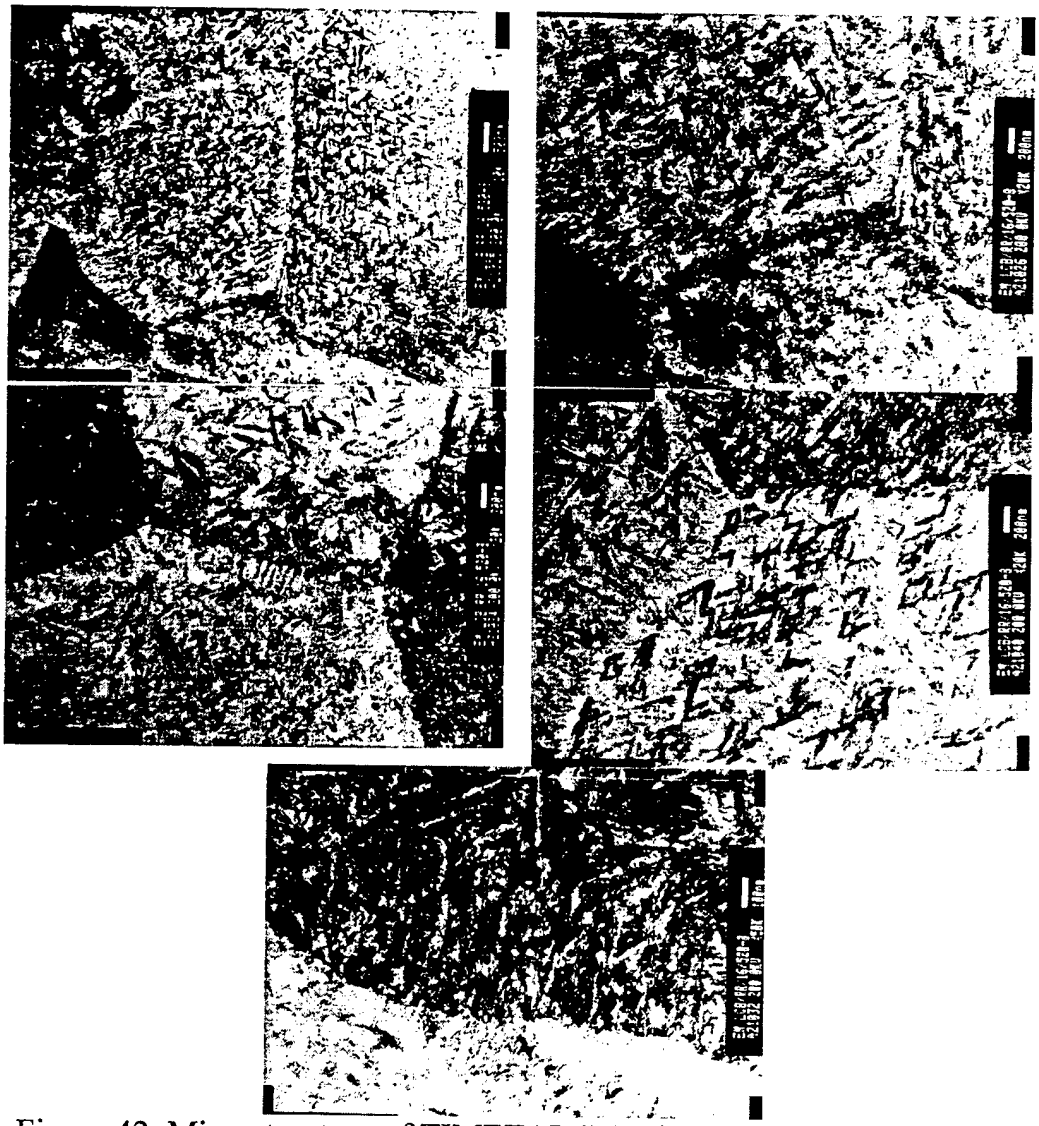

Figure 42. Microstructure of TIMETAL-LCB in RR condition #1 (table 6, aging at 520°C, 8h, heating rate to aging temperature - 0.16Ks^{-1}).

Main features:
-fine uniform beta precipitated microstructure.
-no precipitation free zones.
-no grain boundary alpha.

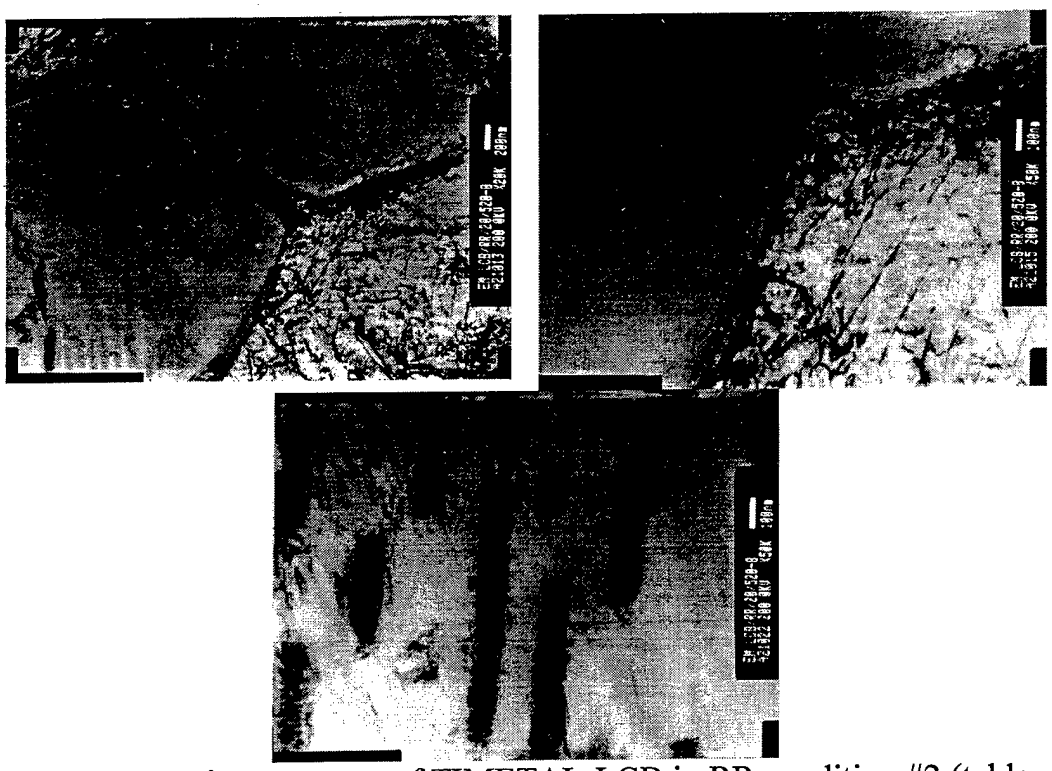

Figure 43. Microstructure of TIMETAL-LCB in RR condition #2 (table 6, aging at 520°C, 8h, heating rate to aging temperature - 20Ks^{-1}).

Main features:

- nonuniform precipitation behavior, separate grains free from precipitation
- coarse alpha precipitations.

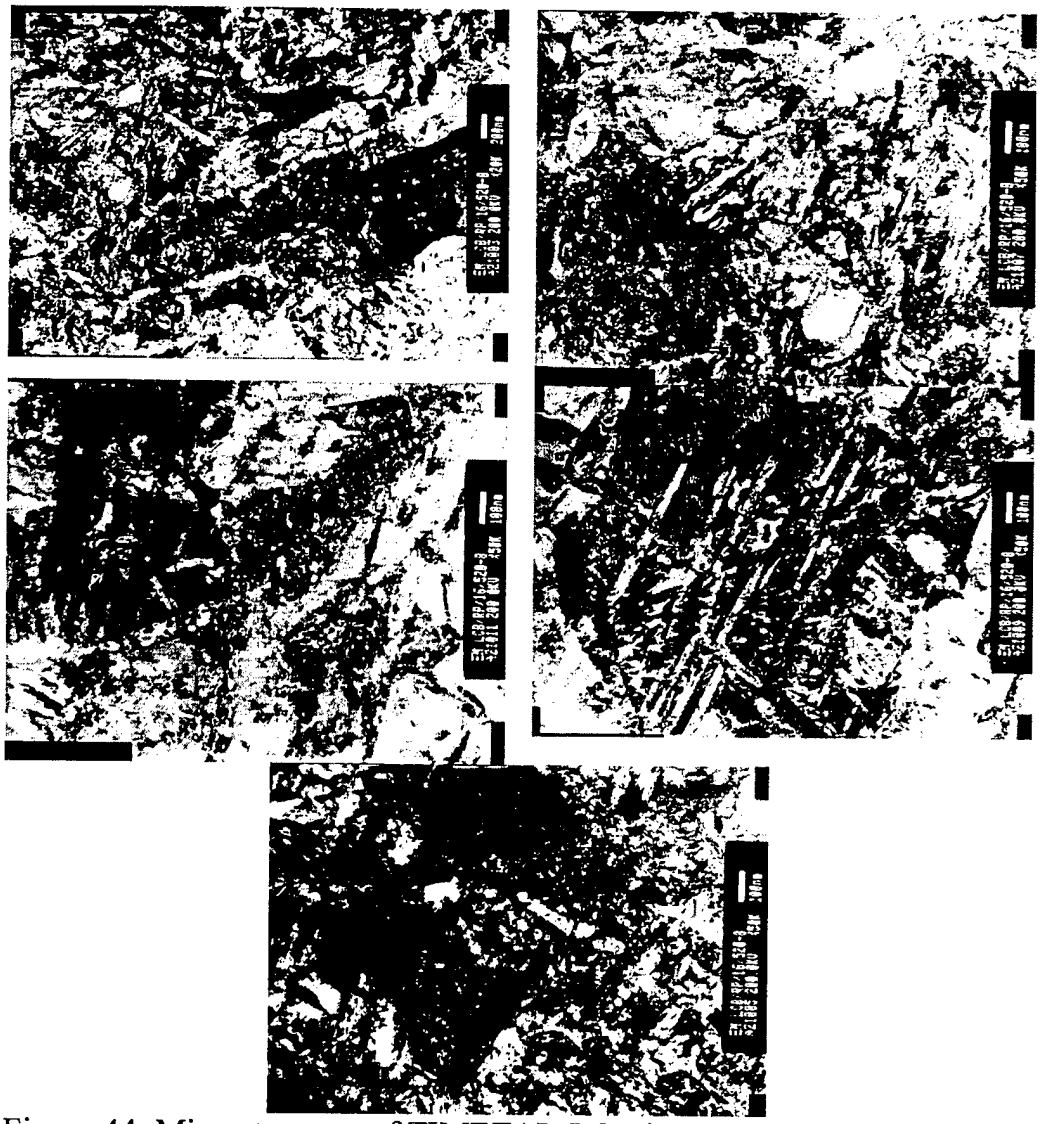

Figure 44. Microstructure of TIMETAL-LCB in RP condition #3 (table 6, aging at 520°C, 8h, heating rate to aging temperature - 0.16Ks^{-1}).

Main features:

- nonuniform precipitation structure influenced by residual deformation defects,
- elongated grains, grain boundaries not seen on TEM pictures.

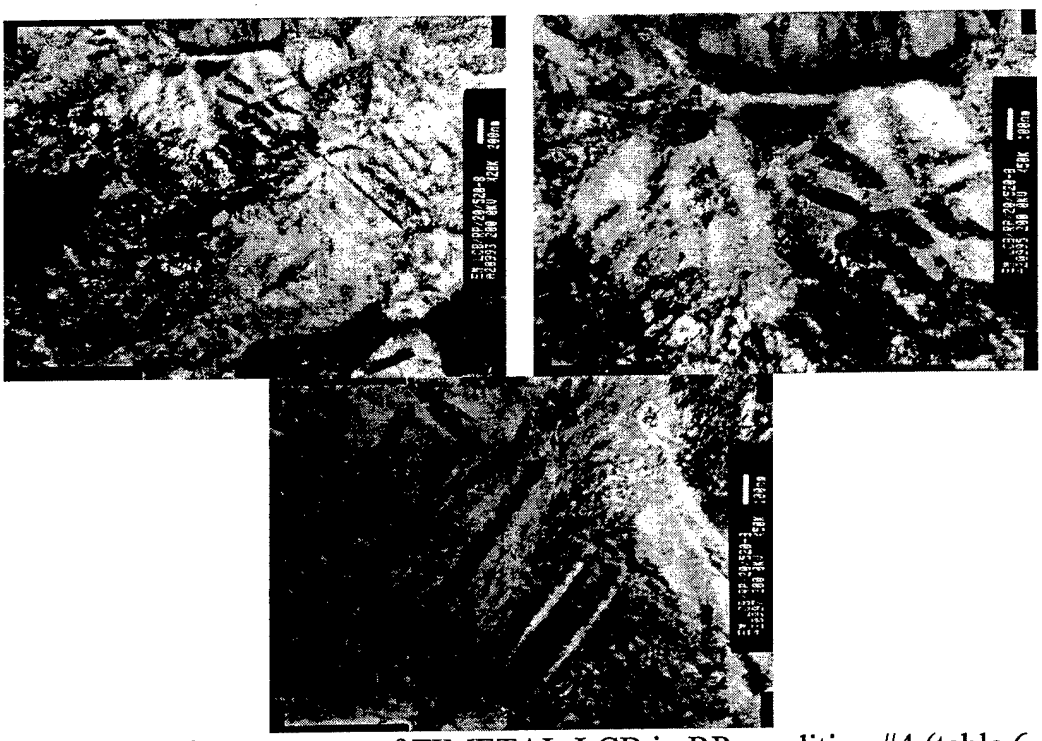

Figure 45. Microstructure of TIMETAL-LCB in RP condition #4 (table 6, aging at 520°C, 8h, heating rate to aging temperature - $20Ks^{-1}$).

Microstructure is slightly coarser than in previous picture but heating rate to aging temperature is not so important for RP condition as compared to RR condition.

Precipitation mechanism: X-ray orientation analysis

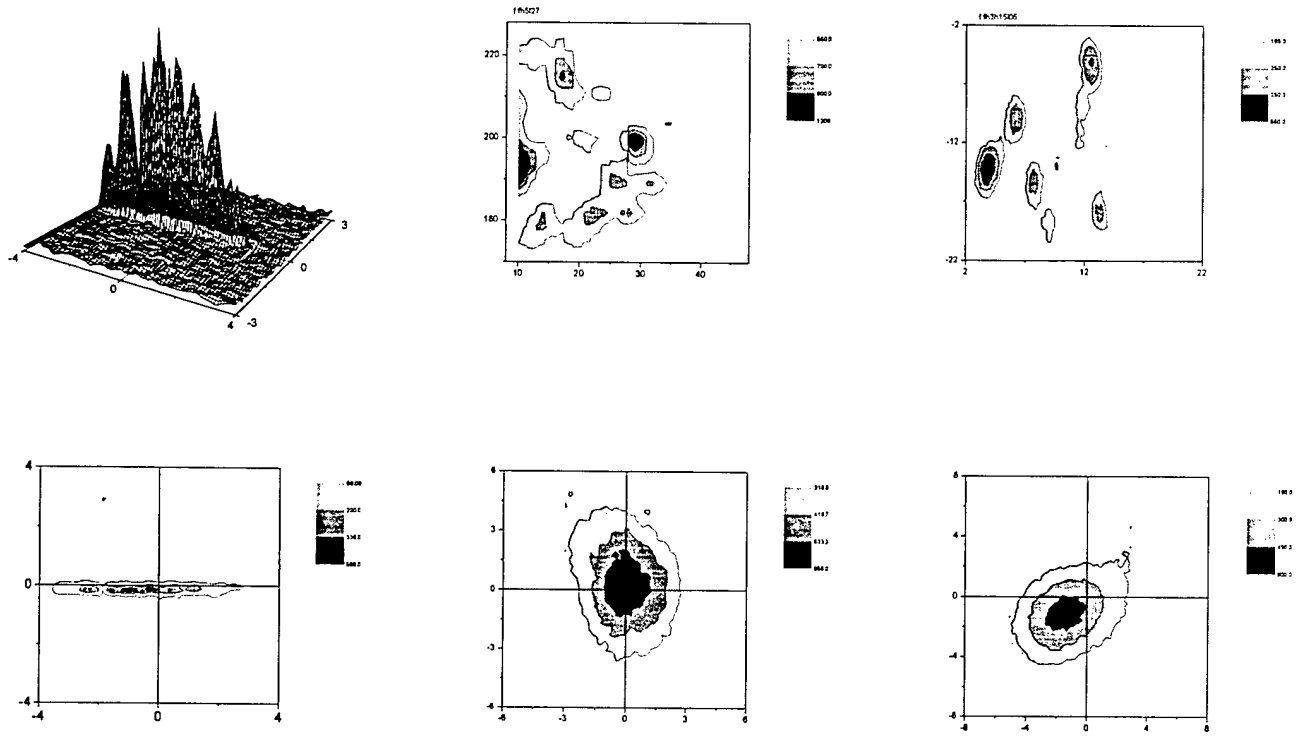

a b c

Figure 46. Comparison of evolution of {110}β intensity distributions $\mathbf{I}q_{\perp}$ for (a) solid solutioned and aged at 538 °C for (b) 5' and (c) 15' TIMETAL-LCB.

SEM of fracture surfaces

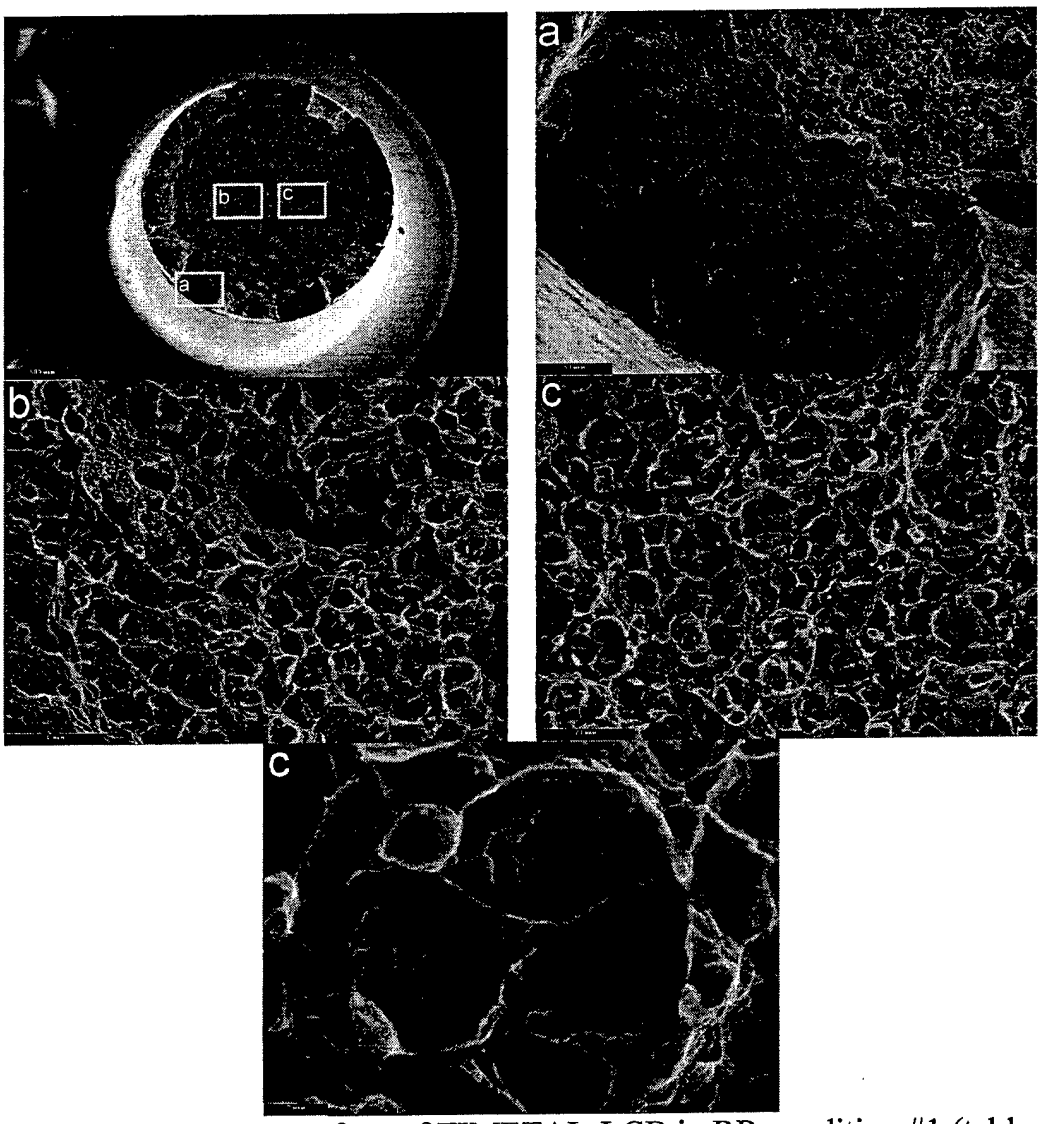

Figure 47. Fracture surface of TIMETAL-LCB in RR condition #1 (table 6, aging at 520°C, 8h, heating rate to aging temperature $0.16Ks^{-1}$).

The fracture surfaces have indications of both ductile and quasi-brittle (transcrystalline or intercrystalline cleavage) mechanisms. Areas of ductile fracture prevail. Fracture was initiated from the rim of the necked specimen.

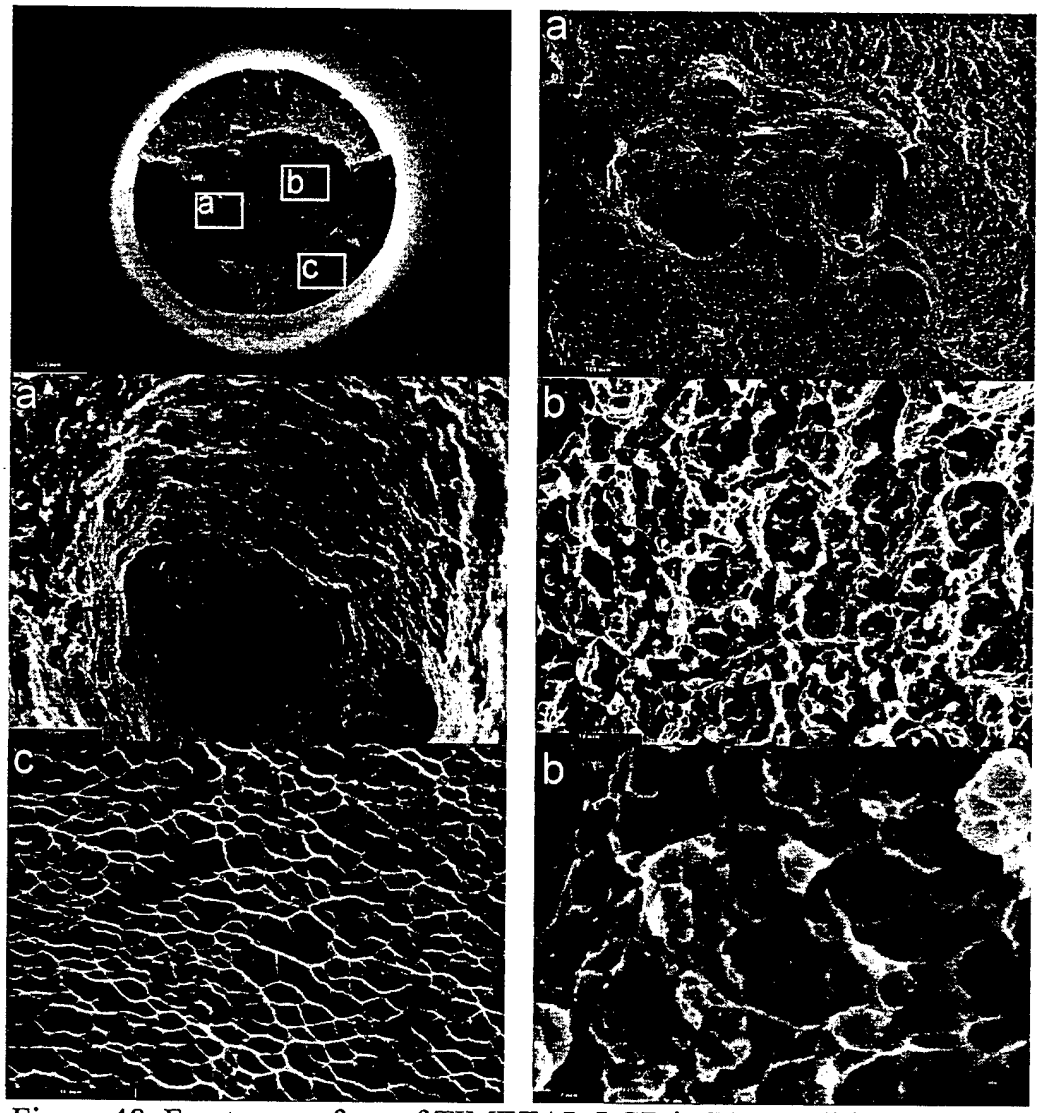

Figure 48. Fracture surface of TIMETAL-LCB in RR condition #2 (table 6, aging at 520°C, 8h, heating rate to aging temperature 20Ks^{-1}).

Fraction of ductile fracture is higher than in previous case. Fracture started in the sample interior, where pits resembling intercrystalline fracture are seen.

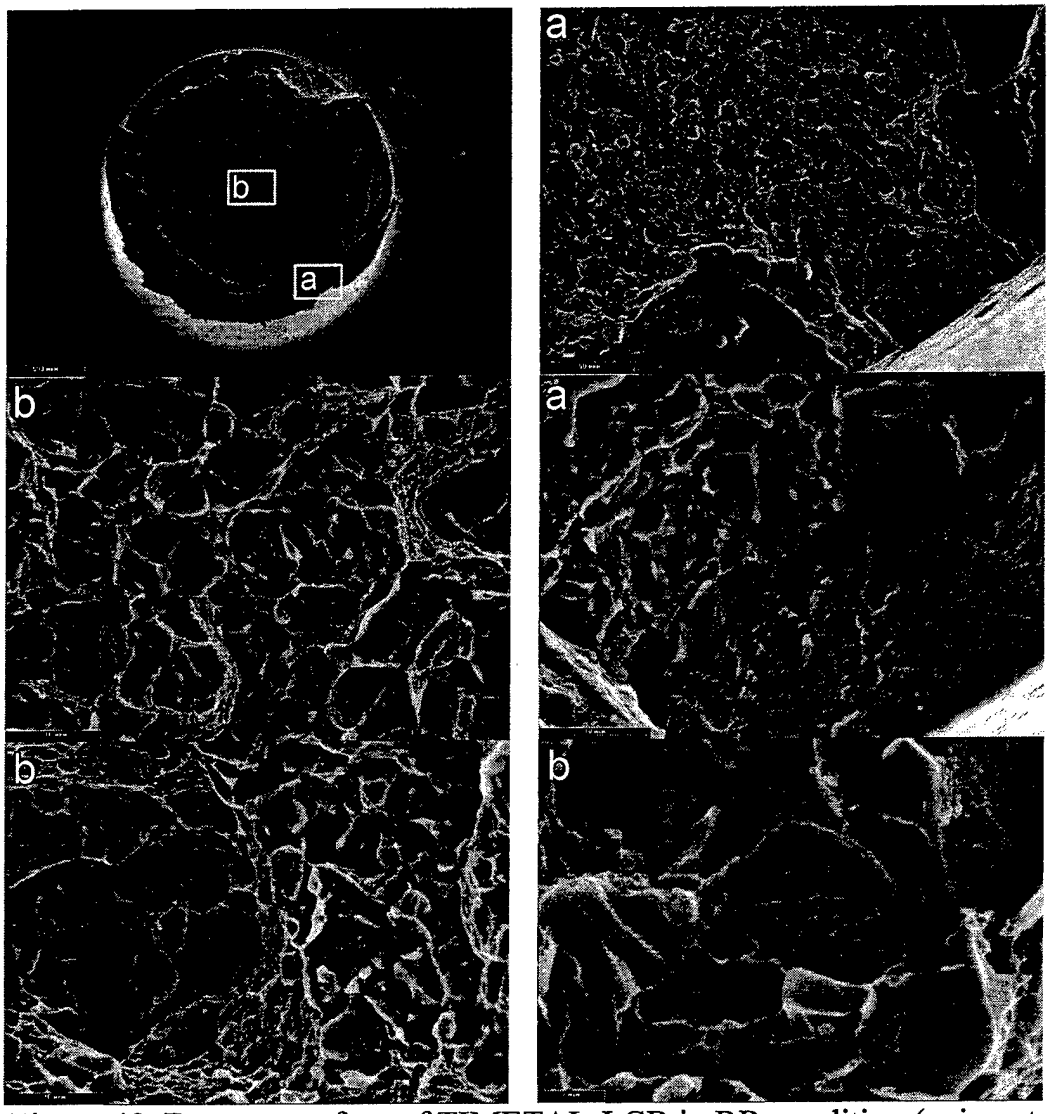

Figure 49. Fracture surface of TIMETAL-LCB in RR condition (aging at 538°C, 15min).

Fraction of quasi-brittle fracture is rather higher. Fracture was initiated from the rim of the necked specimen.

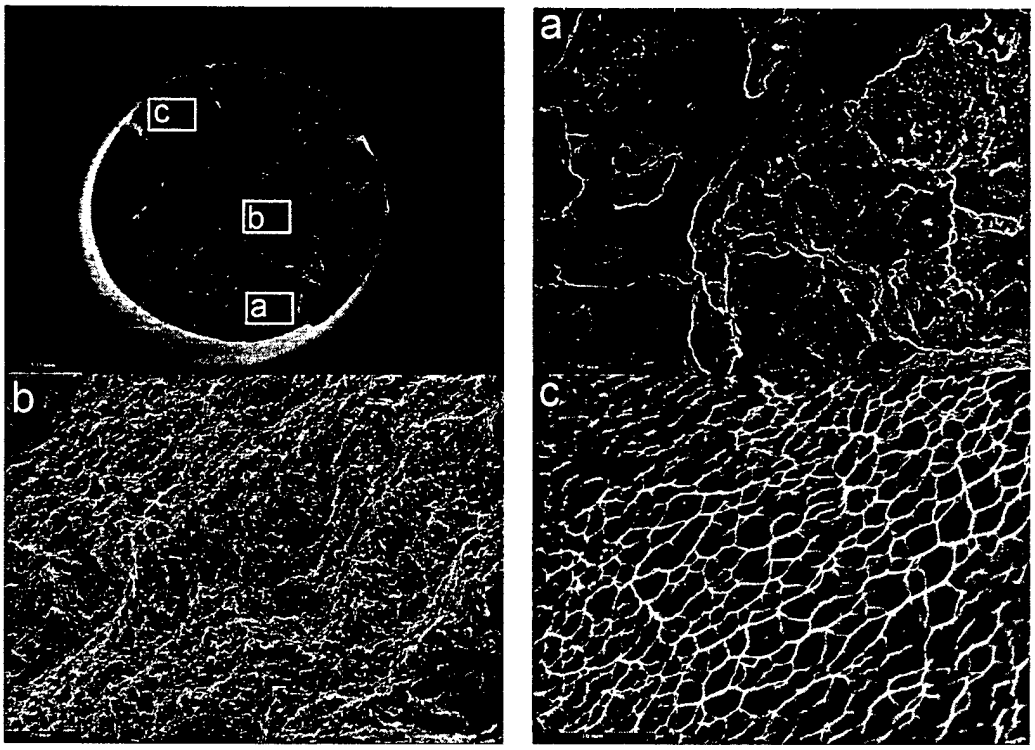

Figure 50. Fracture surface of TIMETAL-LCB in RP condition #3 (table 6, aging at 520°C, 8h, heating rate to aging temperature $0.16Ks^{-1}$).

The fracture is quasi-ductile. Fracture was initiated from the rim of the necked specimen.

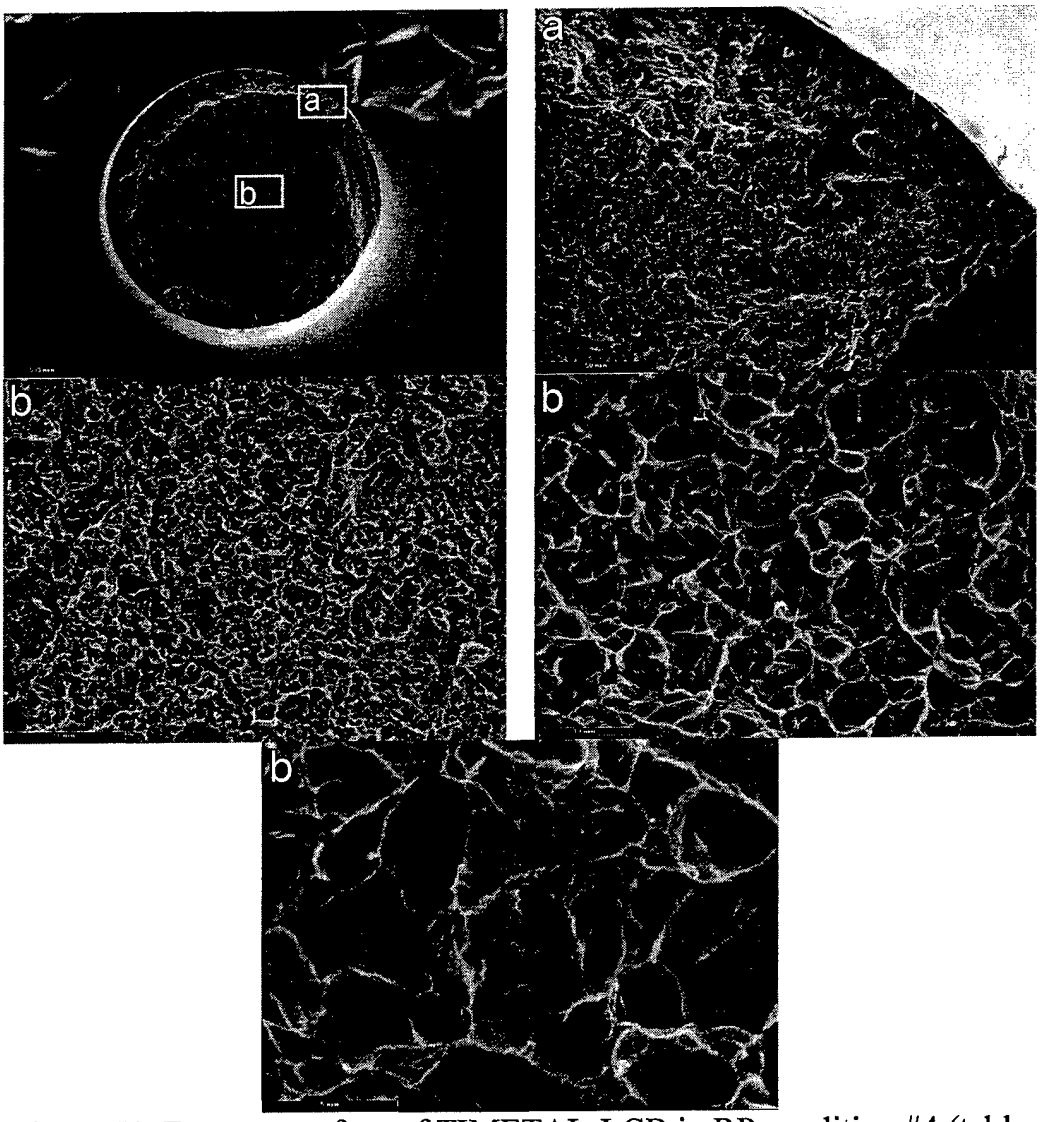

Figure 51. Fracture surface of TIMETAL-LCB in RP condition #4 (table 6, aging at 520°C, 8h, heating rate to aging temperature 20Ks^{-1}).

The fracture is quasi-ductile. The dimple size is possibly determined by subgrain size. Sometimes areas of quasi-brittle fracture between subgrains are observed. Fracture was initiated from the rim of the necked specimen.

Role of grain size

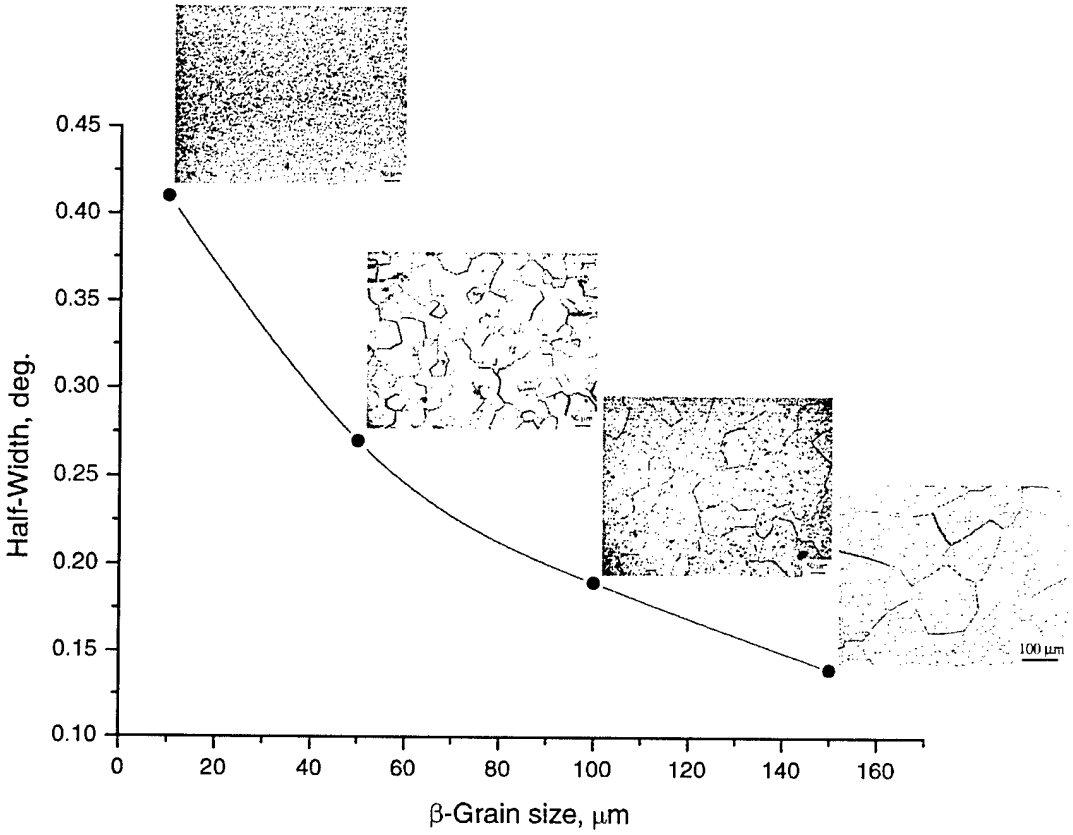

Figure 52. Influence of beta-grain size on the half-width of $(110)_\beta$ line for TIMETAL-LCB.

Texture evolution in CD TIMETAL-LCB on rapid heating

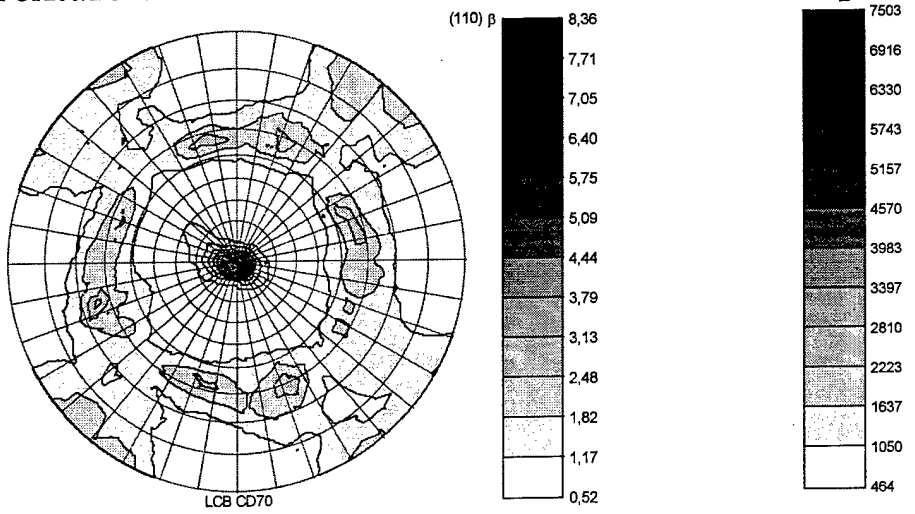

Figure 53. (110)β pole figure of CD TIMETAL-LCB.

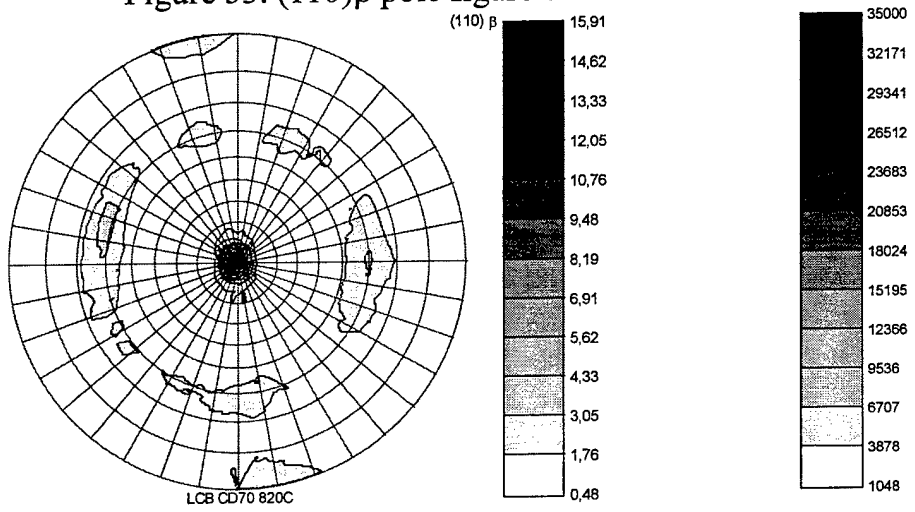

Figure 54. (110)β pole figure of CD and RR (beta-820°C) TIMETAL-LCB. Heating rate 20 Ks^{-1}.

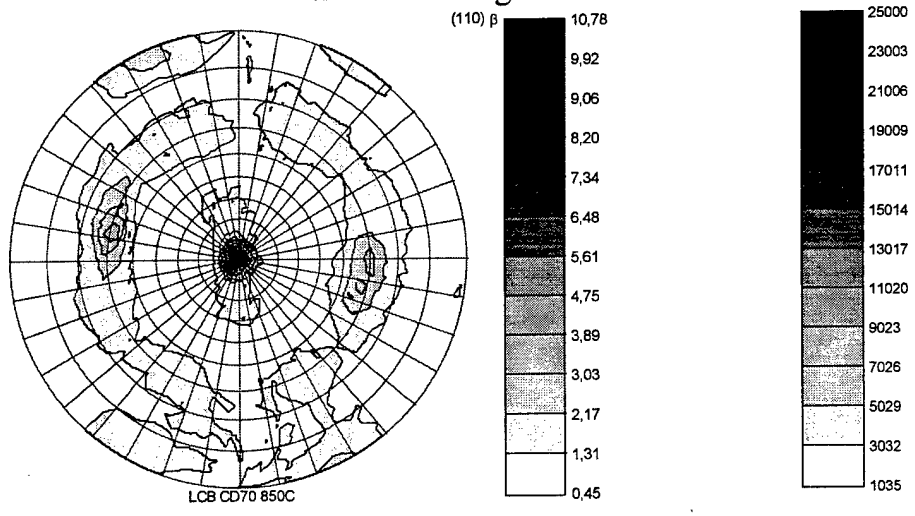

Figure 55. (110)β pole figure of CD and RR (beta-850°C) TIMETAL-LCB. Heating rate 20 Ks^{-1}.

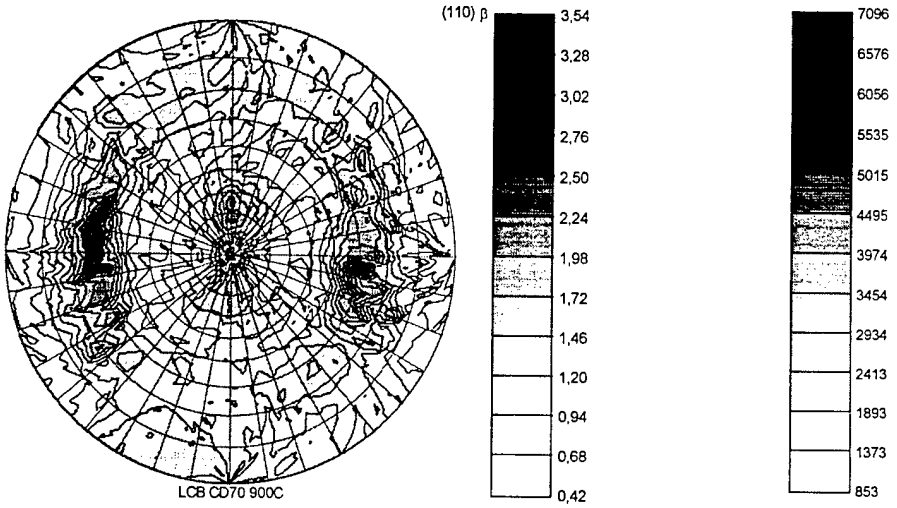

Figure 56. (110)β pole figure of CD and RR (beta-900°C) TIMETAL-LCB. Heating rate 20 Ks^{-1}.

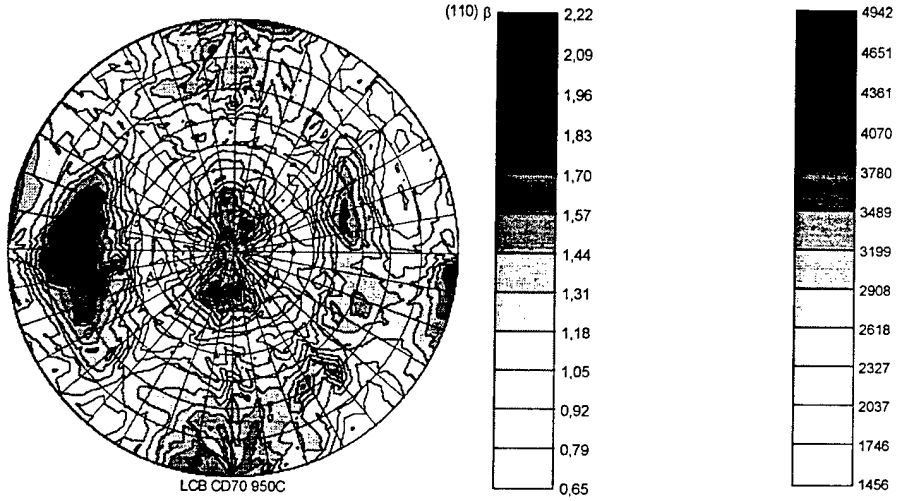

Figure 57. (110)β pole figure of CD and RR (beta-950°C) TIMETAL-LCB. Heating rate 20 Ks^{-1}.

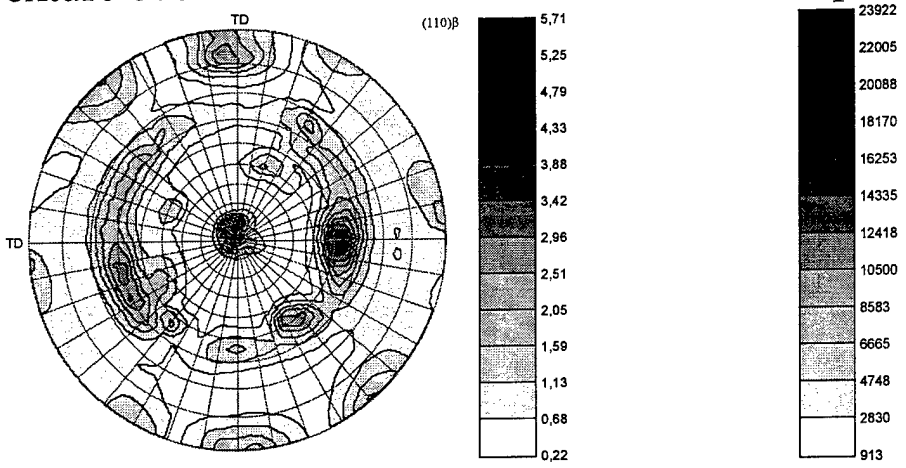

Figure 58. (110)β pole figure of condition A: HR and RP (alpha+beta – 760°C) TIMETAL-LCB. Heating rate 10 Ks^{-1}.

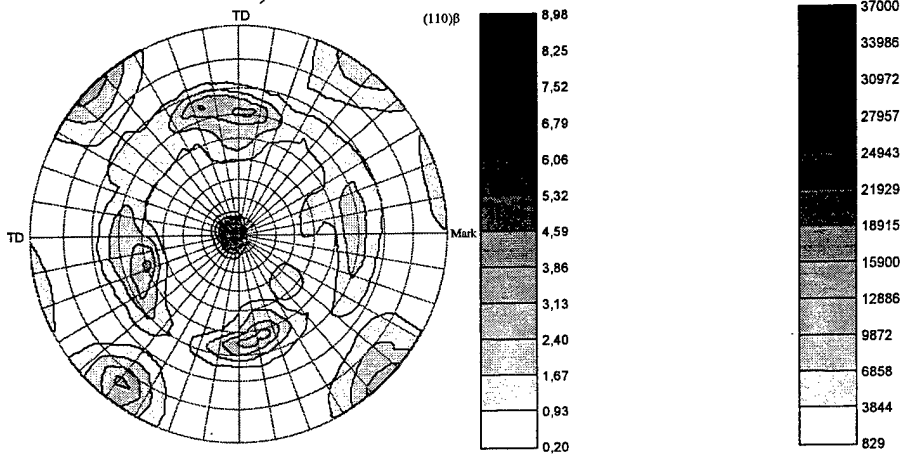

Figure 59. (110)β pole figure of condition B: HR and RR (beta-830°C) TIMETAL-LCB. Heating rate 10 Ks^{-1}.

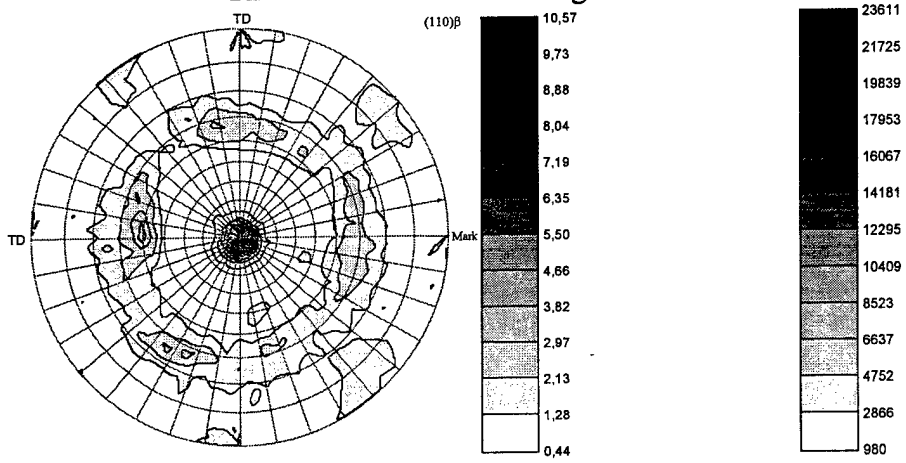

Figure 60. (110)β pole figure of condition C: HR and RR (beta-850°C) TIMETAL-LCB. Heating rate 10 Ks^{-1}.

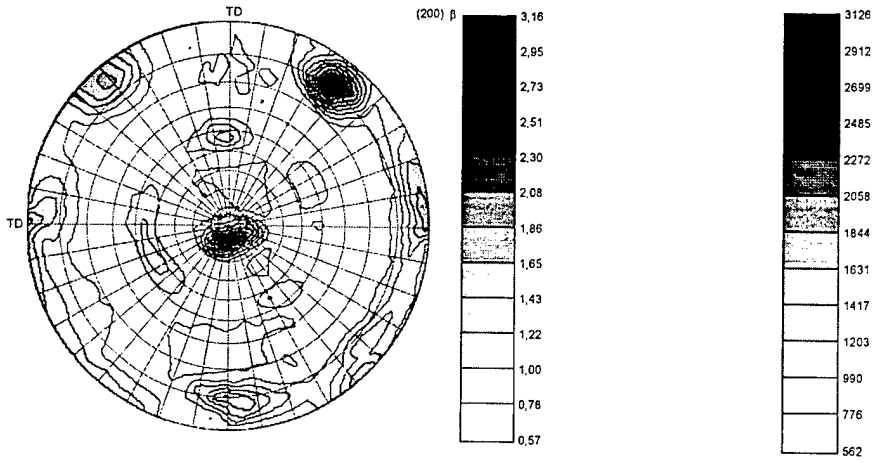

Figure 61. (200)β pole figure of condition A: HR and RP (alpha+beta – 760°C) TIMETAL-LCB. Heating rate 10 Ks^{-1}.

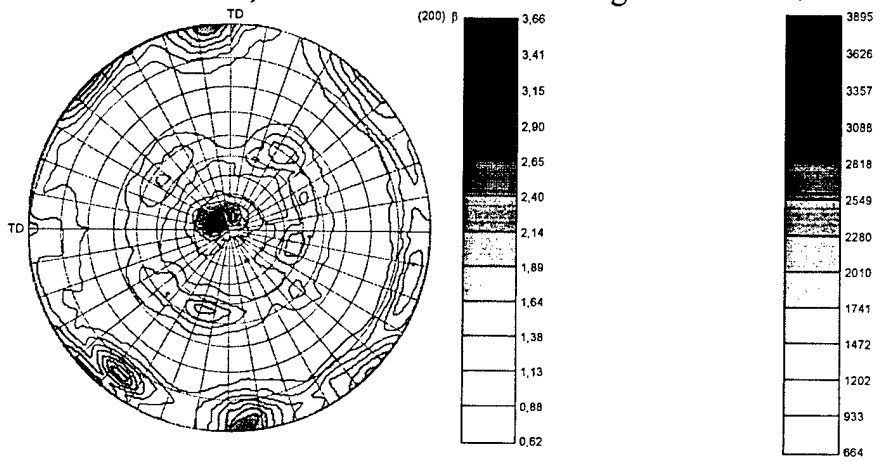

Figure 62. (200)β pole figure of condition B: HR and RR (beta-830°C) TIMETAL-LCB. Heating rate 10 Ks^{-1}.

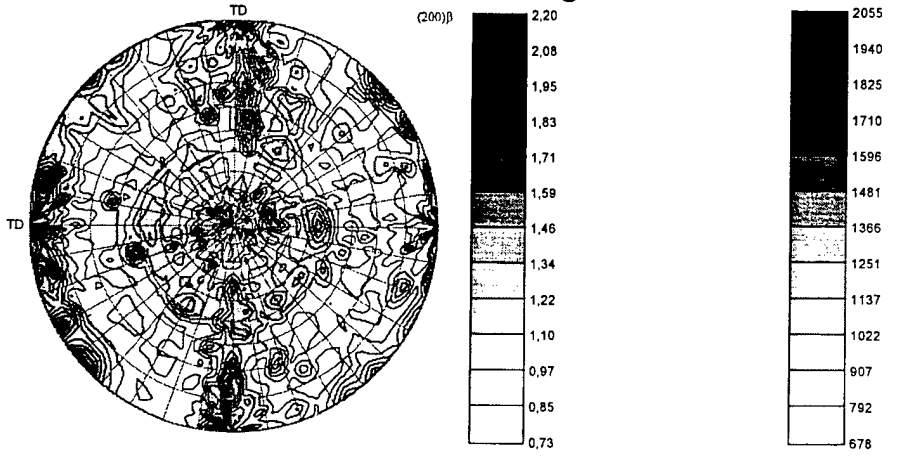

Figure 63. (200)β pole figure of condition C: HR and RR (beta-850°C) TIMETAL-LCB. Heating rate 10 Ks^{-1}.

Table 8
Tensile properties of the TIMETAL-LCB in B and C conditions

TMT/Tension direction	$\sigma_{0.2}$, MPa	UTS, MPa	R.A., %
A/longitudinal	1364	1415	35
A/transverse	1255	1309	9.2
B/longitudinal	1428	1501	33
B/transverse	1328	1386	28.5

In general, rapid heating to higher temperatures caused in more random texture and, hence, more isotropic mechanical properties of material, but at the same time, in coarser beta-grain structure because of monotonic grain growth. So, dilemma to produce the more isotropic material or to allow grains to grow and thus, to deteriorate strength/ductility balance, should be solved depending on a particular application of the heat-treated material.

Ti-15-3

Figures 64 - 75
Tables 9 - 11

Ti-15-3 alloy was treated in accordance to Figure 64. The mechanical properties were compared to those received by treatments presented on Figures 65-66 [Vodolazsky V.F., Popov A.A., et. al., Improvement of production technology for cold rolled Ti-15-3 sheets, Titan, 1(11), 2002, pp. 23-29 (in Russian)].

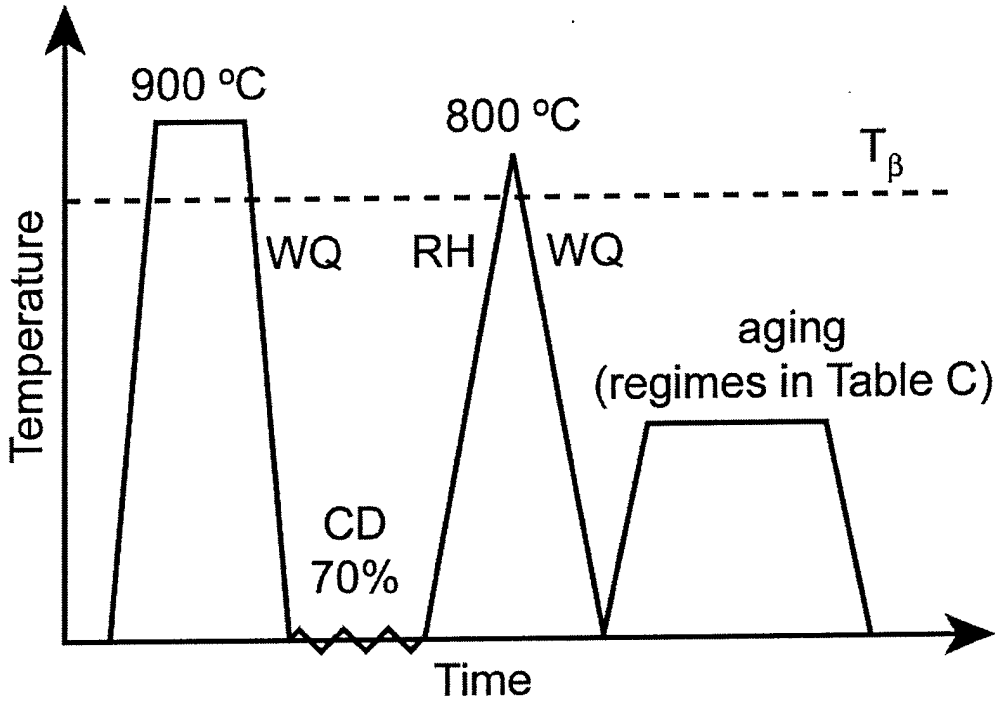

Figure 64. Scheme of Ti-15-3 thermomechanical processing and RH treatment. Results of tensile properties testing are listed in Table 9.

Table 9

Mechanical properties of Ti-15-3 after RHT, as shown in Figure 64.

##	Condition	Properties			
		YS, MPa	UTS, MPa	A_5, %	RA, %
Initial Conditions					
1	ST	830	840	22.7	72
2	ST + CD70 + 450 °C, 16h	1940	1960	0.32	-
3	*RR*	770	780	28.8	81
RR+ Single Aging					
4	*RR* + 450 °C, 8h	1180	1310	11.1	39
5	**RR + 450 °C, 16h**	**1270**	**1370**	**8.3**	**37**
6	*RR*+ 538 °C, 8h	975	1085	14.5	69
7	*RR* +538 °C, 16h	1030	1120	13.3	68
RR +CD15%+Aging					
8	*RR* + CD15+ 450 °C, 16h	1730	1840	1.5	19
9	**RR + CD15+ 500°C, 8h**	**1450**	**1520**	**6.7**	**38**
10	**RR + CD15+ 500°C, 16h**	**1317**	**1405**	**8**	**32**
11	*RR* + CD15+538°C, 8h	1210	1310	10.5	50
Two Step Aging					
12	**RR + 300°C, 8h + 450 °C, 16h**	**1330**	**1430**	**10.4**	**46**
13	RR+300°C, 8h + 538°C, 8h	995	1095	16.2	68
14	RR+300°C, 8h + 538°C, 16h	1030	1120	17.6	71

Following conclusions can be drawn from above tensile data:

a) Due to very sluggish precipitation kinetics mentioned in previous reports the strength after aging at common temperature (538°C) is low, even after 16 h.

b) Aging at lower temperature results in a reasonable balance between strength and ductility, especially if aging time is 16 h.

c) Even better strength/ductility balance can be obtained by double aging, which allowed to form finer and more uniform precipitation microstructure, similar to that formed on slow heating. Additional experiments are being performed to optimize the exposures at both steps of double aging.

d) Direct aging of heavily deformed condition resulted in very high strength, but zero ductility.

e) Very good balance of tensile strength and ductility was achieved after additional CD (reduction 15%) in RR condition before aging, especially if aging was done at 500°C. Important feature of such treatment is that overall aging time is 8 h only.

f) It should be taken into account that ST condition of Ti-15-3 is the mildest among three program alloys. Therefore, relative increase in strength in this alloy is the biggest among them, despite that absolute value of strength achieved is some lower than in TIMETAL-LCB.

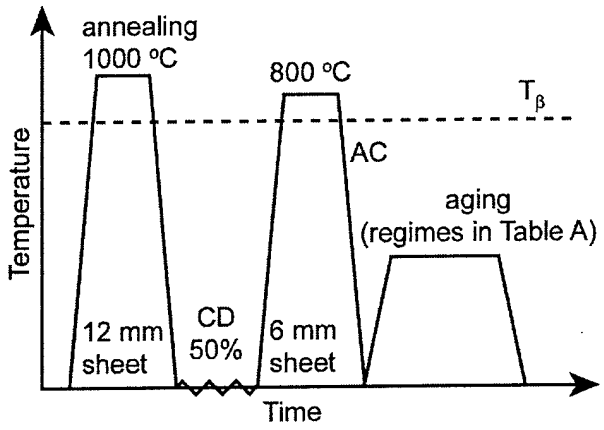

Figure 65. Scheme of Ti-15-3 thermomechanical processing given in [Vodolazsky V.F., Popov A.A., et. al., Improvement of production technology for cold rolled Ti-15-3 sheets, Titan, 1(11), 2002, pp. 23-29 (in Russian)]. Obtained mechanical properties are listed in Table 10.

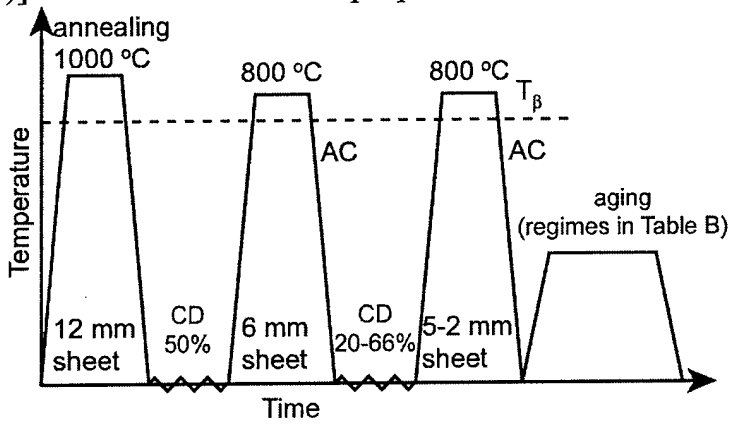

Figure 66. Scheme of Ti-15-3 thermomechanical processing given in [Vodolazsky V.F., Popov A.A., et. al., Improvement of production technology for cold rolled Ti-15-3 sheets, Titan, 1(11), 2002, pp. 23-29 (in Russian)]. Obtained mechanical properties are listed in Table 11.

Table 10
Mechanical properties of Ti-15-3 (6 mm sheet) after treatment shown on Figure 65.

##	Condition	Properties*			
		YS, MPa	UTS, MPa	A_5, %	RA, %
1	Initial deformed	948 980	988 1037	5.3 4.7	39.2 29.7
2	Solid Solutioned (800°C) and Air Cooled	730 690	773 714	11.3 11.7	63 66
3	Deformed + Aging 538°C, 8 h	1208 1319	1257 1347	0.7 1.7	5.2 11.8
4	Solid Solutioned + Aging 538°C, 8 h	1006 1061	1159 1155	10.3 9.3	42.1 39.9
5	Deformed + Aging 482°C, 8 h	1436 1557	1485 1557	0.3 0.3	1.3 3.3
6	Solid Solutioned +Aging 482°C, 8 h	1276 1286	1367 1382	5.3 6.0	26.1 27.8

* Longitudinal properties are shown as numerator, transverse properties – as denominator.

Table 11

Mechanical properties of Ti-15-3 after treatment shown on Figure 66.

##	Sheet thickness, mm (reduction, %)	Properties*			
		YS, MPa	UTS, MPa	A_5, %	RA, %
Solid Solutioned and Air Cooled Condition					
1	5 (20)	701 737	741 783	21.7 16.7	61.9 64.5
2	3.2 (45)	720 735	742 757	18.5 13.2	
3	2 (66)	729	769	12.4	
+ Aging 538°C, 8 h					
4	5 (20)	1059 1084	1156 1168	12.7 10	41.8 43.4
5	3.2 (45)	997 1009	1077 1094	8.6 8.4	
6	2 (66)	997	1075	7.6	
+Aging 482°C, 8h					
7	5 (20)	1233 1257	1311 1327	7.7 7.3	29.7 25.6
8	3.2 (45)	1196 1205	1287 1311	6.4 6	
9	2 (66)	1222	1241	5.2	

* Longitudinal properties are shown as numerator, transverse properties – as denominator.

Properties achieved with RHT looks comparable in strength level but, at comparable strengths, are better in ductility due to finer beta grain size.

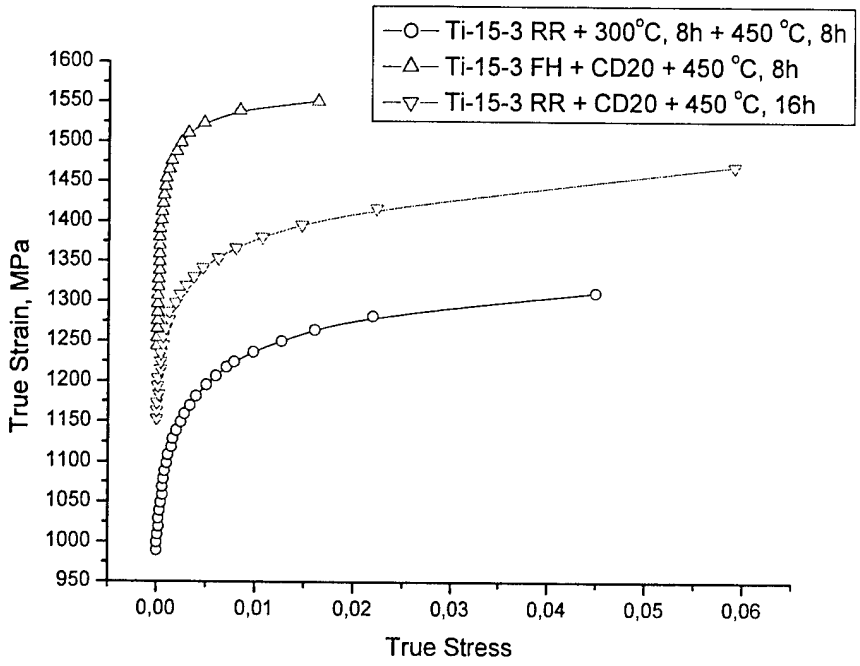

Figure 67. True strain – true stress curves of Ti-15-3 after different treatments.

Precipitation mechanism: TEM

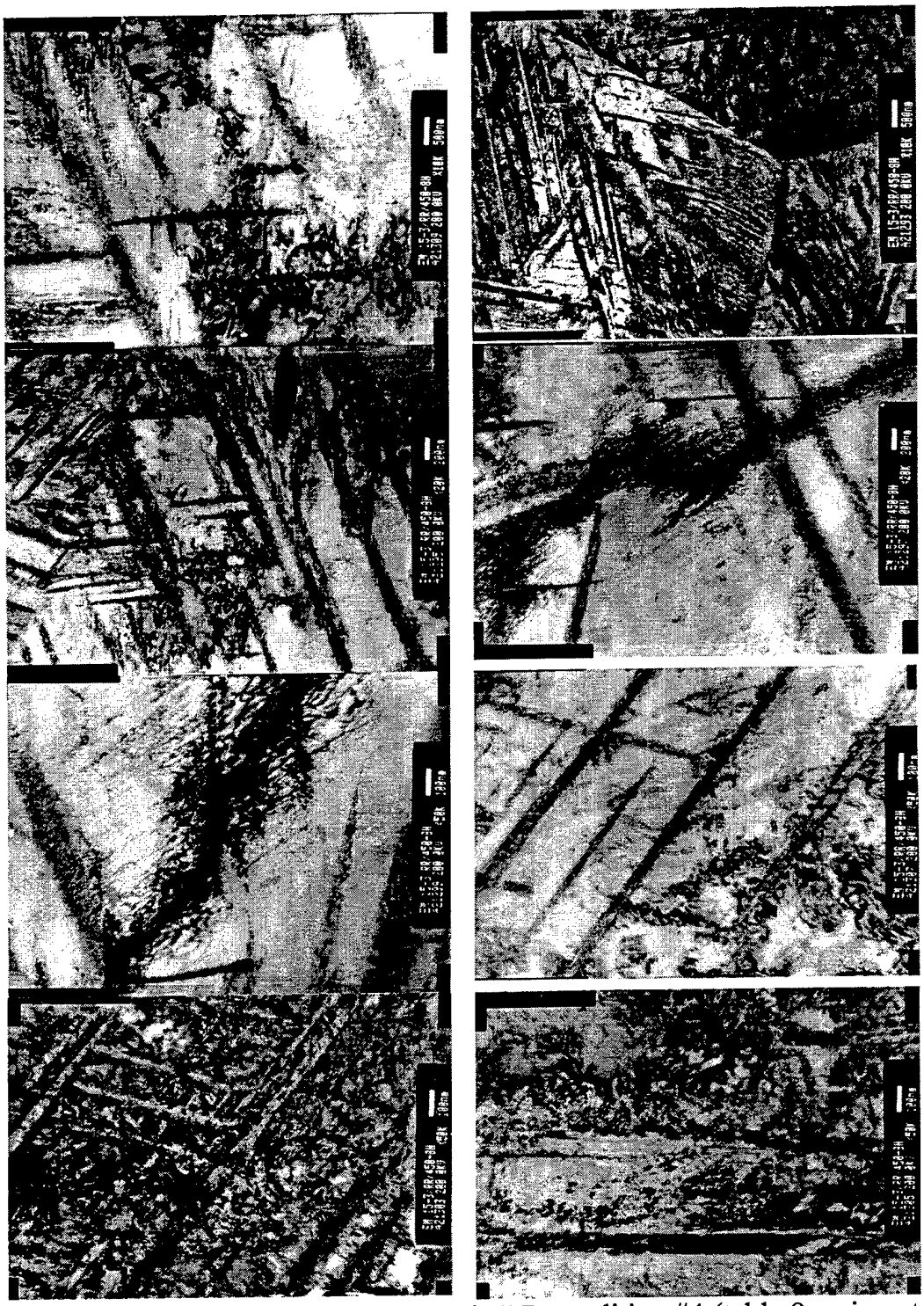

Figure 68. Microstructure of Ti-15-3 in RR condition #4 (table 9, aging at 450°C, 8h).

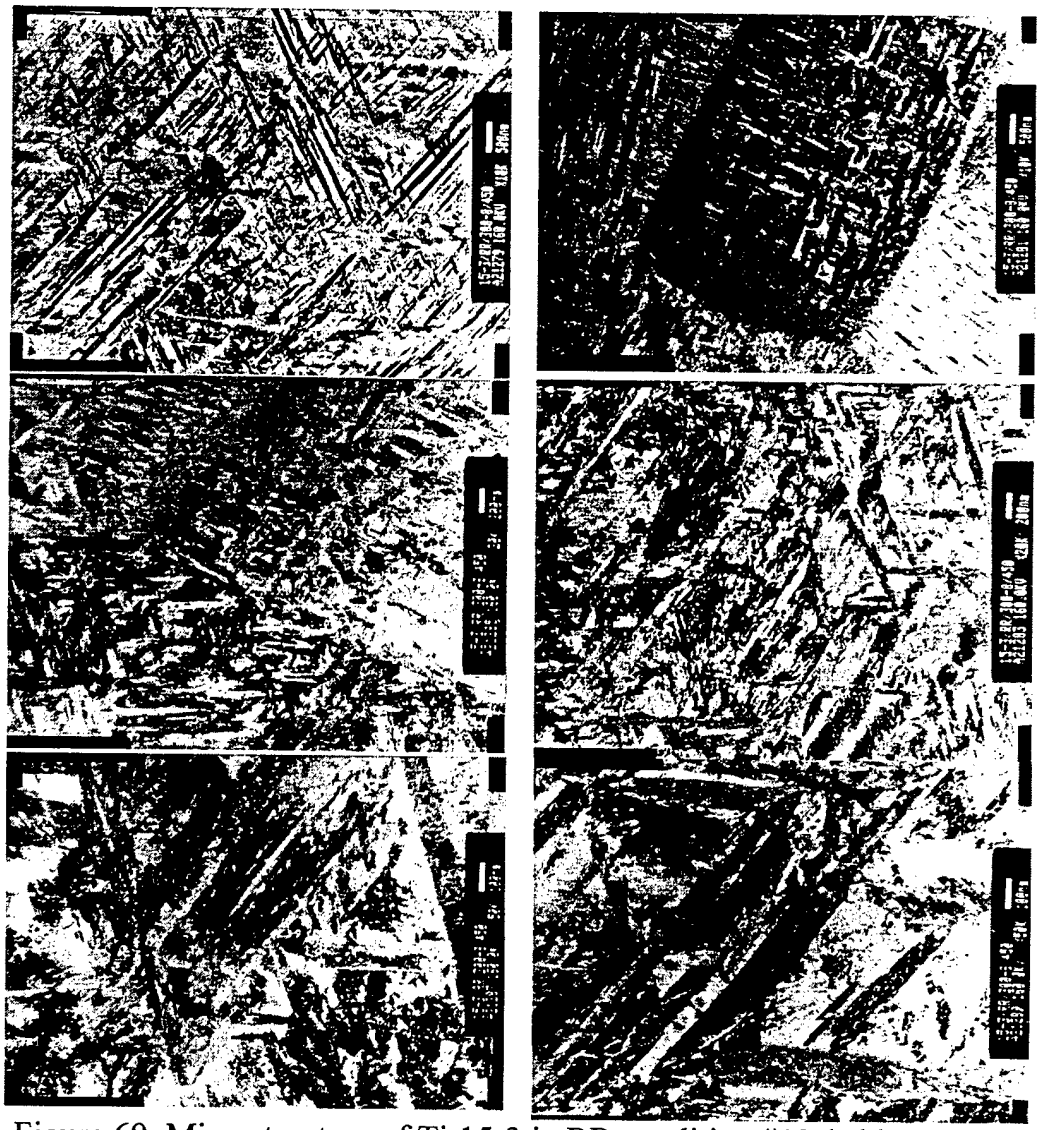

Figure 69. Microstructure of Ti-15-3 in RR condition #12 (table 9, aging at 300°C, 8h + 450°C, 16h).

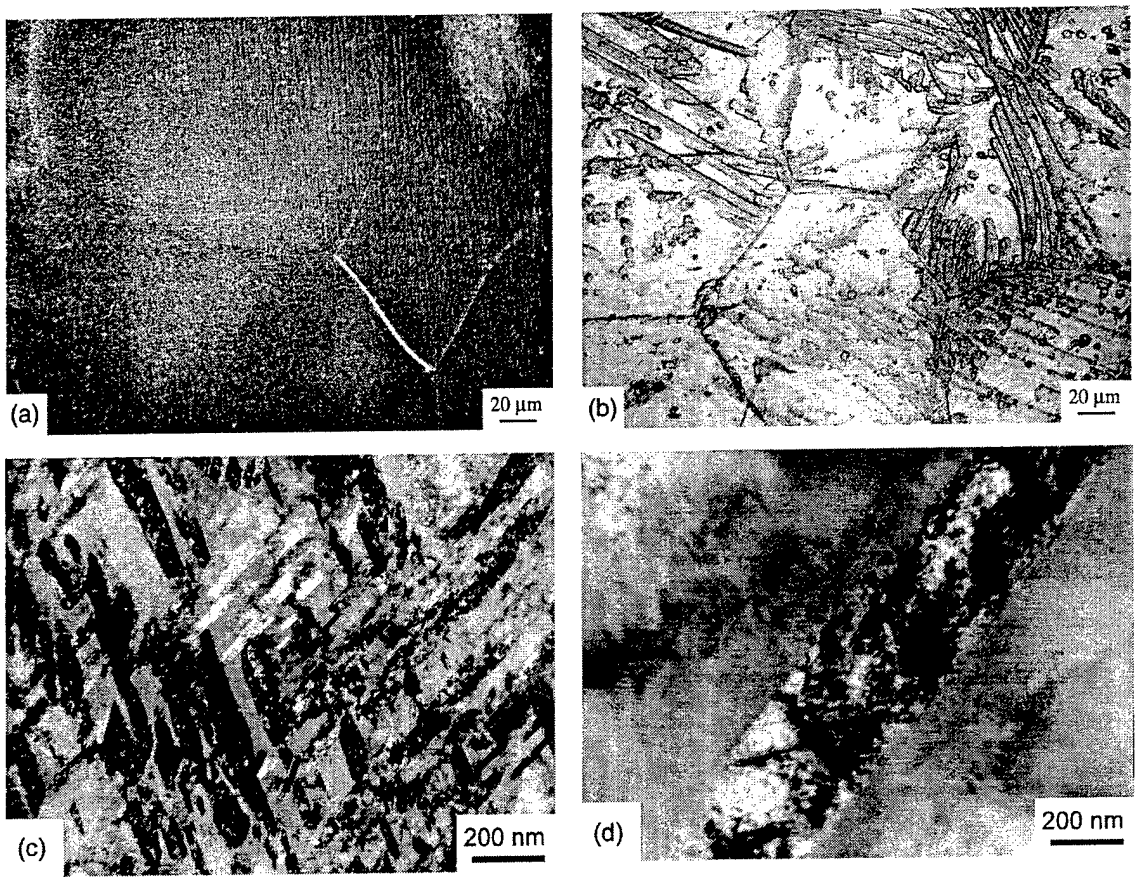

Figure 70. Comparison of microstructure of coarse-grained Ti-15-3 aged at 538°C for 4h after heating with different rates: (a, c) – 0.01 Ks^{-1}, and (b, d) - ~20 Ks^{-1}. (a, b) – LM, (c, d) - TEM.

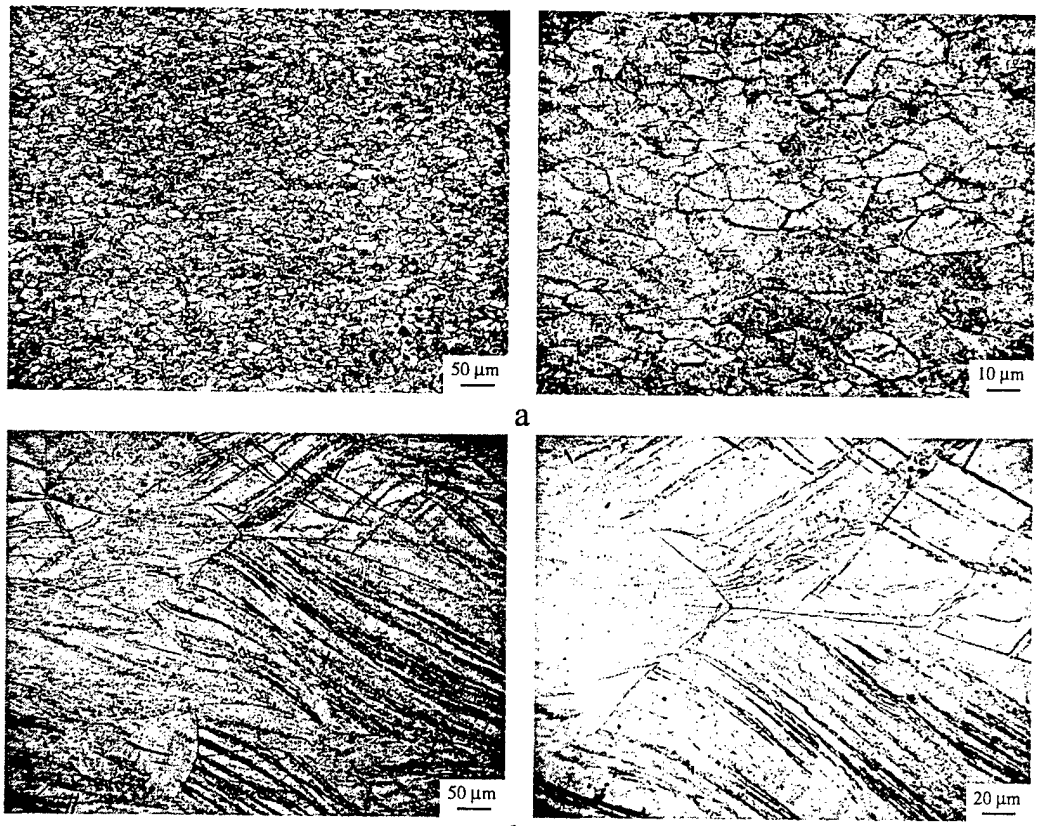

Figure 71. Microstructure of Ti-15-3 in (a) fine-grained (RR) and (b) coarse-grained conditions after additional 20 %CD and subsequent aging at 450°C for 16h. LM.

Additional deformation produces more uniform precipitation structure in fine-grained condition as compared to coarse-grained condition where precipitations generally decorate slip bands.

Precipitation mechanism: X-ray orientation analysis

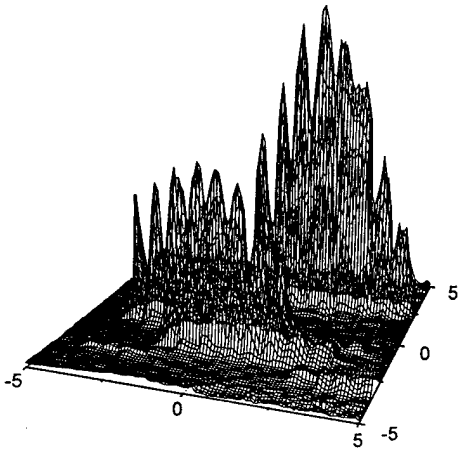

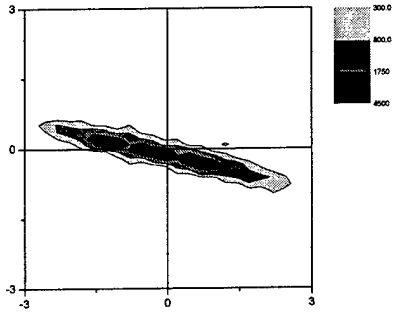

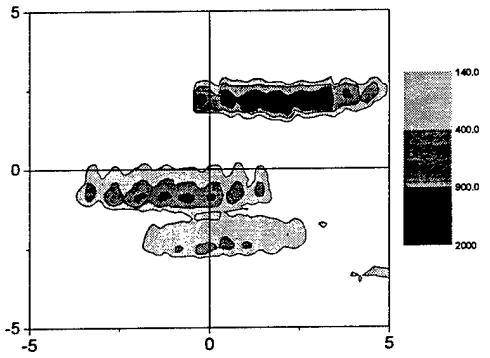

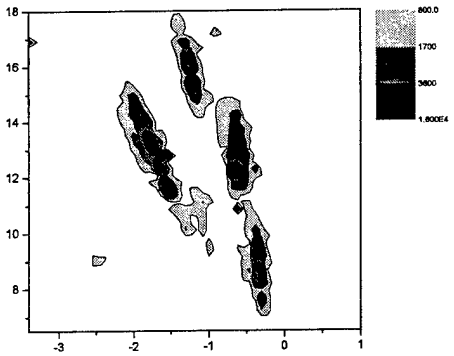

a

b

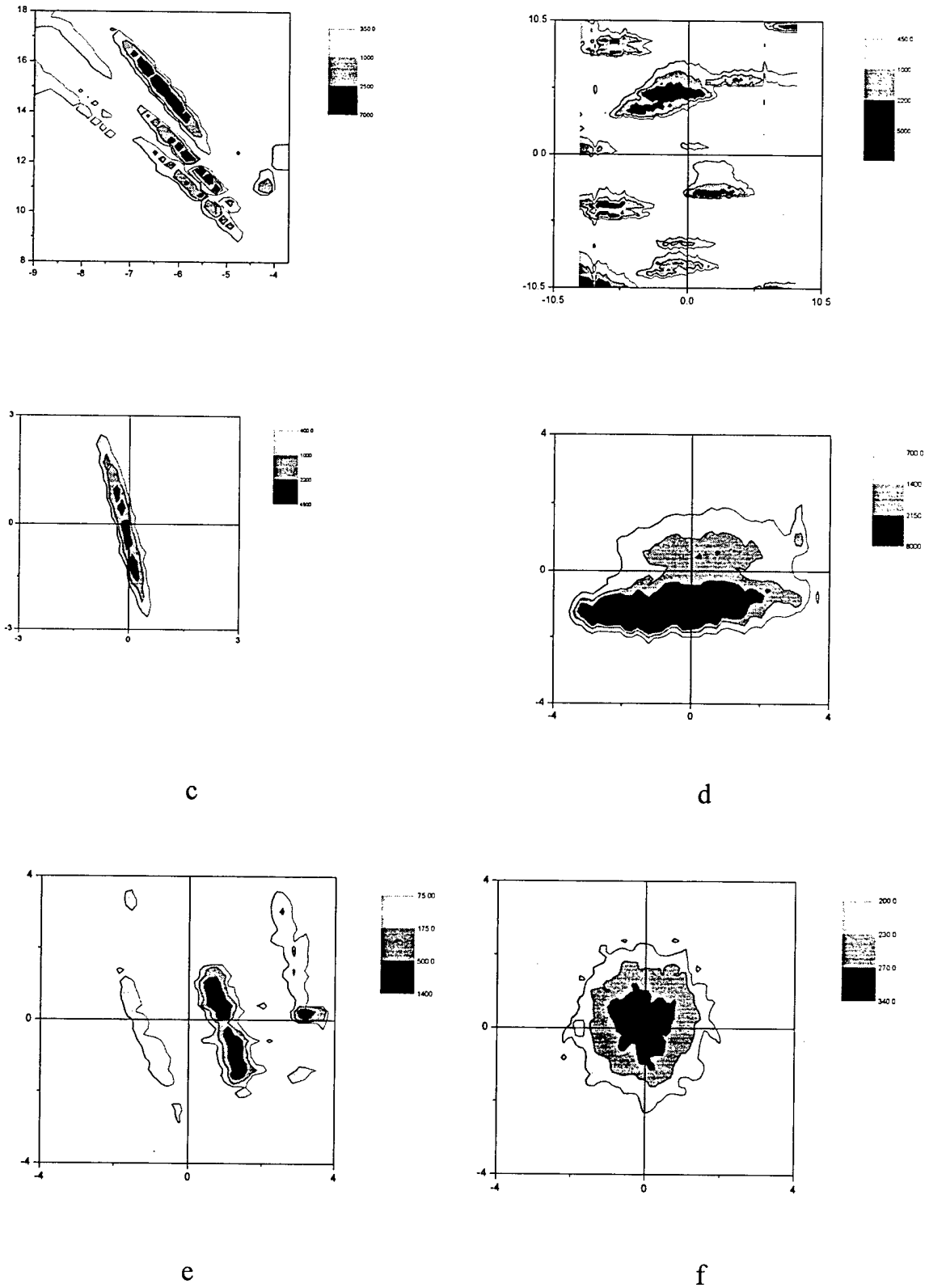

Figure 72. Comparison of evolution of {110}β intensity distributions $\mathbf{I}q_{\perp}$ for (a) solid solutioned and aged at 538 °C for (b) 5', (c) 15', (d) 30', (e) 2h and (f) 12h Ti-15-3.

SEM of fracture surfaces

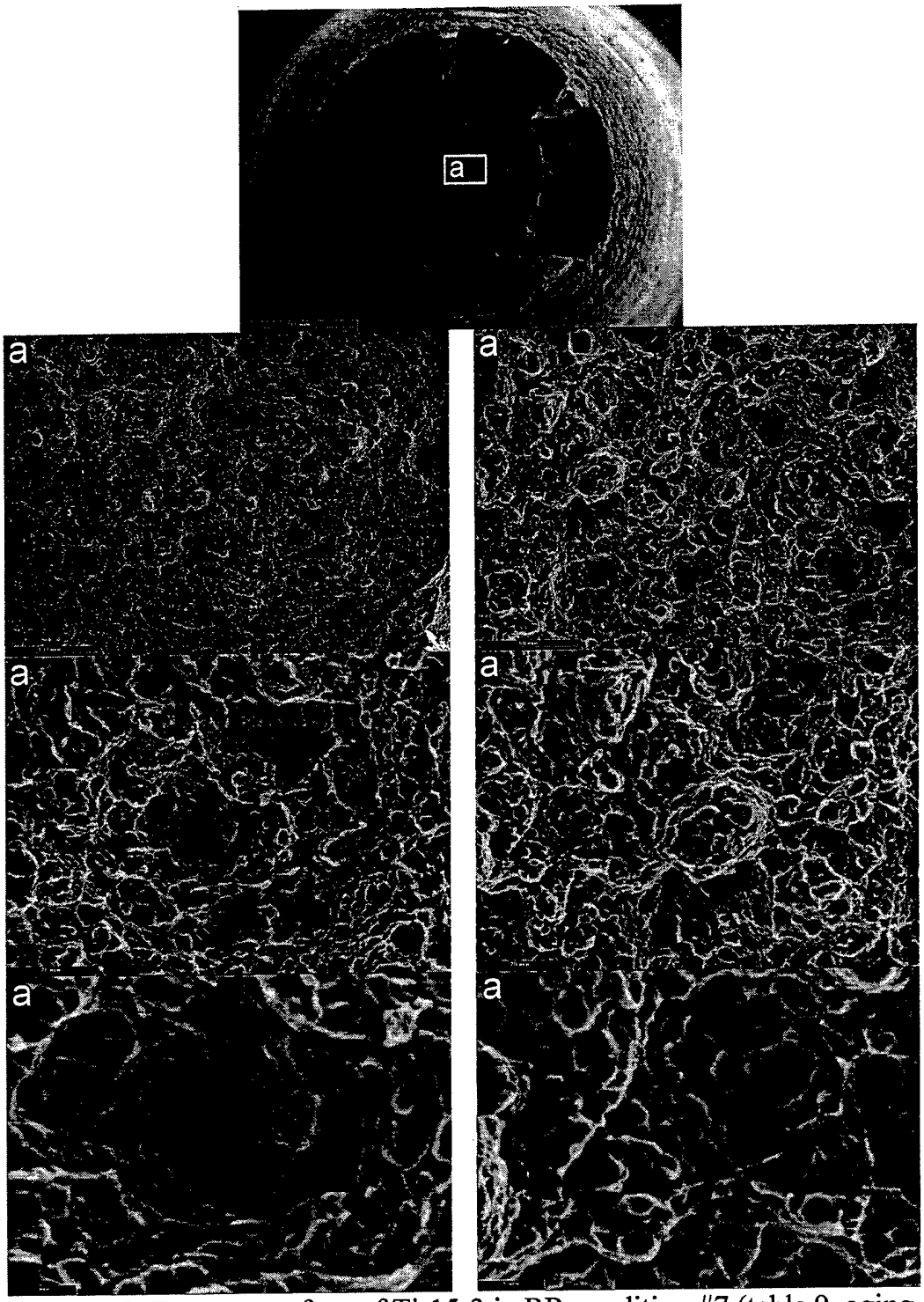

Figure 73. Fracture surface of Ti-15-3 in RR condition #7 (table 9, aging at 538°C, 16h).

Ductile fracture.

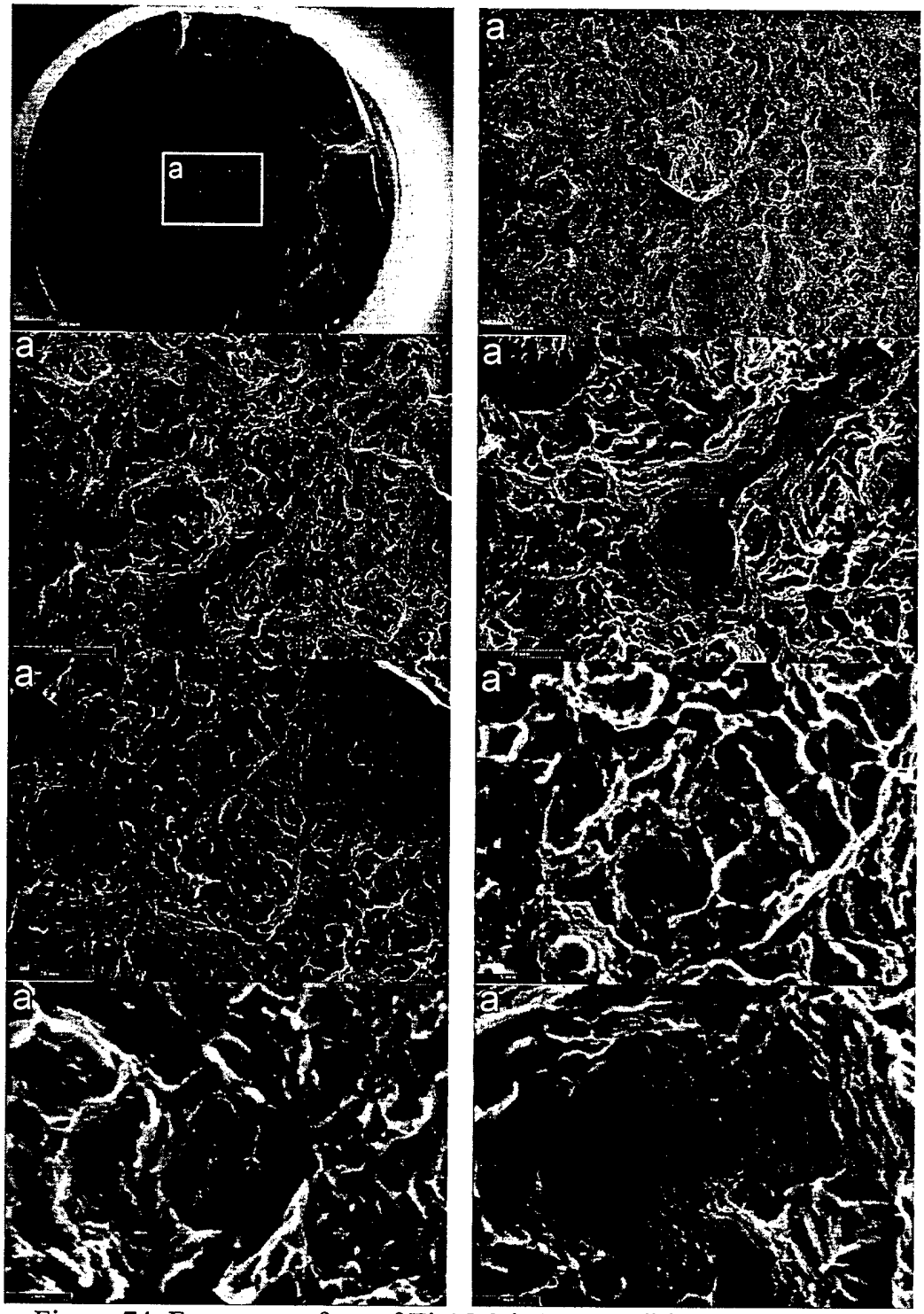

Figure 74. Fracture surface of Ti-15-3 in RR condition #12 (table 10, aging at 300°C, 8h + 450°C, 16h).

The fracture surfaces have indications of both ductile and quasi-brittle mechanisms, significantly less ductile in comparison with the previous case.

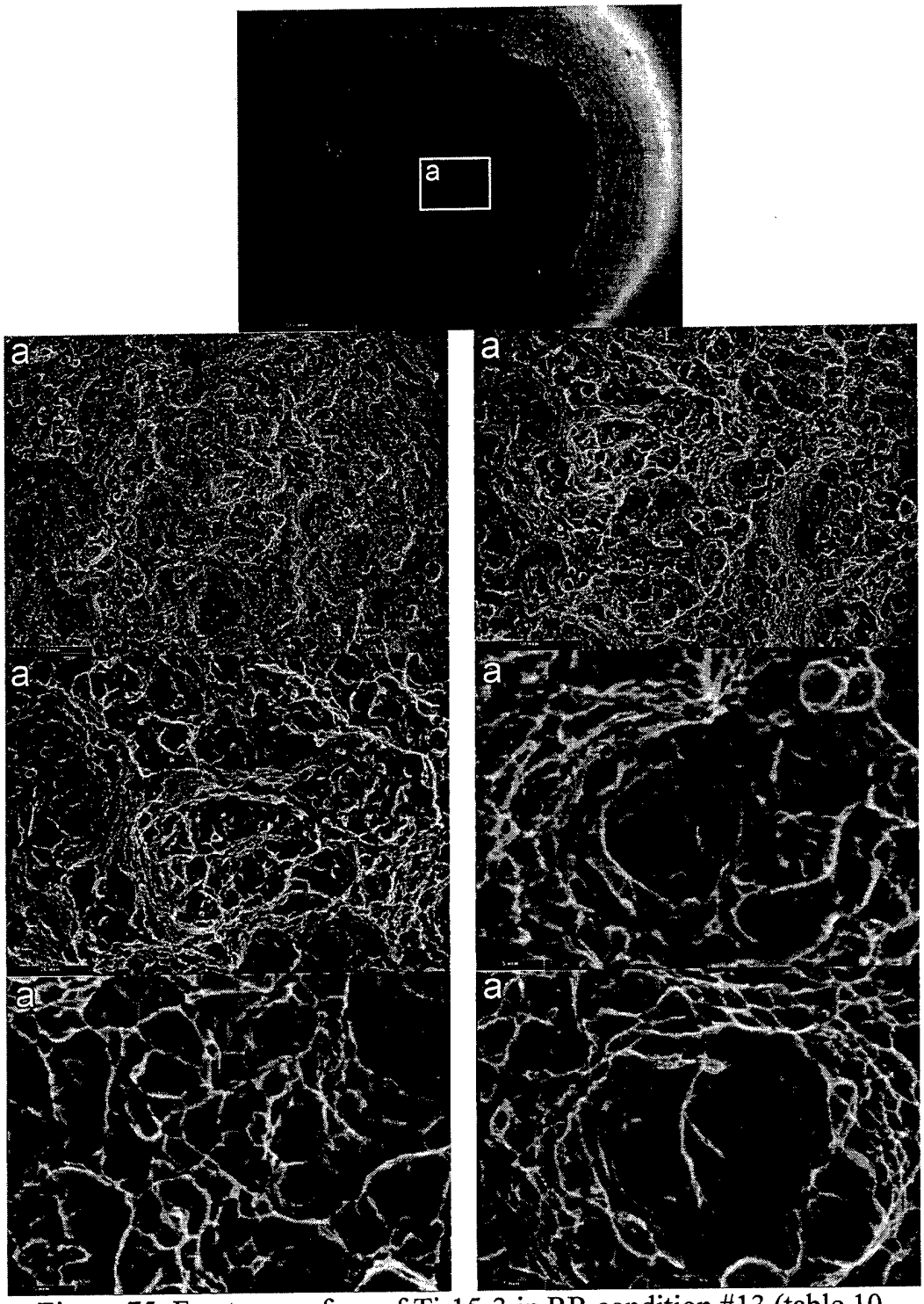

Figure 75. Fracture surface of Ti-15-3 in RR condition #13 (table 10, aging at 300°C, 8h + 538°C, 8h).

Ductile fracture similar to Figure 73.

VT22

Figures 76 – 84
Table 12

Table 12
Mechanical Properties of VT22 after Hot Rolling and different RH-treatments

##	Treatment				Properties			
	Condition	Rapid Heating	Aging	Heating rate	YS, MPa	UTS, MPa	A_5, %	RA, %
First Lot of Specimens (content of oxygen ≈ 0.3 wt.%)								
1	RP	20 Ks^{-1} 950°C	560°C, 8h	0.16 Ks^{-1}	1650	1665	0.32	1
2	RP	20 Ks^{-1} 950°C	560°C, 8h	20 Ks^{-1}	1595	1635	1.2	2.5
3	*RR*	***20 Ks^{-1} 1010°C***	***560°C, 8h***	***0.16 Ks^{-1}***	1680	1730	2.53	12
4	*RR)*	***20 Ks^{-1} 1010°C***	***560°C, 8h***	***20 Ks^{-1}***	1560	1590	0.66	1
5	RP	20 Ks^{-1} 950°C	600°C, 8h	0.16 Ks^{-1}	1450	1480	0.52	1
6	RP	20 Ks^{-1} 950°C	600°C, 8h	20 Ks^{-1}	1480	1520	1.72	2.5
7	*RR*	***20 Ks^{-1} 1010°C***	***600°C, 8h***	***0.16 Ks^{-1}***	1240	1355	2.2	11
8	*RR*	***20 Ks^{-1} 1010°C***	***600°C, 8h***	***20 Ks^{-1}***	1350	1420	2.42	4.2
9	RP	20 Ks^{-1} 950°C	640°C, 8h	0.16 Ks^{-1}	1410	1465	1.52	3.1
10	*RR*	***20 Ks^{-1} 1010°C***	***640°C, 8h***	***0.16 Ks^{-1}***	**1330**	**1410**	**7.5**	**12**
Second Lot of Specimens (content of oxygen ≈ 0.1 wt.%)								
11	*RR*	***20 Ks^{-1} 1010°C***	***600°C, 8h***	***0.16 Ks^{-1}***	**1330**	**1380**	**6.5**	**47**
12	*RR*	***20 Ks^{-1} 1010°C***	***560°C, 8h***	***0.16 Ks^{-1}***	1575	1588	2.3	21
13	*RR*	***20 Ks^{-1} 1010°C***	***640°C, 8h***	***0.16 Ks^{-1}***	1310	1355	9.8	52
14	RP	20 Ks^{-1} 950°C	640°C, 8h	0.16 Ks^{-1}	1380	1427	3.2	16

Tensile tests of the VT22 showed worse possibilities to control strength/ductility balance. Strength of both, recrystallized and polygonized microstructures varied from 1600 to 1350 MPa strength, but ductility in this high-strength condition was low. Only recrystallized condition aged at 640°C, 8h allowed to receive acceptable balance of strength and ductility. Comparison of data for different oxygen content showed that poor ductility only partly could be related to prior high-temperature processing and, correspondingly, higher than specified interstitial content. Main problem, however, is that the finest the finest obtained grain size was of about 50 μm because it was achieved not through cold, but hot deformation. It was concluded that high strength in excess of 1500 MPa balanced with reasonable ductility needs an essentially finer grain size and therefore is hardly to be possible in this alloy.

Precipitation mechanism: TEM

Figure 76. Microstructure of VT22 in RR condition #12 (table 12, aging at 560°C, 8h, heating rate to aging temperature 0.16Ks^{-1}).

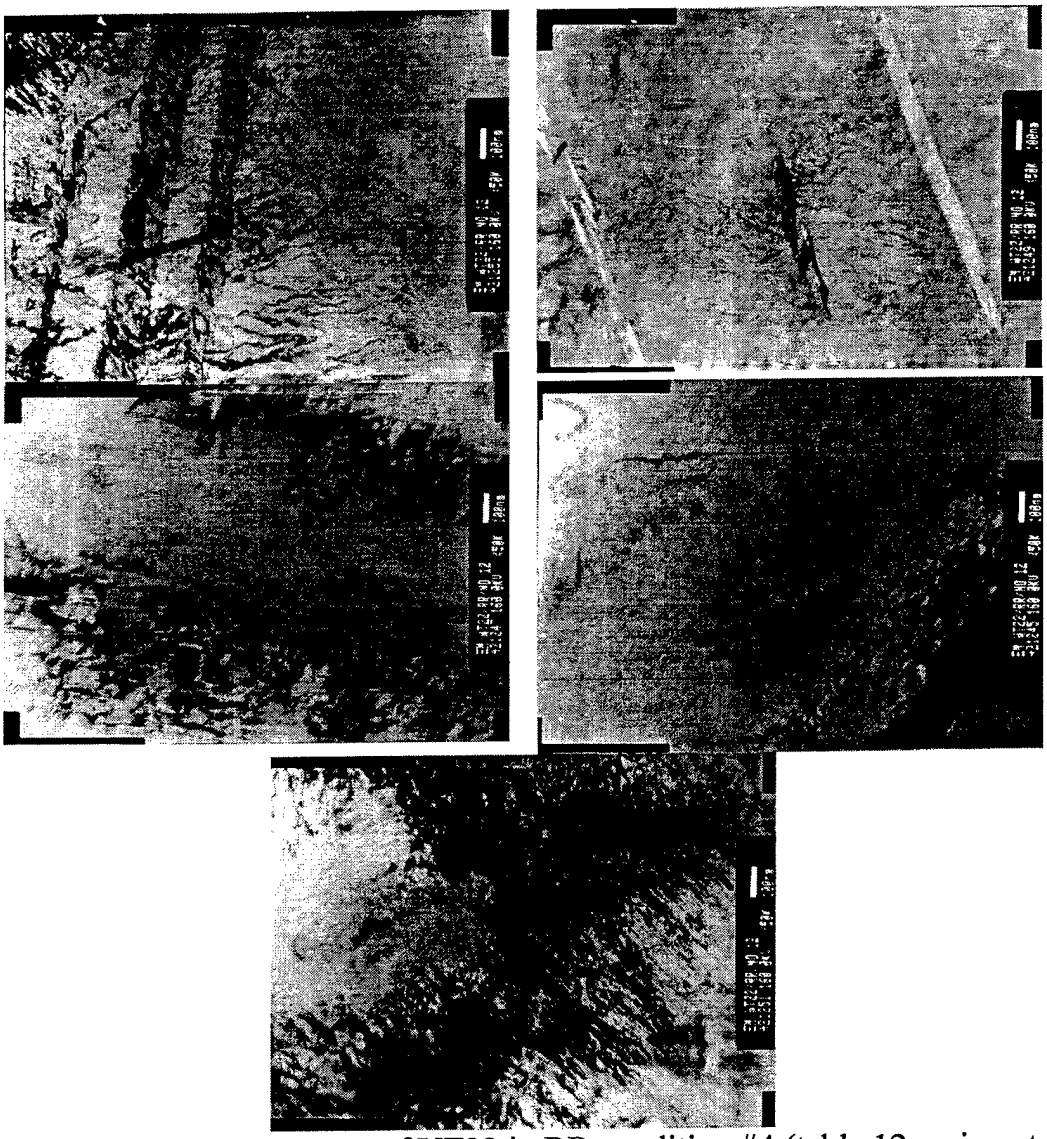

Figure 77. Microstructure of VT22 in RR condition #4 (table 12, aging at 560°C, 8h, heating rate to aging temperature 20Ks^{-1}).

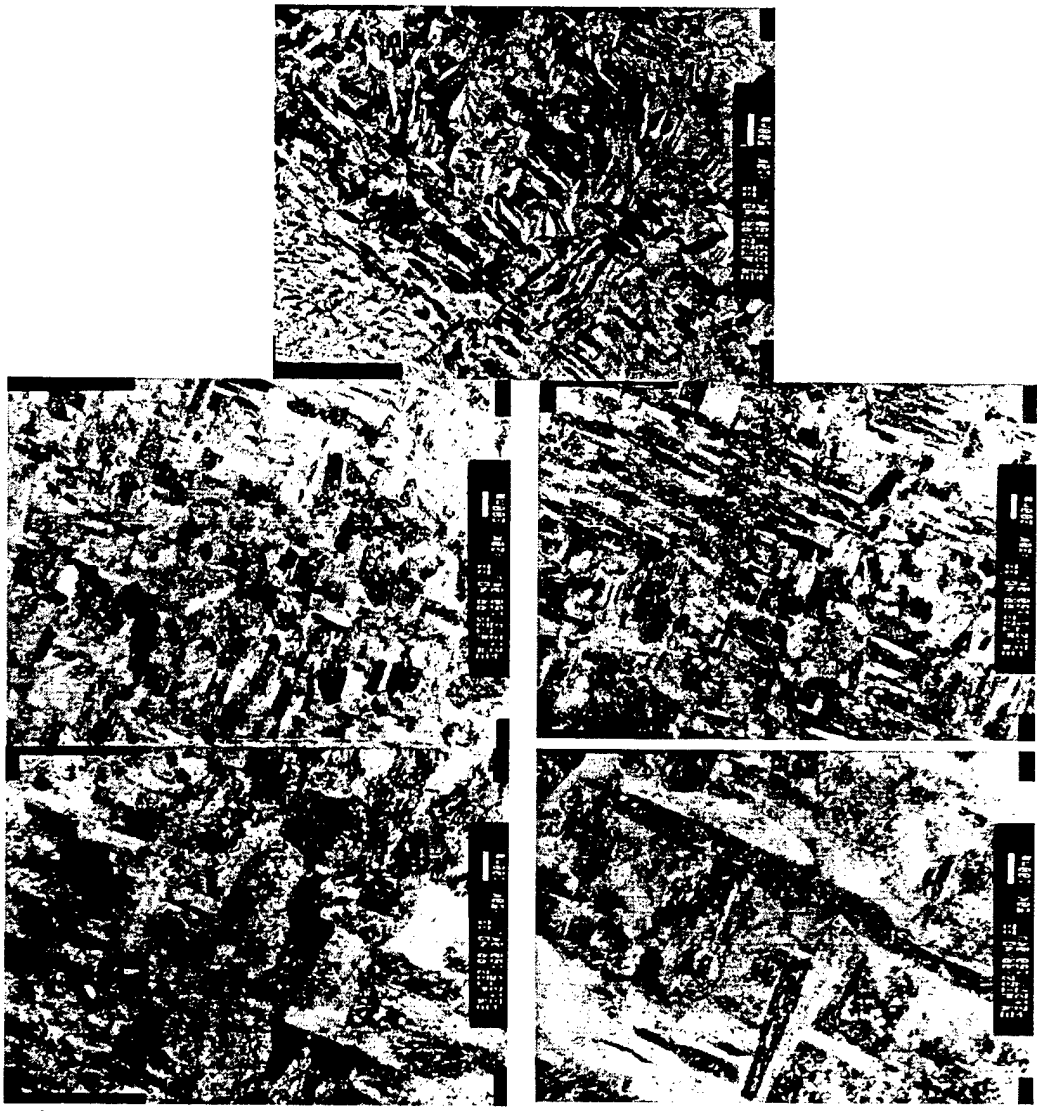

Figure 78. Microstructure of VT22 in RR condition #13 (table 12, aging at 640°C, 8h, heating rate to aging temperature 0.16Ks^{-1}).

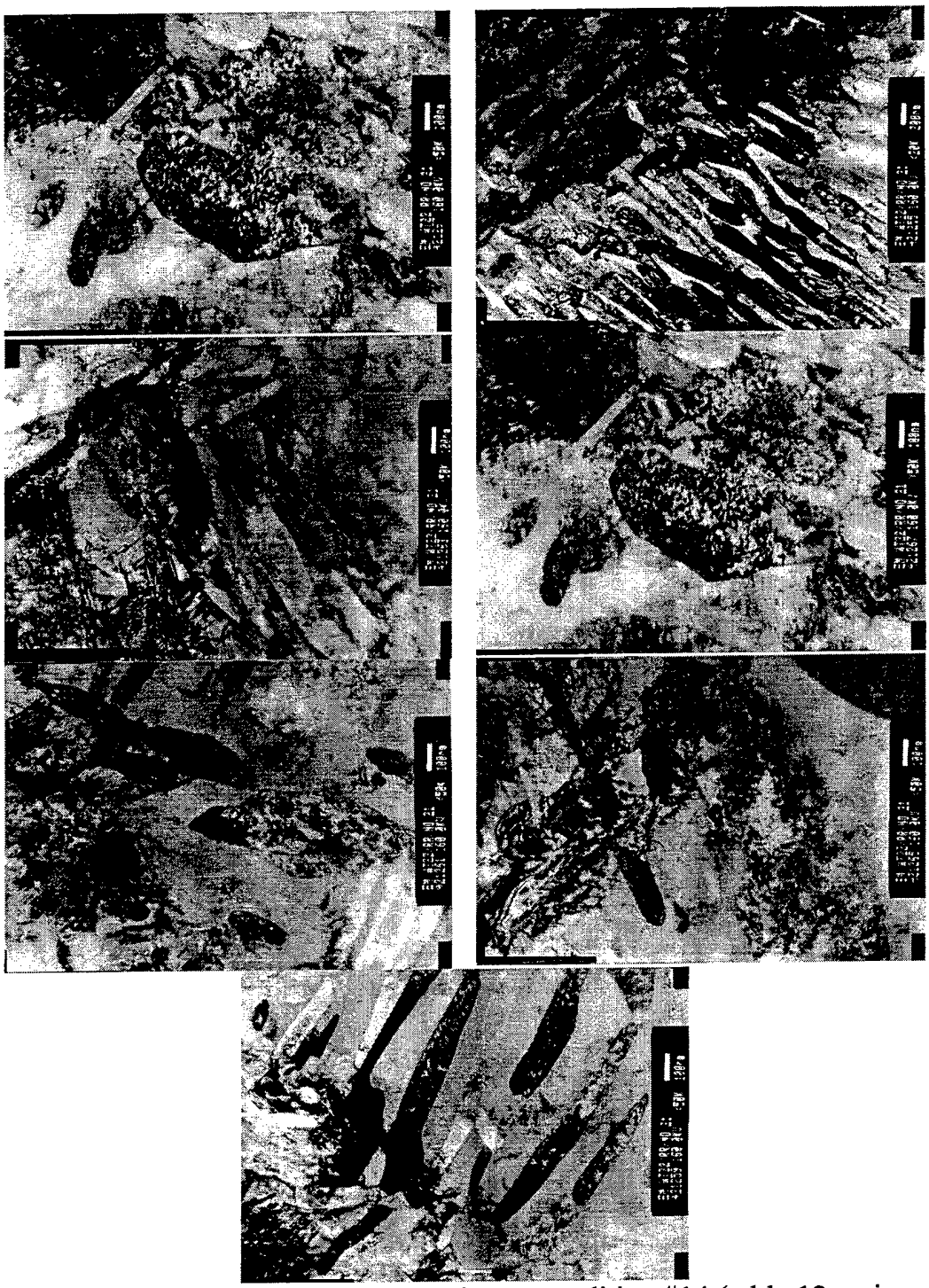

Figure 79. Microstructure of VT22 in RP condition #14 (table 12, aging at 640°C, 8h, heating rate to aging temperature 0.16Ks^{-1}).

Precipitation mechanism: X-ray orientation analysis

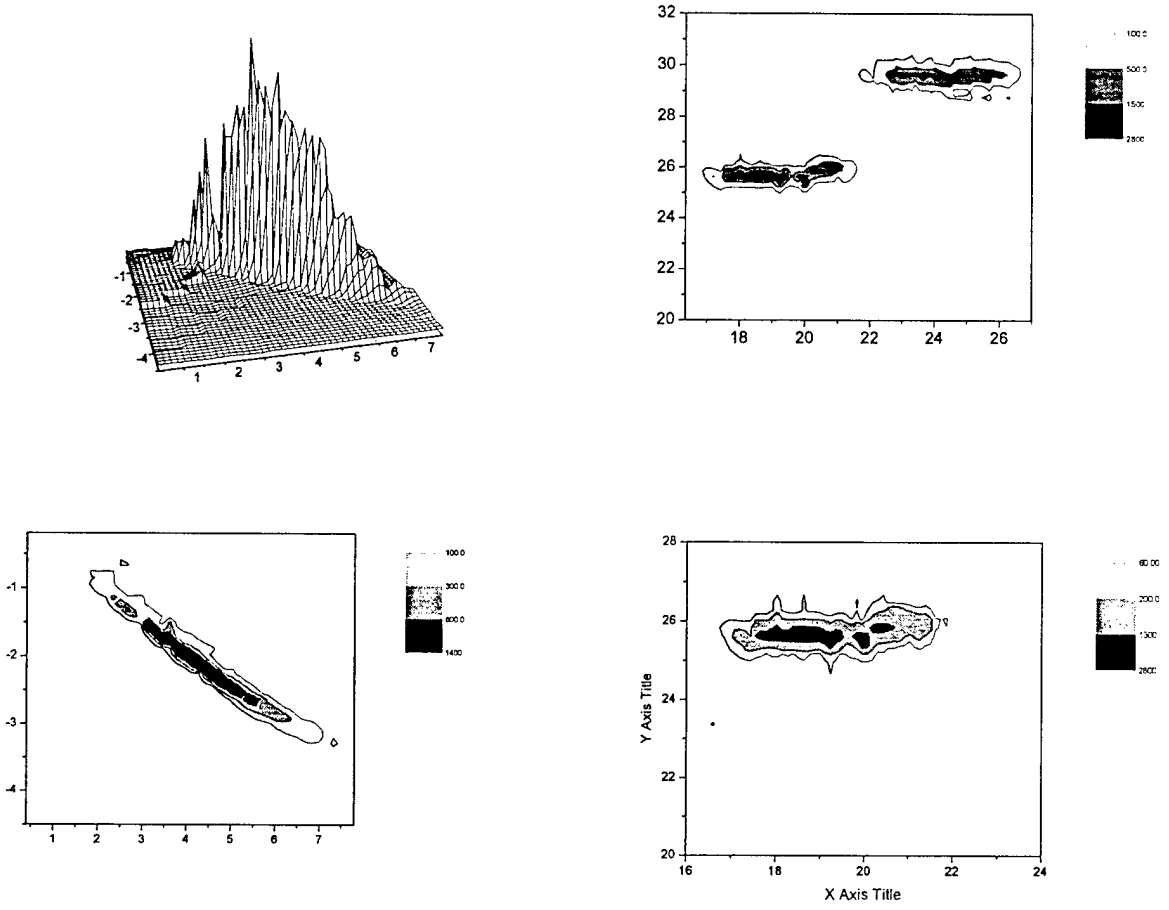

a

b

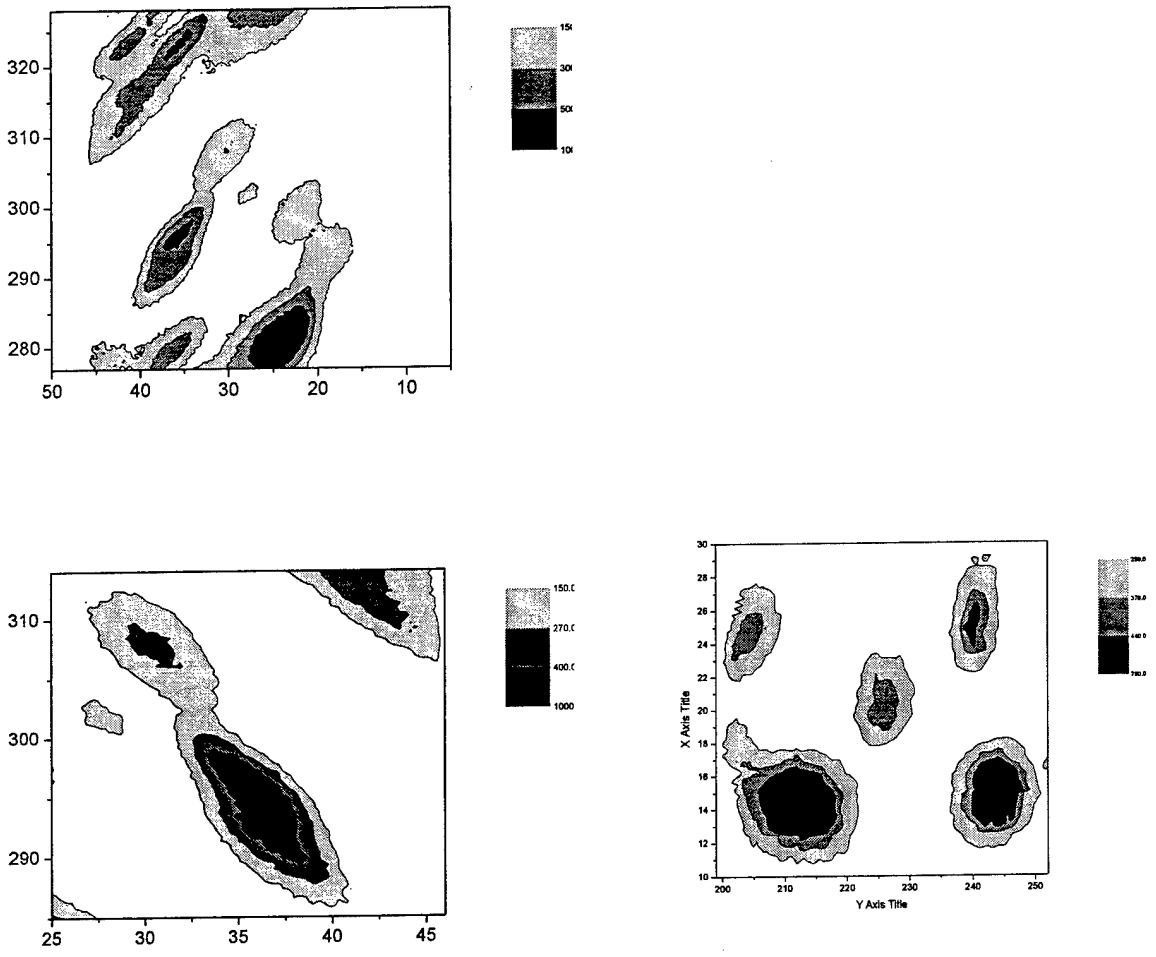

c d

Figure 80. Comparison of evolution of {110}β intensity distributions $Iq_{\perp}$ for (a) solid solutioned and aged at 538 °C for (b) 5', (c) 15' and (d) 30' VT22.

SEM of fracture surfaces

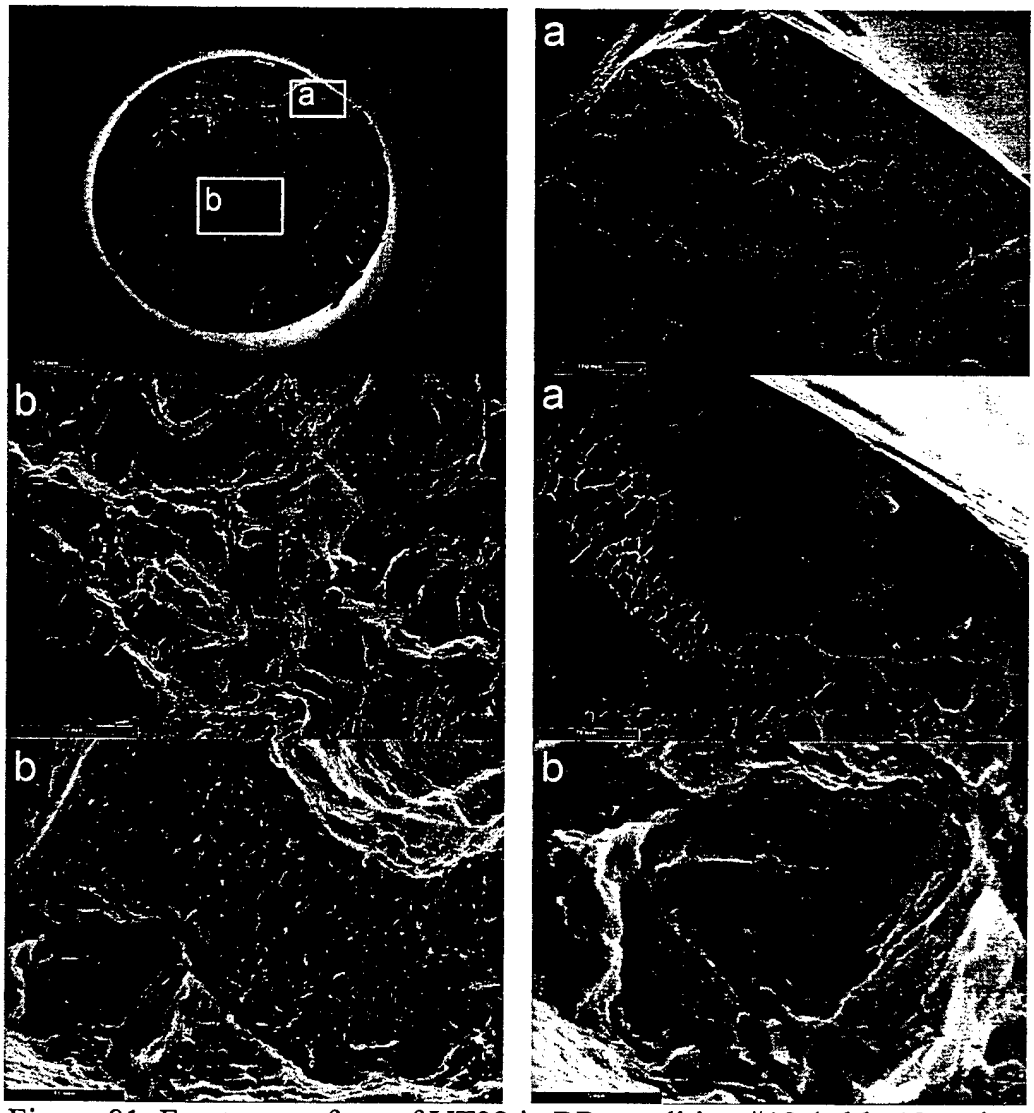

Figure 81. Fracture surface of VT22 in RR condition #12 (table 12, aging at 560°C, 8h, heating rate to aging temperature 0.16 Ks^{-1}).

The fracture surfaces have indications of both ductile and quasi-brittle mechanisms. Areas of quasi-brittle fracture prevail.

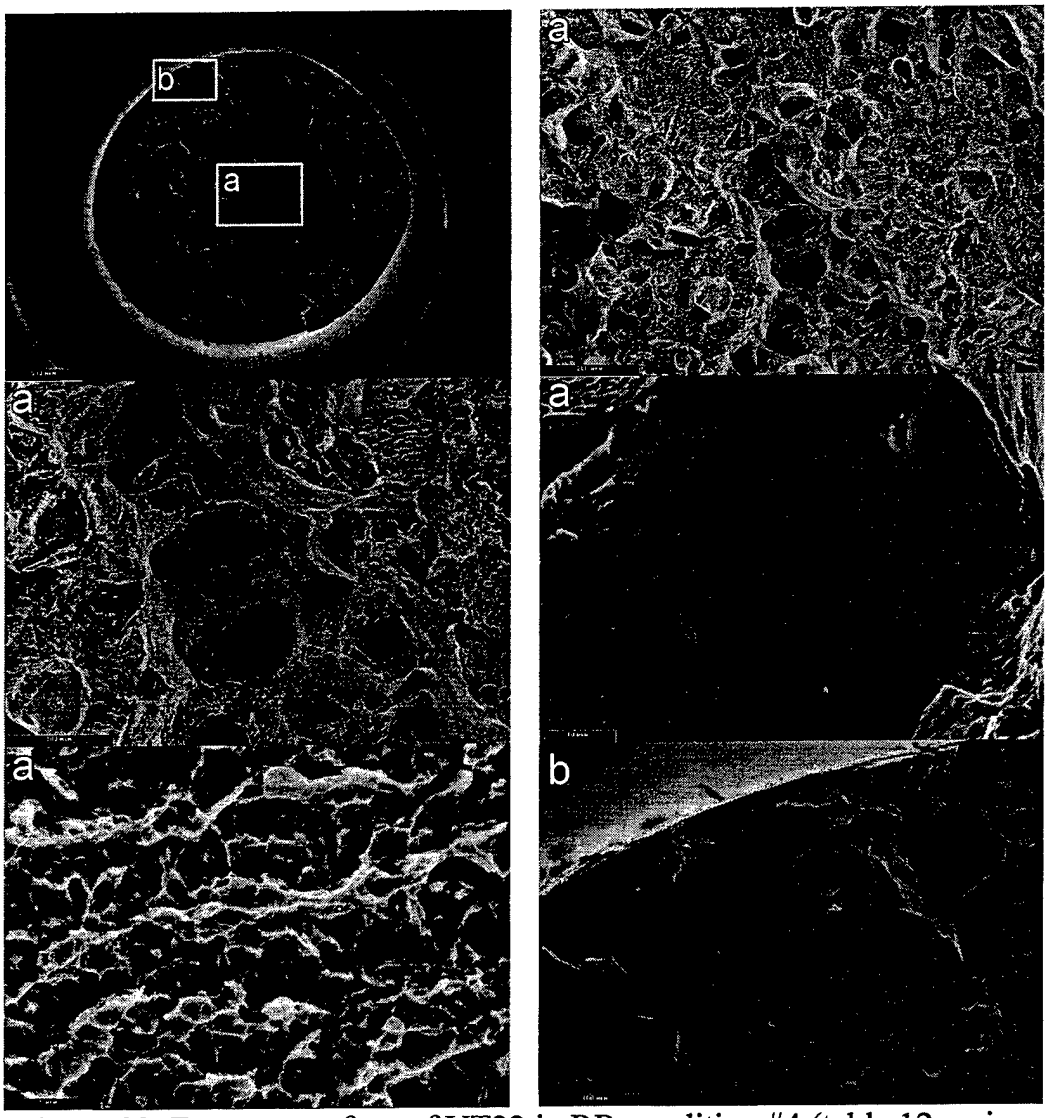

Figure 82. Fracture surface of VT22 in RR condition #4 (table 12, aging at 560°C, 8h, heating rate to aging temperature 20 Ks^{-1}).

Fraction of quasi-brittle areas is significantly higher comparatively to Figure 81.

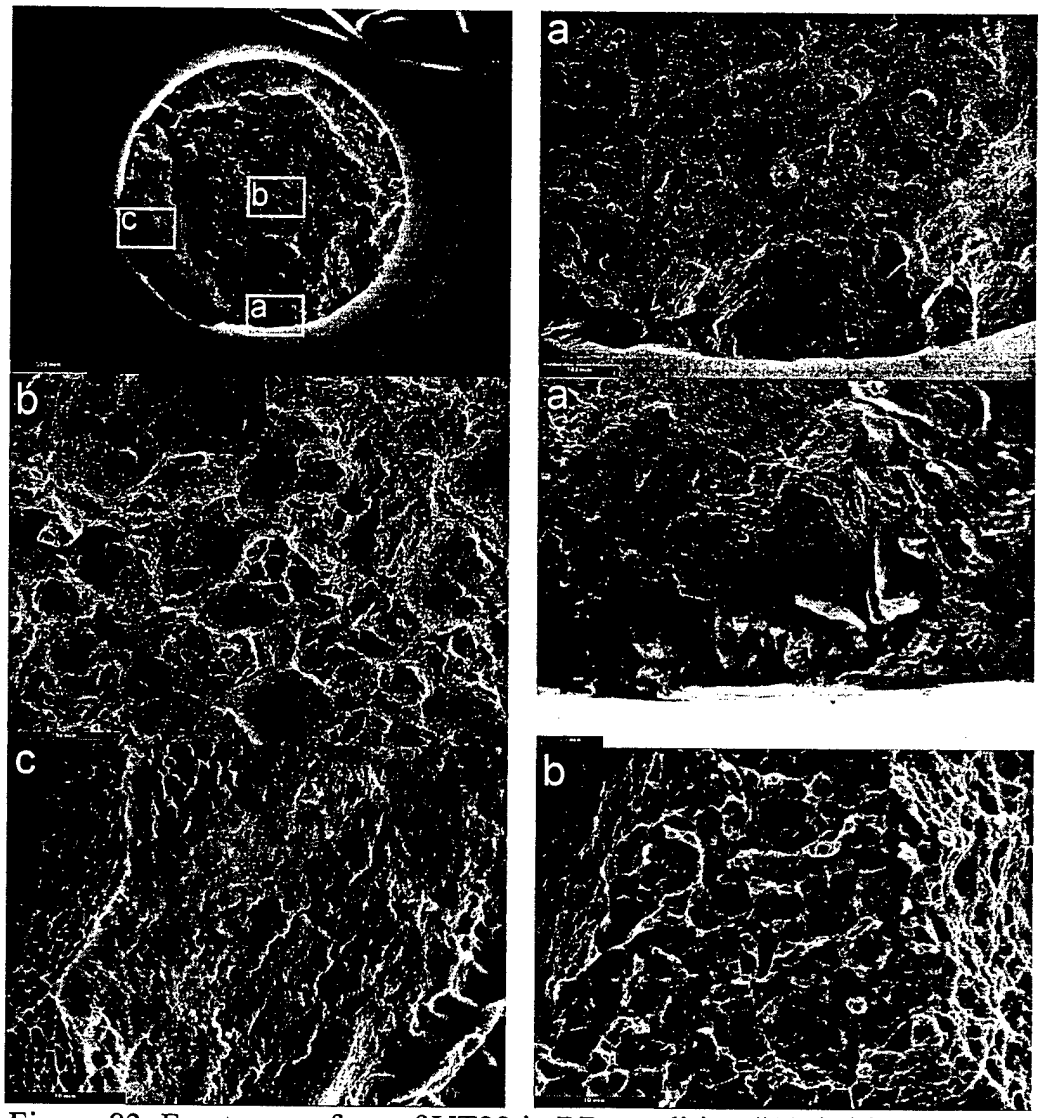

Figure 83. Fracture surface of VT22 in RR condition #13 (table 12, aging at 640°C, 8h, heating rate to aging temperature 0.16 Ks^{-1}).

The fracture is mainly ductile, however some areas of intercrystalline fracture are observed.

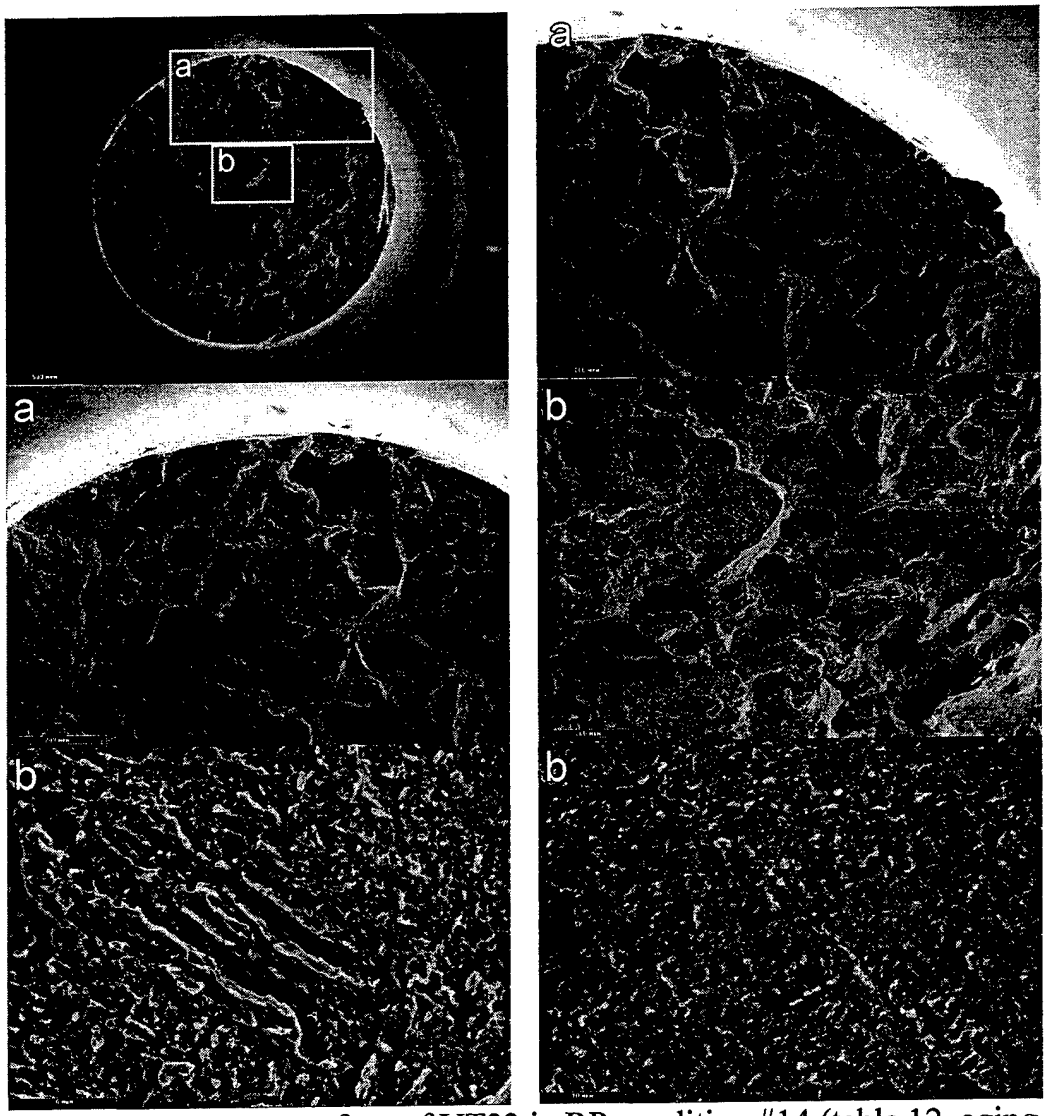

Figure 84. Fracture surface of VT22 in RP condition #14 (table 12, aging at 640°C, 8h, heating rate to aging temperature 0.16 Ks^{-1}).

The fracture surfaces have indications of both ductile and quasi-brittle mechanisms. Areas of quasi-brittle fracture prevail.

Comparison of microstructure/properties relationship in different alloys

Figures 85 - 88

TIMETAL- LCB	Ti-15-3	VT22
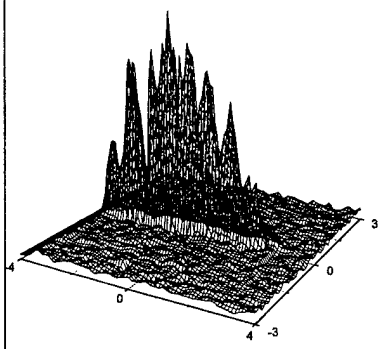	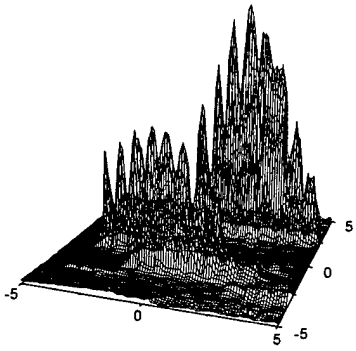	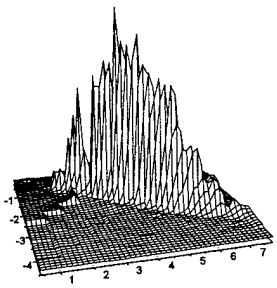
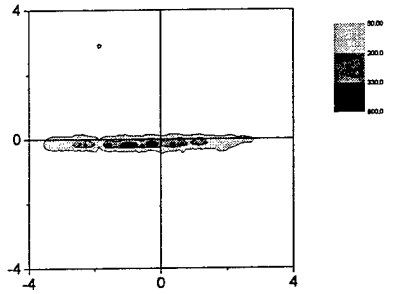	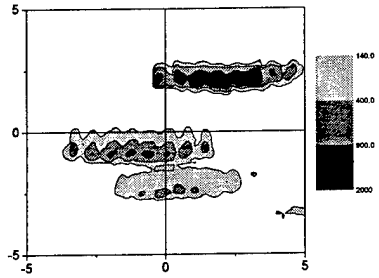	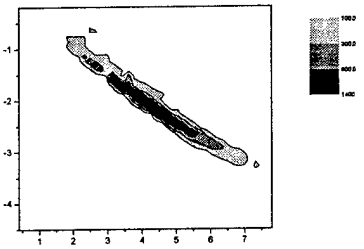
Solid solutioned		
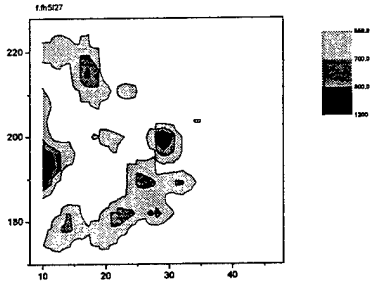	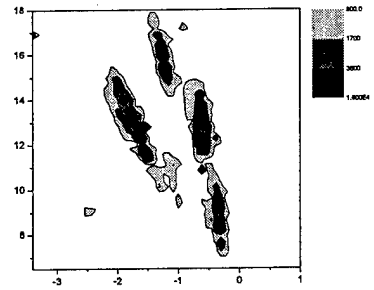	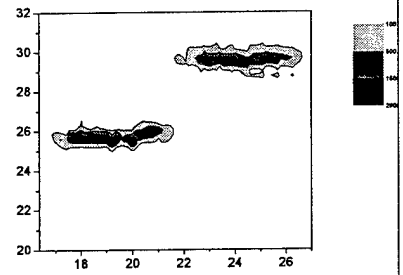
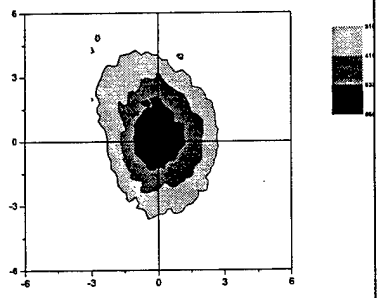	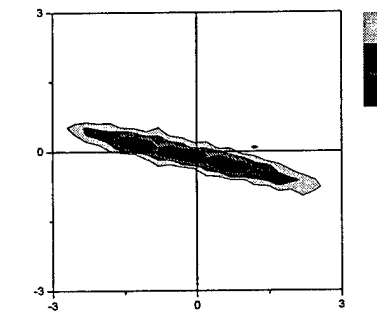	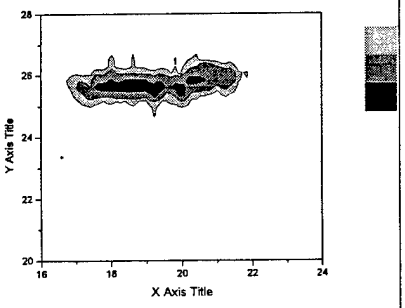
Aging 538°C, 5min		

TIMETAL- LCB	Ti-15-3	VT-22
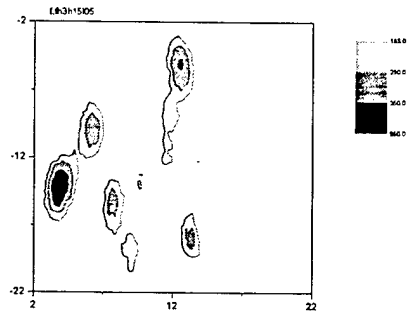	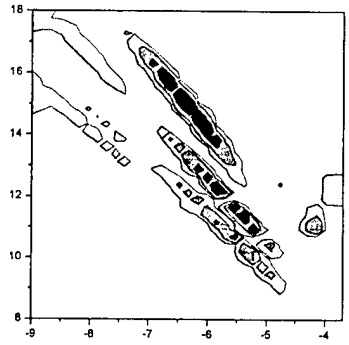	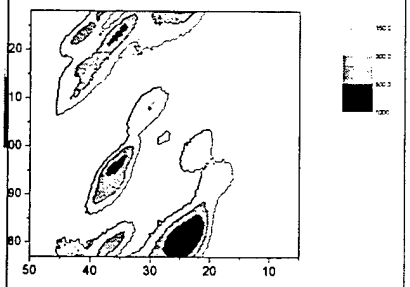
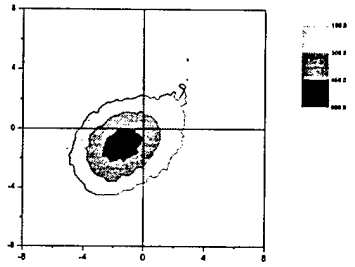	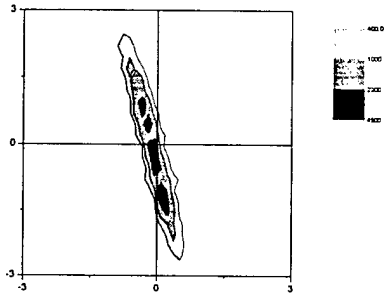	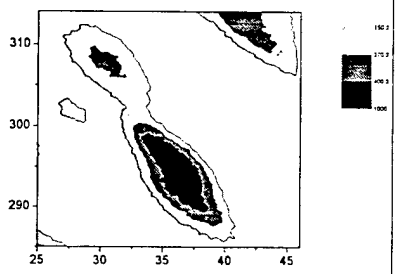
Aging 538°C, 15min		
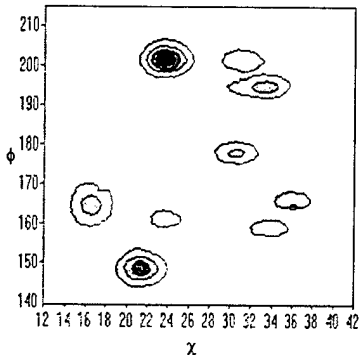	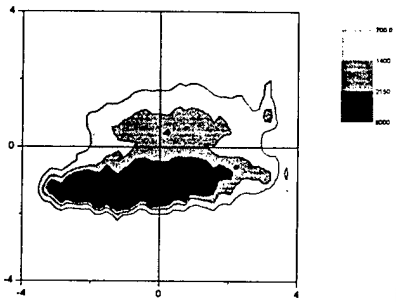	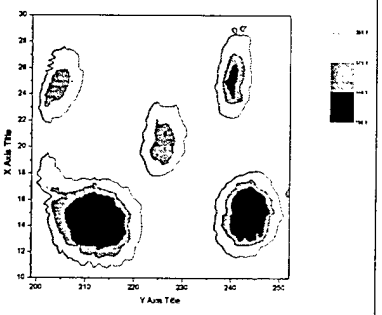
Aging 538°C, 30min		

TIMETAL- LCB	Ti-15-3	VT-22
	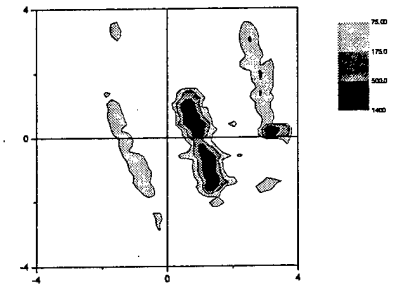	
Aging 538°C, 2h		
	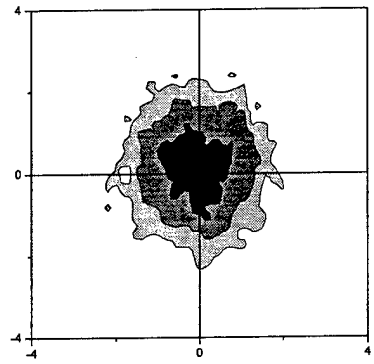	
Aging 538°C, 12h		

Figure 85. Comparison of evolution of {110}β intensity distributions $Iq_{\perp}$ for three beta alloys.

Processes of structural transformation in beta phase occurs much faster in TIMETAL-LCB and much slower in Ti-15-3. This well corresponds to the much faster aging response of TIMETAL-LCB as compared to other alloys.

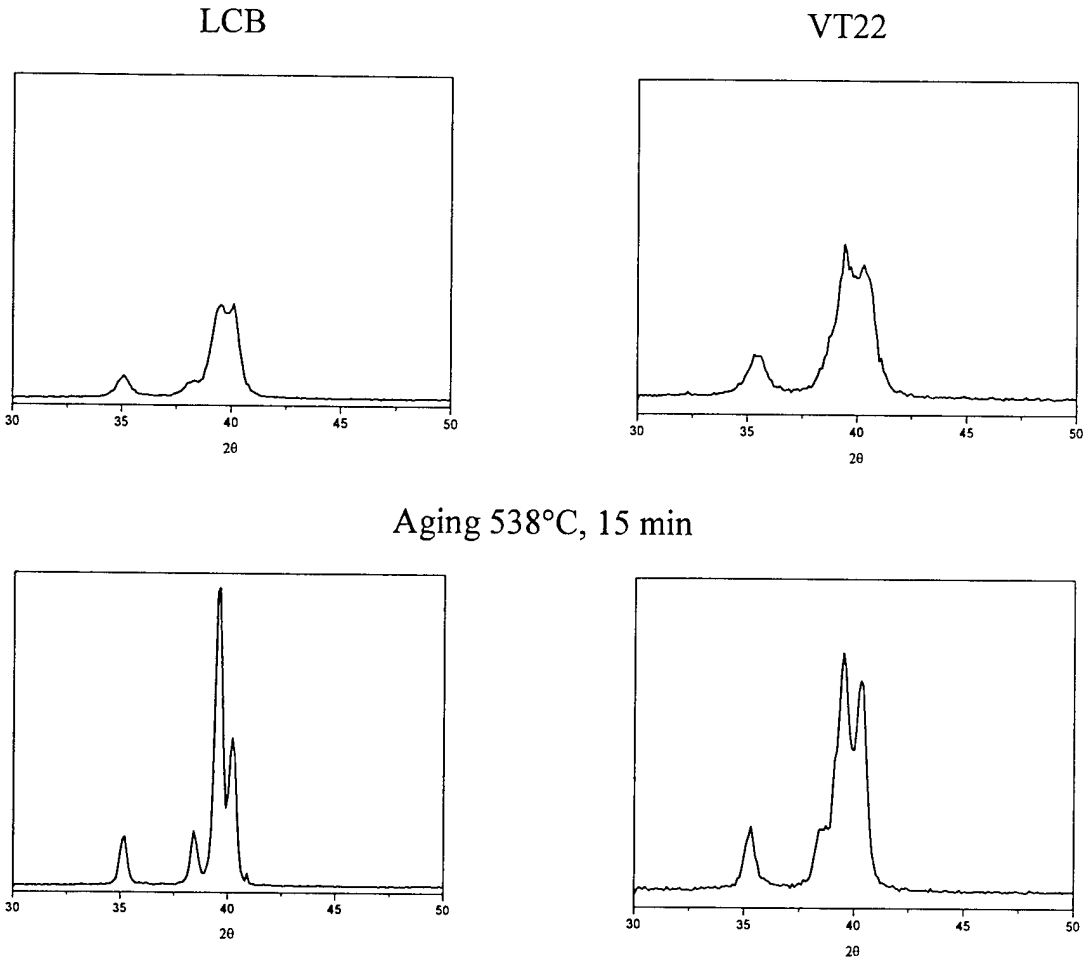

Figure 86. Comparison of X-ray patterns for TIMETAL-LCB and VT22 after aging at 538 °C, (a) 15` and (b) 2h.

Reflections of both alpha and beta phases became sharp faster in TIMETAL-LCB giving an evidence of faster relaxation of stresses arisen during precipitation.

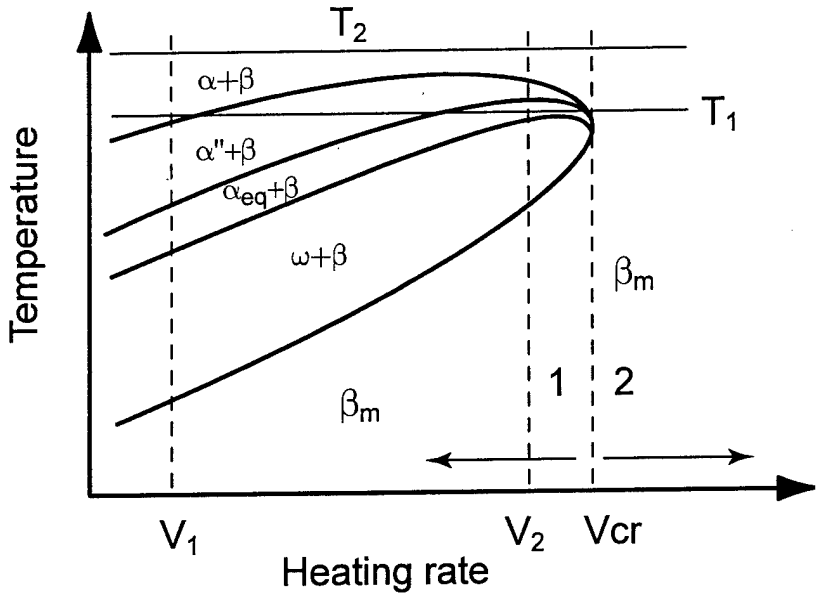

Figure 87. Scheme illustrating influence of heating rate on mechanism of precipitation in titanium β-alloys.

See explanation in ref. [14].

Prognoses of the Cr, Al and Ti losses

T=2100, 2050 and 2000 K. S=0,40x0,30=0,12 m^2,
DCr(T) = 8,41E-06*exp(-208000/R*(1/T-1/1923))*exp(36,6/R*(1/T^2-1/1923^2))

Table 1
The initial composition of the melt in the cold hearth

mass%			at/%		
Al	Cr	Ti	Al	Cr	Ti
6.3	2	91.7	10.68008	1.759148	87.56077
6.3	5	88.7	10.70425	4.407826	84.88792
6.3	6.5	87.2	10.71638	5.736667	83.54695
6.3	8	85.7	10.72854	7.068523	82.20294

Table 2
The partial excess Gibbs energies of Al and Cr at 2100, 2050 and 2000K

		gammaAl			gamma Cr		
Xal	Xcr	2100	2050	2000	2100	2050	2000
0.107	0.071	0.278936	0.258904	0.240311	1.09043	1.098936	1.107509
0.08	0.02	0.29073	0.268779	0.247555	1.096691	1.10345	1.110251

Table 3
Evaporation pressures above pure liquid components

Element	A	B	C	Po(2100)	Po(2050)	Po(2000)
Al	16379	9.979	-0.335	1550.188	1008.458	641.958
Cr	18204	9.446	-0.114	333.079	205.2635	123.4623
Ti	22946	10.581	-0.373	3.459371	1.889717	1.001307

Table 4
Diffusivity

Element	D(2100)	D(2050)	D(2000)
Al	3.70E-08	3.00E-08	2.41E-08
Cr	2.569E-07	2.018E-07	1.568E-07

Table 5
The melting time of 16.2 kg charge under different melting rate

*d*m/*d*t	40 kg/h	50 kg/h	60 kg/h
t (s)	1.44E+03	1.15E+03	9.60E+02

Table 6
The evaluation of Cr losses at 2100 K

t(s)	Ccr mol%	dM (kg)	Ccr mol%	dM (kg)	Ccr mol%	dM (kg)	Ccr mol%	dM (kg)
0	4.410		**5.74**		**7.07**		**1.76**	
1	3.956		5.150		6.3429		1.5790	
2	3.790		4.933		6.0761		1.5126	
3	3.670		4.777		5.8835		1.4646	
4	3.573		4.651		5.7286		1.4261	
5	3.492		4.545		5.5977		1.3935	
960	0.801	**0.365**	1.042869	**0.475**	1.2845	**0.585**	0.319765	**0.146**

1150	0.743	**0.409**	0.966893	**0.533**	1.1909	**0.656**	0.296469	**0.164**
1440	0.677	**0.471**	0.880602	**0.614**	1.0846	**0.755**	0.27001	**0.189**

Table 7

The evaluation of Al losses a at 2100 K

t(s)	Cal mol%	Wal	dM
0	**10.7**	0.023037	
1	6.913359	0.014884	
2	5.951081	0.012813	
3	5.357195	0.011534	
4	4.931769	0.010618	
5	4.603612	0.009912	
960	0.041094	0.439701	**0.23675**
1150	0.037546	0.401739	**0.2574**
1440	0.033553	0.359014	**0.2859**

Table 8

The evaluation of Ti losses at 2100 K

t(s)	d M(kg)
960	**0.031**
1150	**0.037**
1440	**0.046**

Table 9

The evaluation of Cr losses at 2050 K

t(s)	Ccr mol%	d M (kg)	Ccr mol%	dM (kg)	Ccrmol%	dM (kg)	Ccrmol%	dM (kg)
0	**4.41**		**5.74**		**7.07**		**1.76**	
1	4.080		5.3106		6.5411		1.6283	
2	3.955		5.1476		6.3403		1.5784	
3	3.863		5.0279		6.1929		1.5416	
4	3.788		4.9304		6.0728		1.5118	
5	3.724		4.8470		5.9701		1.4862	
960	1.076	**0.291**	1.400007	**0.378**	1.724399	**0.466**	0.42927	**0.116**
1150	1.000	**0.328**	1.30221	**0.426**	1.603942	**0.526**	0.399284	**0.131**
1440	0.914	**0.380**	1.18926	**0.494**	1.46482	**0.607**	0.364651	**0.152**

Table 10

The evaluation of Al losses a at 2050 K

t(s)	Cal mol%	Wal	d M(kg)
0	10.7	0.014306	
1	7.8586	0.010507	
2	7.0245	0.009392	
3	6.4795	0.008663	
4	6.0731	0.00812	

Table 11

The evaluation of Ti losses at 2050 K

t(s)	d M(kg)
960	**0.0168**
1150	**0.0202**
1440	**0.0253**

5	5.7497	0.007687	
960	0.6491	0.000868	**0.18692**
1150	0.5931	0.000793	**0.20586**
1440	0.5300	0.000709	**0.23198**

Table 12

The evaluation of Cr losses at 2000 K

t(s)	Ccr mol%	dM (kg)	Ccrmol%	dM (kg)	Ccrmol%	dM (kg)	Ccrmol%	dM (kg)
0	**4.41**		**5.74**		**7.07**		**1.76**	
1	4.1754		5.4346		6.4389		1.6664	
2	4.0839		5.3155		6.2032		1.6298	
3	4.0158		5.2269		6.0315		1.6027	
4	3.9598		5.1540		5.8925		1.5803	
5	3.9114		5.0910		5.7742		1.5610	
960	1.373296	**0.219**	1.787465	**0.284**	1.5132	**0.351**	0.548073	**0.0874**
1150	1.274897	**0.248**	1.65939	**0.322**	1.3825	**0.398**	0.508802	**0.099**
1440	1.157442	**0.289**	1.506511	**0.357**	1.2365	**0.464**	0.461927	**0.115**

Table 13

The evaluation of Ti losses at 2000 K

t(s)	Cal mol%	Wal	dM (kg)
0	10.7	0.008485	
1	8.6679	0.006874	
2	8.0023	0.006346	
3	7.5464	0.005984	
4	7.1945	0.005705	
5	6.9064	0.005477	
960	0.9805	0.000778	**0.1618**
1150	0.8959	0.00071	**0.17877**
1440	0.8006	0.000635	**0.20218**

Table 14

The evaluation of Ti losses at 2000 K

t(s)	d M(kg)
960	**0.00866**
1150	**0.01038**
1440	**0.01303**

Prognoses of the Cr, Al and Ti losses

T=2100, 2050 and 2000 K. S=0,40x0,30=0,12 m^2,
DCr(T)= 14,8*E-06*exp(-217000/R*(1/T-1/1923))*exp(43E+06/R*(1/T^2-1/1923^2))

Table 1
The initial composition of the melt in the cold hearth

mass%			at/%		
Al	Cr	Ti	Al	Cr	Ti
6.3	2	91.7	10.68008	1.759148	87.56077
6.3	5	88.7	10.70425	4.407826	84.88792
6.3	6.5	87.2	10.71638	5.736667	83.54695
6.3	8	85.7	10.72854	7.068523	82.20294

Table 2
The partial excess Gibbs energies of Al and Cr at 2100, 2050 and 2000K

		gammaAl			gamma Cr		
Xal	Xcr	2100	2050	2000	2100	2050	2000
0.107	0.071	0.278936	0.258904	0.240311	1.09043	1.098936	1.107509
0.08	0.02	0.29073	0.268779	0.247555	1.096691	1.10345	1.110251

Table 3
Evaporation pressures above pure liquid components

Element	A	B	C	Po(2100)	Po(2050)	Po(2000)
Al	16379	9.979	-0.335	1550.188	1008.458	641.958
Cr	18204	9.446	-0.114	333.079	205.2635	123.4623
Ti	22946	10.581	-0.373	3.459371	1.889717	1.001307

Table 4
Diffusivity

Element	D(2100)	D(2050)	D(2000)
Al	3.70E-08	3.00E-08	2.41E-08
Cr	3.210E-07	2.516E-07	1.947E-07

Table 5
The melting time of 16.2 kg charge under different melting rate

dm/dt	40 kg/h	50 kg/h	60 kg/h
t (s)	1.44E+03	1.15E+03	9.60E+02

Table 6
The evaluation of Cr losses at 2100 K

t(s)	Ccr mol%	dM (kg)	Ccr mol%	dM (kg)	Ccr mol%	dM (kg)	Ccr mol%	dM (kg)
0	**4.41**		**5.74**		**7.07**		**1.76**	
1	4.001		5.207		6.414		1.597	
2	3.849		5.009		6.170		1.536	
3	3.738		4.866		5.993		1.492	
4	3.649		4.749		5.850		1.456	
5	3.573		4.651		5.728		1.426	
960	0.866	**0.393**	1.127	**0.515**	1.388	**0.630**	0.345	**0.157**

1150	0.800	**0.441**	1.041	**0.577**	1.282	**0.706**	0.319	**0.176**
1440	0.724	**0.507**	0.943	**0.664**	1.161	**0.813**	0.289	**0.203**

Table 7

The evaluation of Al losses a at 2100 K

t(s)	Cal mol%	Wal	dM
0	**10.7**	0.023037	
1	6.913359	0.014884	
2	5.951081	0.012813	
3	5.357195	0.011534	
4	4.931769	0.010618	
5	4.603612	0.009912	
960	0.041094	0.439701	**0.23675**
1150	0.037546	0.401739	**0.2574**
1440	0.033553	0.359014	**0.2859**

Table 8

The evaluation of Ti losses at 2100 K

t(s)	d M(kg)
960	**0.031**
1150	**0.037**
1440	**0.046**

Table 9

The evaluation of Cr losses at 2050 K

t(s)	Ccr mol%	d M (kg)	Ccr mol%	dM (kg)	Ccrmol%	dM (kg)	Ccrmol%	dM (kg)
0	**4.41**		**5.74**		**7.07**		**1.76**	
1	4.112		5.353		6.593		1.547	
2	3.998		5.204		6.410		1.470	
3	3.914		5.095		6.275		1.415	
4	3.845		5.005		6.165		1.372	
5	3.786		4.928		6.070		1.335	
960	1.153	**0.309**	1.500	**0.403**	1.848	**0.496**	0.460	**0.123**
1150	1.069	**0.349**	1.392	**0.455**	1.715	**0.56**	0.427	**0.139**
1440	0.972	**0.405**	1.265	**0.528**	1.559	**0.65**	0.388	**0.161**

Table 10

The evaluation of Al losses a at 2050 K

t(s)	Cal mol%	Wal	d M(kg)
0	10.7	0.014306	
1	7.8586	0.010507	
2	7.0245	0.009392	
3	6.4795	0.008663	
4	6.0731	0.00812	

Table 11

The evaluation of Ti losses at 2050 K

t(s)	d M(kg)
960	**0.0168**
1150	**0.0202**
1440	**0.0253**

5	5.7497	0.007687	
960	0.6491	0.000868	**0.18692**
1150	0.5931	0.000793	**0.20586**
1440	0.5300	0.000709	**0.23198**

The evaluation of final cocentration of components during E-B melting

DCr(T) = 8,41*10^-6*exp(-208000/R*(1/T-1/1923)*exp(36,6*10^6/R*(1/T^2-1/1923^2)

88,7Ti-6,3Al-5Cr

mCr=0,8 kg mAl=1,008 kg

2100 K

dm/dt	mCr	mAl	dmCr	dmAl	dmTi	%Cr	%Al
60	0.8	1.008	0.365	0.23675	0.031	2.830695	5.01879
50	0.8	1.008	0.409	0.2574	0.037	2.556124	4.906973
40	0.8	1.008	0.471	0.2859	0.046	2.164887	4.751564

2050 K

dm/dt	mCr	mAl	dmCr	dmAl	dmTi	%Cr	%Al
60	0.8	1.008	0.291	0.187	0.0168	3.28277	5.294998
50	0.8	1.008	0.328	0.206	0.202	3.092243	5.254193
40	0.8	1.008	0.38	0.232	0.253	2.775025	5.127189

2000 K

dm/dt	mCr	mAl	dmCr	dmAl	dmTi	%Cr	%Al
60	0.8	1.008	0.219	0.1618	0.00866	3.721844	5.420697
50	0.8	1.008	0.248	0.17877	0.01038	3.546908	5.328266
40	0.8	1.008	0.289	0.20218	0.01303	3.29767	5.200251

88,7Ti-6,3Al-6,5Cr

mCr=1,04 kg mAl=1,008 kg

2100 K

dm/dt	mCr	mAl	dmCr	dmAl	dmTi	%Cr	%Al
60	1.04	1.008	0.475	0.23675	0.031	3.703158	5.054974
50	1.04	1.008	0.533	0.2574	0.037	3.34155	4.947076
40	1.04	1.008	0.614	0.2859	0.046	2.829794	4.7967

2050 K

dm/dt	mCr	mAl	dmCr	dmAl	dmTi	%Cr	%Al
60	1.04	1.008	0.378	0.18692	0.0168	4.293605	5.325367
50	1.04	1.008	0.426	0.20586	0.0202	4.000537	5.226369
40	1.04	1.008	0.494	0.23198	0.0253	3.580628	5.089083

2000 K

dm/dt	mCr	mAl	dmCr	dmAl	dmTi	%Cr	%Al
60	1.04	1.008	0.284	0.1618	0.00866	4.863131	5.443362
50	1.04	1.008	0.322	0.17877	0.01038	4.635593	5.353722
40	1.04	1.008	0.375	0.20218	0.01303	4.315438	5.229273

88,7Ti-6,3Al-8Cr

mCr = 1,28 kg mAl = 1,008 kg

2100 K

dm/dt	mCr	mAl	dmCr	dmAl	dmTi	%Cr	%Al
60	1.28	1.008	0.585	0.23675	0.031	4.588292	5.091683
50	1.28	1.008	0.656	0.2574	0.037	4.14629	4.987508
40	1.28	1.008	0.755	0.2859	0.046	3.520395	4.842052

2050 K

dm/dt	mCr	mAl	dmCr	dmAl	dmTi	%Cr	%Al
60	1.28	1.008	0.466	0.18692	0.0168	5.309753	5.355936
50	1.28	1.008	0.526	0.20586	0.0202	4.94493	5.260645
40	1.28	1.008	0.607	0.23198	0.0253	4.446435	5.127077

2000 K

dm/dt	mCr	mAl	dmCr	dmAl	dmTi	%Cr	%Al
60	1.28	1.008	0.351	0.1618	0.00866	6.001858	5.466924
50	1.28	1.008	0.398	0.17877	0.01038	5.722498	5.380121
40	1.28	1.008	0.464	0.20218	0.01303	5.326096	5.25965

88,7Ti-6,3Al-2Cr

mCr = 0,32 kg mAl = 1,008 kg

2100 K

dm/dt	mCr	mAl	dmCr	dmAl	dmTi	%Cr	%Al
60	0.32	1.008	0.146	0.23675	0.031	1.116369	4.948272
50	0.32	1.008	0.164	0.2574	0.037	1.003758	4.829619
40	0.32	1.008	0.189	0.2859	0.046	0.846302	4.665

2050 K

dm/dt	mCr	mAl	dmCr	dmAl	dmTi	%Cr	%Al
60	0.32	1.008	0.116	0.18692	0.0168	1.300997	5.236386
50	0.32	1.008	0.131	0.20586	0.0202	1.208213	5.127808
40	0.32	1.008	0.152	0.23198	0.0253	1.077564	4.977448

2000 K

dm/dt	mCr	mAl	dmCr	dmAl	dmTi	%Cr	%Al
60	0.32	1.008	0.0874	0.1618	0.00866	1.477563	5.375381
50	0.32	1.008	0.099	0.17877	0.01038	1.406582	5.277736
40	0.32	1.008	0.115	0.20218	0.01303	1.30825	5.142507

The evaluation of final cocentration of components during E-B melting

DCr(T) = 14,8*10^-6*exp(-217000/R*(1/T-1/1923)*exp(43*10^6/R*(1/T^2-1/1923^2)

88,7Ti-6,3Al-5Cr

mCr=0,8 kg mAl=1,008 kg

2100 K

dm/dt	mCr	mAl	dmCr	dmAl	dmTi	%Cr	%Al
60	0.8	1.008	0.393	0.23675	0.031	2.653324	5.027951
50	0.8	1.008	0.441	0.2574	0.037	2.351847	4.91726
40	0.8	1.008	0.507	0.2859	0.046	1.932577	4.762847

2050 K

dm/dt	mCr	mAl	dmCr	dmAl	dmTi	%Cr	%Al
60	0.8	1.008	0.309	0.187	0.0168	3.17036	5.301152
50	0.8	1.008	0.349	0.206	0.202	2.958735	5.261431
40	0.8	1.008	0.405	0.232	0.253	2.614163	5.135672

2000 K

dm/dt	mCr	mAl	dmCr	dmAl	dmTi	%Cr	%Al
60	0.8	1.008	0.23	0.1618	0.00866	3.653954	5.424519
50	0.8	1.008	0.261	0.17877	0.01038	3.466271	5.33272
40	0.8	1.008	0.304	0.20218	0.01303	3.203971	5.20529

88,7Ti-6,3Al-6,5Cr

mCr=1,04 kg mAl=1,008 kg

2100 K

dm/dt	mCr	mAl	dmCr	dmAl	dmTi	%Cr	%Al
60	1.04	1.008	0.515	0.23675	0.031	3.450	5.068
50	1.04	1.008	0.577	0.2574	0.037	3.060	4.961
40	1.04	1.008	0.664	0.2859	0.046	2.506	4.813

2050 K

dm/dt	mCr	mAl	dmCr	dmAl	dmTi	%Cr	%Al
60	1.04	1.008	0.403	0.18692	0.0168	4.138	5.334
50	1.04	1.008	0.455	0.20586	0.0202	3.819	5.236
40	1.04	1.008	0.528	0.23198	0.0253	3.365	5.100

2000 K

dm/dt	mCr	mAl	dmCr	dmAl	dmTi	%Cr	%Al

88,7Ti-6,3Al-8Cr

mCr = 1,28 kg mAl = 1,008 kg

2100 K

dm/dt	mCr	mAl	dmCr	dmAl	dmTi	%Cr	%Al
60	1.28	1.008	0.63	0.23675	0.031	4.304	5.107
50	1.28	1.008	0.706	0.2574	0.037	3.827	5.004
40	1.28	1.008	0.813	0.2859	0.046	3.144	4.861

2050 K

dm/dt	mCr	mAl	dmCr	dmAl	dmTi	%Cr	%Al
60	1.28	1.008	0.496	0.18692	0.0168	5.124	5.366
50	1.28	1.008	0.56	0.20586	0.0202	4.733	5.272
40	1.28	1.008	0.65	0.23198	0.0253	4.174	5.142

2000 K

dm/dt	mCr	mAl	dmCr	dmAl	dmTi	%Cr	%Al
60	1.28	1.008	0.369	0.1618	0.00866	5.892	5.473
50	1.28	1.008	0.419	0.17877	0.01038	5.594	5.387
40	1.28	1.008	0.488	0.20218	0.01303	5.178	5.268

88,7Ti-6,3Al-2Cr

mCr = 0,32 kg mAl = 1,008 kg

2100 K

dm/dt	mCr	mAl	dmCr	dmAl	dmTi	%Cr	%Al
60	0.32	1.008	0.157	0.23675	0.031	1.047	4.952
50	0.32	1.008	0.176	0.2574	0.037	0.927	4.833
40	0.32	1.008	0.203	0.2859	0.046	0.757	4.669

2050 K

dm/dt	mCr	mAl	dmCr	dmAl	dmTi	%Cr	%Al
60	0.32	1.008	0.123	0.18692	0.0168	1.257	5.239
50	0.32	1.008	0.139	0.20586	0.0202	1.158	5.130
40	0.32	1.008	0.161	0.23198	0.0253	1.020	4.980

2000 K

dm/dt	mCr	mAl	dmCr	dmAl	dmTi	%Cr	%Al
60	0.32	1.008	0.092	0.1618	0.00866	1.449	5.377
50	0.32	1.008	0.104	0.17877	0.01038	1.375	5.279
40	0.32	1.008	0.121	0.20218	0.01303	1.270	5.144